Università Politecnica delle Marche

Scuola di Dottorato di Ricerca in Scienze dell'Ingegneria

Corso di Dottorato in Ingegneria Industriale

Biomaterials for Tissue Engineering by Additive Manufacturing

Ph.D. Dissertation of:

Maria Laura Gatto

Supervisor:

Prof. Paolo Mengucci

Ph.D. Course coordinator:

Prof. Giovanni Di Nicola

XX edition - new series

Università Politecnica delle Marche

Dipartimento di Scienze e Ingegneria della Materia, dell'Ambiente ed Urbanistica (SIMAU)

Via Brecce Bianche — 60131 - Ancona, Italy

Abstract

This PhD thesis deals with biomaterial for tissue engineering applications produced by additive manufacturing technologies.

The research was carried out focusing on biomaterials based on metal, polymer, ceramic and composite, aiming at combining biomaterials with innovative additive manufacturing technologies, geometries and surface functionalization to create 3D scaffolds suitable for the specific needs of tissue engineering.

3D scaffolds in titanium alloys (Ti6Al4V and Ti48Al2Cr2Nb) with lattice geometry were produced by electron beam powder bed fusion (EB-PBF). Ti6Al4V lattice scaffolds were fabricated starting from industrial EB-PBF process based on cost and waste reduction (reused powder) in order to overcome issues connected to the high costs of preclinical studies. On the other hand, the biological response of Ti-48Al-2Cr-2Nb (γ-TiAl alloy) in terms of adhesion, short-term viability and proliferation of NIH-3T3 cells on lattice scaffold for the first time has been studied to overcome critical issues associated with the presence of potentially cytotoxic elements.
In addition, scaffolds in stainless steels (316L and duplex) with graded lattice geometry were manufactured by laser powder bed fusion (L-PBF). 316L lattice scaffolds were graded for programming mechanical and biological behavior for short-term clinical applications. The most promising graded lattice geometry was also produced in duplex steels to compare for the first time the *in vitro* behavior of duplex steel with 316L stainless steel additively manufactured lattice scaffold.

High-definition bone biomimetic scaffolds were geometrically optimized and produced by vat photopolymerization by using a biocompatible polymer developed for medical applications requiring limited time contact with the body. The research work was focused on the studying of the influence of 3D bone-like structure on biomechanical performances of scaffold.

Correlation between morphometry, microstructure, mechanical properties, sintering temperature and time at peak temperature were investigated in an innovative way, in order to find the best sintering conditions for the biphasic calcium phosphate (tricalcium phosphate/hydroxyapatite 30 wt.%) composites grafted in severe alveolar bone defects

The know-how on resorbable polycaprolactone/hydroxyapatite (PCL/HA, 70/30 wt.%) scaffolds produced by L-PBF technology was extended to geometrically complex lattice structures and micro porous struts.

Results from the above issues dealt with this research work make the approach based on biomaterial → additive manufacturing technology → geometry optimization → surface functionalization → advanced characterization *in vitro* very promising for patient-customized solutions in tissue engineering applications.

Acknowledgment

The research work discussed in this PhD thesis has been carried out at Dipartimento di Scienze e Ingegneria della Materia, dell'Ambiente ed Urbanistica (SIMAU) of Università Politecnica delle Marche. However, due to the multidisciplinary scientific nature of the topic, the project has been accomplished thanks to collaborations with several academic and company partners. I would like to express my gratitude to all the people who helped me build this project.

I would like to thank Prof. Luca Iuliano of Politecnico di Torino and his group, in particular Dr. Manuela Galati, for the production of scaffolds in titanium alloys and for the constant scientific support on additive manufacturing technologies. I would also thank Ivano Corsini, CEO of 3D4MEC, for his availability in the production of stainless-steel scaffolds, and to Riccardo Groppo, for his enthusiasm and dedication in the design and manufacturing of samples. I am extremely grateful to Vanna Menco, CEO of Prosilas, who believed in the project and made me available materials and machines for polymer scaffolds production in a very short time. I would like to express my gratitude to Prof. Livia Visai, Prof. Lorenzo Fassina and Dr. Nora Bloise of Univeristà di Pavia for biological tests and for their insightful comments. I also appreciate all the support I received from Dr. Francesco Leonardi and the whole team of PUNTOZERO for their commitment to a challenging but rewarding project of bone biomimetic scaffold. My gratitude extends to Prof. Elena Bassoli, Prof. Lucia Denti, Dr. Silvio Defanti and Dr. Emanuele Tognoli of Università di Modena e Reggio Emilia for the mechanical tests, which gave us some nice surprises. Additionally, I would like to express gratitude to Prof. Alessandra Giuliani of Università Politecnica delle Marche (Dept. Disclimo), who initiated me to the world of imaging and to Prof. Monica Mattioli Belmonte and Dr. Giorgia Cerqueni (Dept. Disclimo) for all the experiments and bio consultations. I would like to thank Prof. Paolo Gargiulo for hosting me at Reykjavik University. It was a great experience to start working with him, Donatella and Halldór, Prof. at Landspitali - University Hospital of Iceland, on Total Hip Arthroplasty project. Finally, I would like to thank Prof. Daniel Munteanu of Transilvania University, for his support and advices, as well as for his hospitality in Brasov on the occasion of BraMat.

1. Introduction

The American anthropologist Margaret Mead (1901-1978) defined a healed femur the earliest sign of civilization: the healed bone shows that someone must have cared for the injured person, hunting on his behalf, bringing him food and serving him at personal sacrifice[1]. Caring for others made it possible to preserve a feeling of humanity even during the most dramatic periods of 20th century history. The double-Nobel prized Marie Curie (1867-1934) invented a radiological car, called *petite Curies*, containing an X-ray machine and photographic darkroom equipment, which could be driven right up to the battlefield where army surgeons could use X-rays to guide their surgeries. Through her efforts, it is estimated that the total number of wounded soldiers receiving X-ray exams during the First World War exceeded one million[2].
This is the premise from which the PhD project starts and the thesis develops.

The thesis deals with the biomaterials for tissue engineering produced by additive manufacturing. Scaffolds were designed, produced, functionalized and characterized for meeting the needs of tissue regeneration. The aim of the thesis is responding to specific needs of tissue engineering, by the promising approach based on biomaterial → additive manufacturing technology → geometry optimization → surface functionalization → advanced characterization, which should be followed by the *in vivo* clinical trial phase.

Specifically, tissue engineering framework is described in Chapter 2, with a focus on biomaterials, additive manufacturing technologies and characterization techniques used in PhD research project, respectively in Chapter 3, 4 and 5. In chapter 6 of experimental results and discussion, solutions to the following problems, related to bone tissue engineering, were investigated:

- Industrial practice of reused powder was proposed in electron beam powder bed fusion (EB-PBF) process for overcoming issues connected to the high costs of preclinical studies (Ti6Al4V in Chapter 6);
- Ti-48Al-2Cr-2Nb (γ-TiAl alloy) was suggested to avoid the critical issues associated with the presence of potentially cytotoxic vanadium and its oxide in Ti6Al4V biomedical alloy (Ti6Al4V in Chapter 6);
- Grading of scaffold lattice geometry was designed for obtaining programmed mechanical and biological behavior for short-term clinical applications (316L in Chapter 6);
- Duplex stainless steel was considered as new alternative to bet the austenitic stainless steel crevice resistances in chloride media, by comparing for the first time the *in vitro* behavior of duplex and 316L scaffolds (Duplex in Chapter 6);
- 3D bone-like structure was examined to understand the influence of bone biomimicry on biomechanical performances of scaffold (DS3000 in Chapter 6);

[1] From *The Gift of Pain: Why We Hurt & what We Can Do about it*, by Philip Yancey and Paul W. Brand.
[2] From *Marie Curie and her X-ray vehicles' contribution to World War I battlefield medicine* on "The Conversation", by Timothy J. Jorgensen, director of the Health Physics and Radiation Protection Graduate Program and Associate Professor of Radiation Medicine, Georgetown University.

- The best sintering conditions for biphasic calcium phosphate was studied by innovatively correlating scaffold morphometry, microstructure, mechanical response, sintering temperature and time at peak temperature (BCP in Chapter 6);
- The know-how on resorbable polycaprolactone/hydroxyapatite (PCL/HA) scaffolds produced by laser powder bed fusion (L-PBF) was extended to geometrically complex lattice structures and micro porous struts, in order to accelerate the degradative process of PCL matrix (PCL/HA in Chapter 6).

Finally, in the General Conclusions (Chapter 7) are briefly summarized the results obtained in the PhD project, pointing out the academic and company collaborations and the scientific production.

2. Tissue Engineering

List of abbreviations

TE - Tissue engineering

GODT - Global Observatory on Donation and Transplantation

WL - Waiting list

AIDO - Italian association for the donation of organs

LD - Living donors

ECM - Extracellular matrix

BTE - Bone tissue engineering

GFs - Growth factors

MSCs - Mesenchymal stem cells

2.1. Background: Transplantation of human tissues and organs

Tissue engineering (TE) had its breakthrough in 1993, after its formalization by Lager and Vacanti [1] as "the interdisciplinary field that applies the principles of engineering and life sciences toward the development of biological substitutes that restore, maintain, or improve tissue function".

The initial motivation was to tackle the growing issue of the donor organ and tissue shortages, which resulted in increased deaths of patients on transplantation waiting lists [2]. Another incentive was to overcome the ethical and deontological problems related to the donors in *limine vitae*.

European union data on organ donation and transplantation activity in the year 2020, collected from the Global Observatory on Donation and Transplantation (GODT, http://www.transplant-observatory.org/), shows a dramatic mismatch between the total number of patients who were active on the waiting list (WL) (96,630) vs the number of transplanted organs in the same year (about 34,500) in Table 2.1. Organ transplantation refers to the transfer of human organs (kidney, liver, heart, lung, pancreas and small bowel) from a living or deceased donor to a recipient. Europe's population is reported in Table 2.1as a reference.

Table 2.1 - Europe waiting list of organ transplants in 2020. Data collected from GODT. WL – waiting list.

Population (million inhabitants)	513
Patients included on the WL for the first time in 2020	32,988
Total number of patients ever active on the WL during 2020	96,630
Patients awaiting organ transplantation (only active candidates) on 31/12/2020	58,175
Patients who died while on the WL during 2020	3,979

Data on donations, transplants and patients during the year 2020 in Italy (Date of publication: 2nd February 2021 from AIDO, the Italian association for the donation of organs, tissues and cells, https://aido.it/statistiche/) reveals a similar trend to Europe (Table 2.2). Moreover, 45,054 patients received follow-up care post organ transplant.

Table 2.2 – Donators and transplants of organ, tissue and hematopoietic stem cells during the year 2020 in Italy. Data collected from AIDO. LD – living donors.

Population (million inhabitants)	60	
	Donators	Transplants
Organ	1,531 (295 LD)	3,441
Tissue	9,564	13,790
Hematopoietic stem cells (registered in the IBMDR - Italian Bone Marrow Donor Registry)	288	875
Patients added to the WL during the year	4,144	

A more accurate analysis of AIDO on tissues transplantation activity between 2015-2020 (Figure 2.1) demonstrates that bone remains the most transplanted tissue. The significant decrease in tissue transplantation in 2020 is due to the consequences of the Coronavirus disease (COVID-19) pandemic.

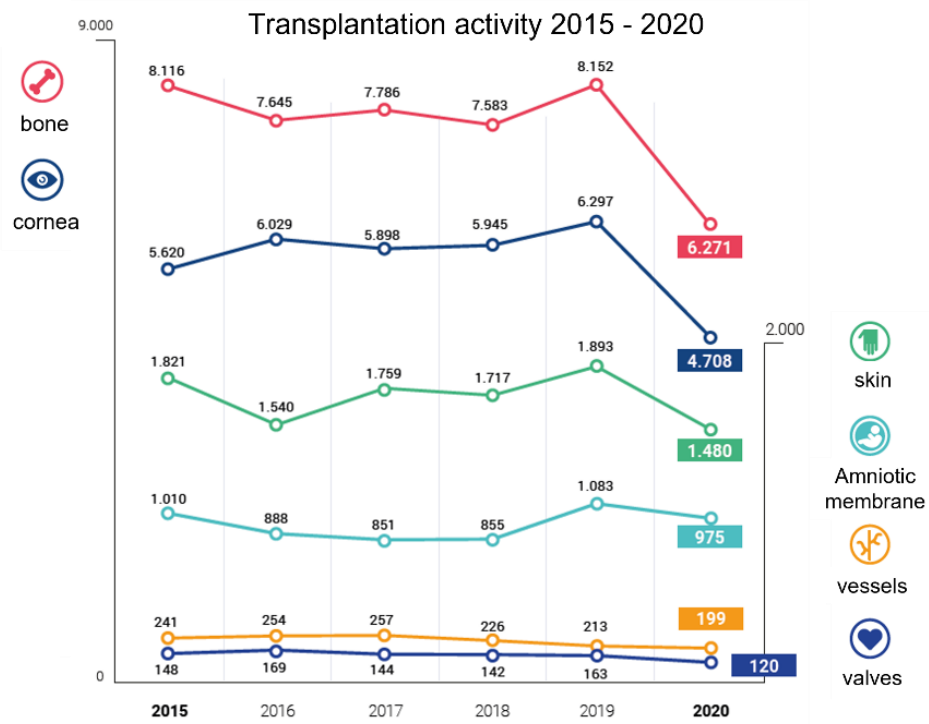

Figure 2.1 - Tissues transplantation activity in the temporal range 2015-2020 in Italy. (Adapted from AIDO Report 2020 – https://www.trapianti.salute.gov.it/imgs/C_17_cntPubblicazioni_438_allegato.pdf)

2.2. The alternative: Tissue Engineering

Therefore, organ and tissue transplantation are severely limited by the demand for transplants far exceeding donors' supply, the related ethical issues, the clinical costs of follow-up to monitor the transplanted organ status and the effects of anti-rejection drugs and therapies.

Tissue engineering is a proposed clinical alternative to transplantation in the case of loss or failure of an organ or tissue. Diseases or conditions that can benefit from TE technologies include skin burns, bone defects, nervous system repair, craniofacial reconstruction, cornea replacement, volumetric muscle loss, cartilage repair, vascular disease, pulmonary disease, gastrointestinal tissue repair, genitourinary tissue repair, congestive heart failure, chronic kidney disease, liver disease and cosmetic procedures [3].

TE adopts three general strategies for creating new tissue:

1) To replace only the specific cells which supply the needed function with isolated cells or cell substitutes, eventually reprogramming cells before infusion. This approach avoids the complications of surgery. Its potential limitations, in addition to being bound by strict ethical and safety procedures regarding cell manipulation, include failure of the infused cells to maintain their function in the recipient and immunological rejection;
2) The delivery of tissue-inducing substances (signal molecules, such as growth and proliferation factors) to the targeted locations. The success of this approach depends on the efficacy of the delivery method;
3) When tissues are so severely altered by cancer, congenital anomaly, or trauma that conventional surgical treatments are no longer applicable, TE strategy is used to customize a cell transplant device (scaffold) [1, 4].

This latter strategy is based on the TE "triad" of cells, signals, and scaffold. Cells are used for the creation of new tissue and its integration with existing host tissues. Different signals are provided as growth factors or specific mechanical or electric stimuli to regulate cell behaviors. Scaffold aims to create an implantable substrate capable of providing functional and structural 3D support, thereby providing the same role as the extracellular matrix (ECM) of in vivo tissues [2, 5, 6].
The scaffolding approach is based on the following observations [1]:

1) Every tissue undergoes remodeling;
2) Infused cells tend to recreate the tissue structure under appropriate experimental conditions;
3) To restore tissue structure and function, cells need support with an intrinsic organization as a template to manage the repair process.;
4) Tissue cannot be implanted in large volumes since cells do not survive if located more than a few hundred micrometers from the nearest capillary.

Thus, the device is designed to guide cell organization and growth and allow nutrients diffusion to the transplanted cells [1].

This research project is focused on tissue engineering applications based on the scaffold serving as a cell transplant device.

Tissues reconstruction can follow two different approaches, in Figure 2.2:

1) The Top-Down approach (Figure 2.2A) is based on (a) the isolation and the expansion of the suitable dominant cell types of the target tissue; (b) a one-stage process for seeding and culturing selected cells in a 3D scaffold that replicates the size and morphology of the target tissue; and (c) the implantation of the reconstructed tissue. Due to the lack of a vascular system, mass transfer within the cultured cells depends on the diffusion property of the scaffold. The main advantage of a top-down approach is the prospect of combining biomaterial, design and production technology to tailor the biomechanical performances of the scaffold. However, this approach has some limitations, such as positioning cells with precision and

achieving geometric accuracy and tissue-specific cell densities. An additional limitation is the difficulty of incorporating vasculature throughout the 3D space [2, 6]. The device can be pre-vascularized or becomes vascularized as the cell mass expands after implantation due to natural host tissue response to the implant or artificial induction by slow release of angiogenic factors [1].

1) The Bottom-Up approach (Figure 2.2B) mimics the natural tissue development process by (a) the isolation of multiple cell types and their separate expansion separately; (b) the independent preparation of multiple modular tissue building blocks by culturing different cell types on corresponding modular scaffolds. Different methodologies can produce scaffolds, including hydrogels which encapsulate cells, self-assembled cell aggregation, cell sheets, and 3D cell printing; (c) the gradual tissue reconstruction via layer-by-layer assembly of the modular tissue building blocks; and (d) the implantation of the designed functional tissues. Due to the reconstruction of vascular systems, mass transfer within the gradually expanded tissues is not a limiting factor. However, specific sterilizations and aseptic techniques of required during production to tackle the high contamination risks caused by the long spatial and temporal tissue reconstruction process. As multiple modular scaffolds are assembled layer-by-layer to provide the cultured cells with physical support, the reconstructed tissue's mechanical stability might be another issue to be considered [2, 6].

The Top-Down approach is used in the current research project with particular attention to scaffold design, material and production technology for bone tissue engineering therapy.

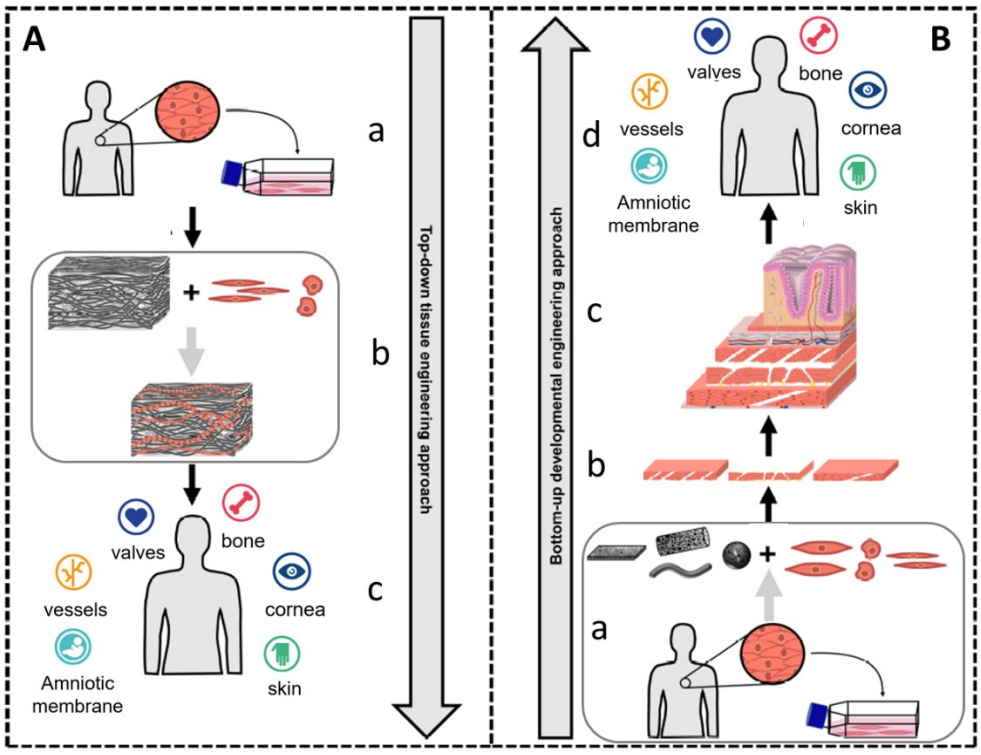

Figure 2.2 - Comparison of Top-Down (A) and Bottom-Up (B) approaches of tissue engineering. Adapted from [2].

2.3. Bone Tissue Engineering

To develop a scaffold-based bone tissue engineering (BTE) strategy, several issues are to be addressed. An in-depth understanding of bone and its characteristics, knowledge of the clinical problem, patient characteristics, and tissue defect specificity are the starting points for identifying the proper scaffold-based BTE therapy. This involves choosing the most accurate scaffold design (biomaterial and manufacturing method), cells and growth factors (GFs). Around this nucleus revolves a series of critical paths for developing BTE products: pre-clinical *in vitro* and *in vivo* investigations, clinical trial approval and conduction, scaffold commercialization and patient care (Figure 2.3) [5].

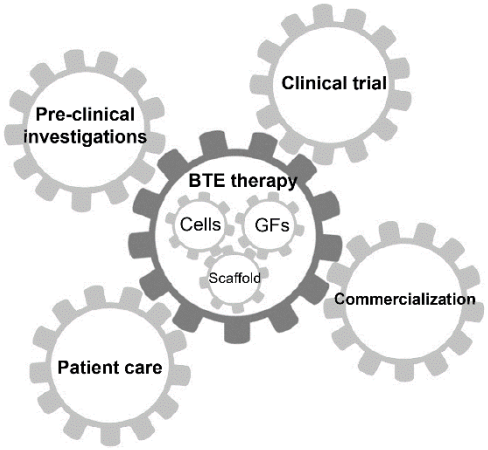

Figure 2.3 - Schematic representation of the challenges to be addressed in developing a scaffold-based Bone Tissue Engineering therapeutic strategy. Adapted from [5].

The PhD research activity deals with *in vitro* characterization investigation of BTE therapy. The work proposes various additive manufacturing biomaterial solutions for bone tissue regeneration.

2.3.1. Bone tissue

Bones exert mechanical, synthetic, and metabolic functions in the body. Mechanically bones protect internal organs, provides body support, and interact with muscles and tendons to generate body movement, such as locomotion. Its synthetic function is conducted by the bone marrow, where both bone and blood cells are synthesized in the process of hematopoiesis. Bones act as a reservoir of calcium, phosphorus, growth factors and fat involved in metabolic functions [7, 8, 9].

2.3.1.1. Bone structure and composition

Bone tissue is arranged in a multi-level hierarchical structure, as displayed in Figure 2.4.

Macroscopically, long bone consists of a dense, hard cylindrical shell of cortical bone (or compact bone) along the shaft of the bone that becomes thinner with a greater distance from the center of the shaft towards the articular surfaces. Cortical bone encompasses increasing amounts of porous trabecular bone (also called

cancellous or spongy bone) at the proximal and distal ends (Figure 2.4) to optimize articular load transfer. In humans, cortical bone corresponds to around 80% of the total skeleton bone and has a dense structure with a 3-12% porosity and an average density of 1.80 g/cm^3. Trabecular bone, which constitutes the remaining 20%, has a 50-90% porosity with an average trabecular spacing of around 1 mm and an average density of approximately 0.2 g/cm^3. The trabeculae have a large surface area for nutrient diffusion and growth factors circulation, thus allowing cancellous bone to play a metabolically active role and permitting a more persistent remodeling than cortical bone [8, 10, 11].

On a microscopic scale, cortical and trabecular bone are composed of parallel sheet structures called lamellae (sub-microstructure), formed by the alternate and regulated deposition of mineralized collagen fibers (nanostructure). In cortical bone, lamellae are organized in concentric layers around a central Haversian canal, which contains nerve and blood vessels, to form an Osteon (or a Haversian system). The osteon is a cylindrical structure running roughly parallel to the long axis of the bone. In trabecular bone, the lamellae are parallel and organized in an interconnected framework of rod and plate to form the trabeculae [10].

At the sub-nanostructural level (Figure 2.4), bone crystals, collagen molecules and non-collagenous organic proteins make up the extracellular matrix (ECM). The inorganic material of bone consists predominantly of phosphate and calcium ions that nucleate to form the hydroxyapatite ($Ca_{10}(PO_4)_6(OH)_2$) [9, 10].

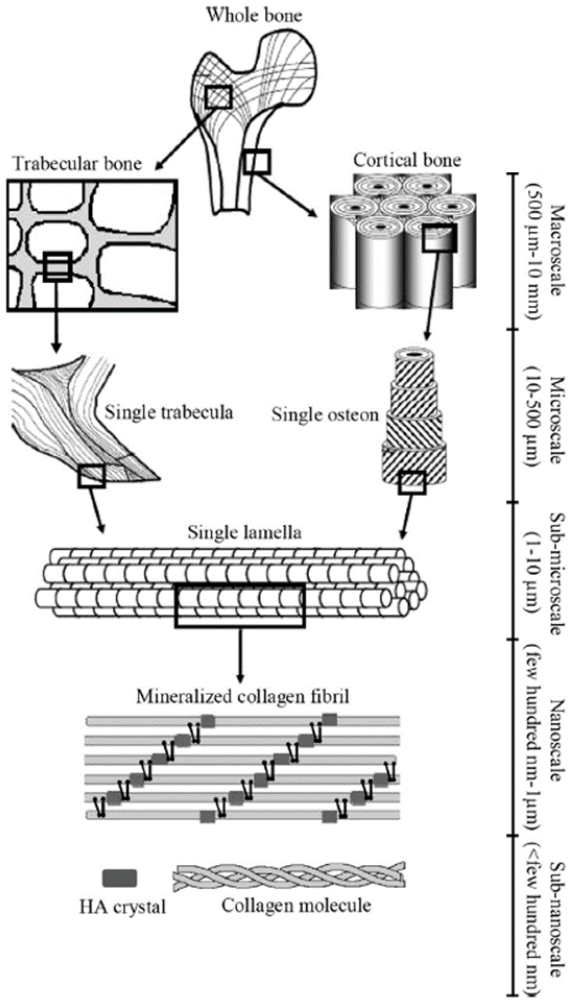

Figure 2.4 - Hierarchical organization of bone structure. Adapted from [12].

Several types of cells are hosted in the tissue:

1) Mesenchymal stem cells (MSCs) represent the adult osteoprogenitor stem cell population located in bone. MSCs are defined by two properties: clonogenic self-renewal and multi-potential lineage differentiation;
2) Osteoblasts are primarily known for their bone-forming function. They derive from osteoblast progenitor MSC differentiated into osteoblast progenitors that evolve into mature osteoblasts. This transition is related to bone matrix synthesis that occurs in two steps: the deposition of an organic matrix made by collagen and non-collagenic proteins, followed by its subsequent mineralization. At this stage, the mature osteoblasts can either undergo apoptosis or become osteocytes;
3) Osteocytes represent the last differentiation state of osteoblasts, which remain embedded in the bone matrix in lacunae. Osteocytes orchestrate the bone remodeling process via the direct regulation of both osteoblast and osteoclast activities;
4) Osteoclasts are responsible for bone resorption, which occurs through the dissolution of the inorganic phase of the bone matrix and the degradation of collagen proteins [8, 9].

2.3.1.2. Mechanical properties

The behavior of cortical bone is anisotropic, with strength and tensile-compressive moduli along the direction aligned with the diaphyseal axis (longitudinal direction) greater than the properties along the radial and circumferential directions. When loaded in tension along the longitudinal direction, cortical bone exhibits a bilinear stress/strain response in which a distinct yield point separates a linearly elastic region and a region of linear hardening that ends abruptly at a fracture strain of less than 3% (Figure 2.5A). In contrast, for compressive loading along the longitudinal direction, rapid hardening occurs after yielding, followed by softening, before failure at approximately 1.5% strain (Figure 2.5A) [13].

Trabecular bone can be viewed as a highly porous material. Porosity, architectural arrangement of the trabecular network, and the individual trabeculae's tissue-level properties determine the anisotropic mechanical properties of trabecular bone. As with cortical bone, the compression strength of trabecular bone is higher than tensile one. The stress/strain curve for trabecular bone does not exhibit a clear linear region or a well-defined yield point (Figure 2.5B). Nevertheless, this tissue is frequently treated as a linear elastic material, and once the modulus is calculated from a linear or polynomial curve fit to the initial portion of the curve, the yield point is defined by the 0.2% offset method. [13].

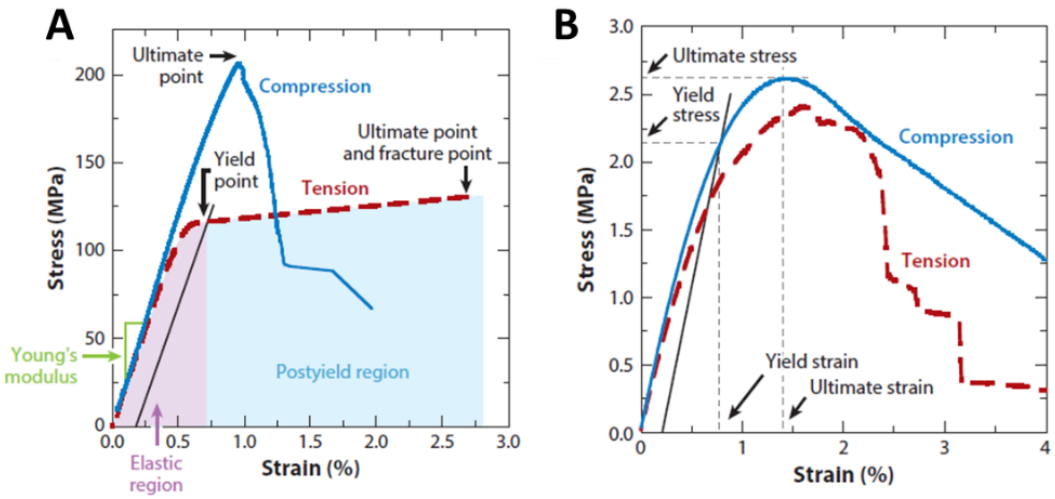

Figure 2.5 – Stress/strain curves from monotonic tests in tension and compression for (A) cortical bone and (B) trabecular bone. Adapted from [13].

2.3.1.3. Bone remodeling

Bone is a very dynamic tissue subjected to a continuous remodeling process, by which old microdamaged bone is replaced with new-formed bone. The remodeling cycle is made up of three principal phases:

1) the osteoclast-mediated bone resorption phase, during which both mineral and collagenous matrixes are dissolved;

2) the reversal period that matches the time and space of the resorption process to the formation of new tissue;
3) the new deposition of the bone matrix made by the osteoblasts.

Normal bone remodeling is necessary for fracture healing and skeleton adaptation to mechanical use and calcium homeostasis. The imbalance of bone resorption and formation results in several bone diseases. For example, excessive resorption by osteoclasts without the corresponding amount of neo-formed bone by osteoblasts contributes to bone loss and osteoporosis, whereas the contrary may result in osteopetrosis. Thus, the equilibrium between bone formation and resorption is necessary and depends on the action of several local and systemic factors, including hormones and biomechanical stimulation [8, 9].
The bone remodeling process renders bone a regenerating tissue. The role of the extracellular matrix in bone tissue is as follows:

1) ECM offers an environment for cells residing in that tissue to attach, grow, migrate and respond to signals;
2) ECM contributes to the mechanical properties of tissue, such as rigidity and elasticity, associated with the tissue functions;
3) ECM provides bioactive cues to the residing cells for regulation of their activities;
4) ECM acts as a reservoir of growth factors and potentiates their actions;
5) ECM constitutes a degradable structural support to allow neovascularization and remodeling in response to developmental, physiological and pathological challenges during dynamic tissue processes of morphogenesis, homeostasis and wound healing, respectively [14].

2.3.1.4. Bone healing and grafts

Bone tissue can fail when mechanical loads potentiate stresses over the limit a healthy bone can bear. Alternatively, when various pathologies decrease the mechanical properties of bone, the result is weakened bone which is prone to be damaged [7].
Following the hematoma formation in fractures caused by trauma, the MSCs are recruited, leading to the generation of a soft callus made of cartilaginous tissue. Subsequently, neo-angiogenesis and revascularization allow for the transformation of a cartilaginous matrix into an osseous tissue, and a hard bony callus replaces the primary soft callus. Since the hard callus is made of woven bone, its remodeling process, carried out by osteoclasts and osteoblasts, allows for substitution with the lamellar bone. Thus, the newly formed tissue is eventually indistinguishable from the adjacent uninjured bone [8].
There are cases in which the regenerative demand is beyond the normal ability for self-healing, such as in critical-size bone defects derived from orthopedic or oral-maxillofacial surgeries following traumas, infections and tumor resections. Important factors that affect the process of bone tissue healing are mechanical stability, proportions of the affected site, severity and incidence of adjacent tissue injuries [11].
In all of these cases, clinical intervention is needed to regenerate the bone tissue exogenously:

1) Autografts are obtained by taking bone from another part of the patient's body and may be harvested from several skeletal sites. Autografts are free from risks of disease transmission and autoimmune rejection. Moreover, they integrate into the host bone fast and are the most effective method for bone regeneration. Unfortunately, major vessel or visceral injuries during harvesting are among the limitations in using autografts;
2) For allografts, the bone graft is taken from a donor and can be obtained in greater quantities compared to the autograft. However, they are linked to risks of immune reactions and infection. These grafts tend to integrate more slowly and to a lesser degree than the autografts;
3) Xenografts derive from other species, commonly porcine and bovine sources. The xenografts are relatively inexpensive and do not lengthen the healing time, although they carry a rare risk of transmitting zoonotic diseases, causing an immune reaction [8, 11].

Engineered scaffolds overcome the limitations of autografts, allografts and xenografts. Novel approaches offered by tissue engineering is aimed to create synthetic grafts for repairing and regenerating damaged bone tissue. The use of a scaffold that meets the needs of bone tissue at the injury site, such as the multi-scale 3D structure, cells wellness, mechanical properties and allowed-regeneration and remodeling (in accordance with biomaterial degradability), is expected to stimulate healing and ensure full recovery of functionality [11].
After implanting a bone scaffold in the body, injured blood vessels quickly lead to protein adsorption on the scaffold surface, and the formation of the fibrin-rich clot with the role of a transitory surface matrix at the tissue-scaffold interface occurs. The immune system recognises the scaffold as a foreign body, inducing specific immune reactions. The scaffold actively regulates the type and extent of immune system reaction during bone regeneration. Initial inflammatory action is necessary to start the bone healing process. Still, persistent inflammatory action against the implant usually leads to the formation of connective tissue and a fibrotic capsule around the implant with the risk of implant failure [11].

2.3.2. Scaffold

“The art of scaffolding is determining where to put the holes and the biofactors”, according to S.J. Hollister [15]. Thus, an open and interconnected porous network constituted by well-distributed pores with appropriate size and shape must be designed appropriately for assuring scaffold balance between desired mechanical function and mass transport. Moreover, scaffold structure needs to be controlled not only on a macroscopic level (to fit into the defect site) but also microscopically (to improve features like osteoinduction, osteoconduction, osteogenesis, vascularization and mechanical stability) and even nanostructural configuration (to set up protein adsorption, cell adhesion, differentiation and proliferation) [5]. Biomaterial functions together with scaffold design to mimic at least partially the functions of native ECM, providing structural support and a healing response [14]. Furthermore, the control over scaffold properties must be necessarily exerted during the fabrication process. Another critical point of scaffold project is the choice of the

manufacturing method, which should be effective in lowering toxic residues at a minimum and be cost-effective to allow patient-customized device production on a large scale [5].

2.3.2.1. Biomechanical requirements

Scaffold mechanical properties, such as elastic modulus, tensile and compressive strength, fatigue and elongation percentage, are considered crucial in BTE and should be modulated to match those found at the implantation site, minimizing the risk of stress shielding, implant-related osteopenia and subsequent re-fracture [5].

From the biological point of view, the scaffold must avoid excessive immune response and should support the development of extracellular matrix and cell colonization, allowing the transit of oxygen and nutrient substances from the surrounding tissue as the waste disposal coming from the tissue being formed [7].

One of the main problems with the use of bone substitutes is the appearance of large defects and central osteonecrosis *in vivo*. Osteonecrosis is caused by the lack of blood supply that causes insufficient nutrient availability and hinders waste removal, leading to bone collapse and the need for further surgery. Moreover, a non-optimal vascularization causes delayed healing and fracture non-unions. Strategies to improve the formation of a vascular network in engineered bone scaffolds have often been cited as the most significant challenge in creating a device for clinical application [16].

In this context, scaffold architecture plays a pivotal role in tailoring the device's mechanical performances and biological response. A periodical arrangement of an elementary unit cell in the 3D space (lattice) allows the customization of pore morphology (size and shape) and arrangement (distribution and interconnectivity), together with total porosity, contributing to :

a. Nutrients and oxygen diffusion to cells and their metabolic waste removal, enhancing in vitro cell proliferation at short viability time;
b. Migration and differentiation of cells, favouring capillary ingrowth and long-term vascularization of *in vivo* regenerated bone.

However, blood capillaries formation and consequent tissue vascularization need an increasing open-porous structure, with the risk of mismatch with the required mechanical properties. Scaffold strength must be designed by maintaining an equilibrium between supporting the 3D structure itself and the physiological loads that surrounding tissue might transmit [17]. In addition, the bone substitute must have an elastic modulus close to that of host tissue to avoid the mechanical failure of the implant due to the stress shielding phenomenon causing the bone loss around the implant [18]. Moreover, lattice filler results are quite dissimilar to bone morphology.

The graded lattice structure is a potential solution to meet both the mechanical and long-term biological demands for bone regeneration, providing an adaptative porous gradient and better miming natural bone. Functional grading (variation of size, typology, material or strut diameter) helps program the scaffold's

deformation behaviour by controlling the local relative density of unit cells. Thus, graded filler enables the design of body implants with local stiffness matching that of the target bone [19].
Therefore, scaffold design must be balanced to guarantee scaffold biomechanical performances suitable for efficient implant osseointegration [7].

The size of pores recommended for a scaffold depends on the type of bone tissue for which it is being designed. Generally, smaller pore sizes (<75 μm) are suitable for the formation of fibrous tissues. In comparison, intermediate (75–100 μm) and larger pore sizes (>200 μm) are more suitable for the formation of unmineralized and fully mineralized bone tissues, respectively. The requirement for vascularization is pores larger than 300 μm. Generally, a range of pore sizes from 50 to 1000 μm is recommended for cell growth and full recovery [20].
Small and intermediate pores (40-100 μm) constitute the scaffold micro-porosity which increases the specific surface of the material, thus improving permeability and enhancing scaffold degradation (in case of degradable biomaterial). Particularly, micro-porosity within the scaffold struts is a factor that accelerates the material degradative process, allowing the infiltration of fluids into the construct and, subsequently, the scaffold matrix. Furthermore, micro-pores increase the number of sites available for protein absorption, improving cell adhesion, proliferation, differentiation and mineralization. [21].
Regarding the shape of pores, osseous tissues typically have curved surfaces; to therefore mimic this biomorphic pattern, pores are intended to have curved cross-sections [20].
Pore connectivity is another important geometrical parameter. Pore interconnections are channels that connect neighboring pores and primarily serve as transportation routes. Channel sizes in the range of 15-50 μm are generally suggested for good inter-pore flow properties. When the scaffold degrades at the end of its life, the efficiency of its removal process depends on the sizes of these interconnection channels and the biodegradability of the scaffold material itself [20].

2.3.2.2. Surface functionalization

The scaffold surface is the most critical factor for host immune response upon implantation, representing the first space where pivotal interactions between the biomaterial and host tissue occur [5, 22]. The success of the implant depends fundamentally on the interaction between biological fluids and the scaffold surface. The initial events include the adsorption of molecules from the surrounding fluid, creating a specific interface to which the cells respond. Scaffold macro and microtopography and chemical properties of the surface determine which molecules are adsorbed and how cells will adhere. The focal attachments made by the cells with their substrate then determines cell shape, which in turn transduces signals via the cytoskeleton to the nucleus, resulting in the expression of specific proteins which contribute towards the cell phenotype [10].

Scaffolds can be functionalized to improve their properties, such as reducing corrosion and increasing bioactivity. The most common functionalization treatment is coating the scaffold surface with a layer of biocompatible material or a combination of biocompatible compounds. Surface coating plays a dual role [23]:

1) Reduces the corrosion rate, avoiding the release of toxic ions;
2) Reduces the inflammatory response at the implant-host tissue interface, improving implant osteointegration.

The design of a scaffold surface with regard to its roughness and patterning can be tailored to aid in cell adhesion, proliferation, and differentiation. For osteoblasts and bone tissue engineering in general, the roughness of a scaffold surface is known to promote attachment and differentiation by supporting focal adhesion formation and extracellular matrix (ECM) accumulation. Investigations also show that microscale and nanoscale surface features promote mesenchymal stem cells' osteogenic differentiation compared to a smooth surface. Specific topographic patterns (grooves, pits, and pillars) on the surface of a scaffold have also been shown to direct cell behavior toward tissue regeneration.

The most basic surface chemistry that influences how the biomaterial behaves is surface wettability. The hydrophilicity of the scaffold surface interacts with serum proteins by either promoting or inhibiting their adsorption and denaturation [22].

References

1. Langer, R., & Vacanti, J. P. (1993). Tissue engineering. Science, 260(5110), 920-926.
2. Schmidt, T., Xiang, Y., Bao, X., & Sun, T. (2021). A Paradigm Shift in Tissue Engineering: From a Top–Down to a Bottom–Up Strategy. Processes, 9(6), 935.
3. Chandra, P. K., Soker, S., & Atala, A. (2020). Tissue engineering: Current status and future perspectives. In Principles of Tissue Engineering (pp. 1-35). Academic Press.
4. Ma, P. X. (2004). Scaffolds for tissue fabrication. Materials today, 7(5), 30-40.
5. Roseti, L., Parisi, V., Petretta, M., Cavallo, C., Desando, G., Bartolotti, I., & Grigolo, B. (2017). Scaffolds for bone tissue engineering: state of the art and new perspectives. Materials Science and Engineering: C, 78, 1246-1262.
6. Abdulghani, S., & Mitchell, G. R. (2019). Biomaterials for in situ tissue regeneration: A review. Biomolecules, 9(11), 750.
7. Velasco, M. A., Narváez-Tovar, C. A., & Garzón-Alvarado, D. A. (2015). Design, materials, and mechanobiology of biodegradable scaffolds for bone tissue engineering. BioMed research international, 2015.
8. Battafarano, G., Rossi, M., De Martino, V., Marampon, F., Borro, L., Secinaro, A., & Del Fattore, A. (2021). Strategies for bone regeneration: From graft to tissue engineering. International Journal of Molecular Sciences, 22(3), 1128.
9. Florencio-Silva, R., Sasso, G. R. D. S., Sasso-Cerri, E., Simões, M. J., & Cerri, P. S. (2015). Biology of bone tissue: structure, function, and factors that influence bone cells. BioMed research international, 2015.
10. Henkel, J., Woodruff, M. A., Epari, D. R., Steck, R., Glatt, V., Dickinson, I. C., Choong, P. F. M., Schuetz, M. A., & Hutmacher, D. W. (2013). Bone regeneration based on tissue engineering conceptions—a 21st century perspective. Bone research, 1(1), 216-248.
11. Codrea, C. I., Croitoru, A. M., Baciu, C. C., Melinescu, A., Ficai, D., Fruth, V., & Ficai, A. (2021). Advances in Osteoporotic Bone Tissue Engineering. Journal of Clinical Medicine, 10(2), 253.
12. Hamed, E., & Jasiuk, I. (2013). Multiscale damage and strength of lamellar bone modeled by cohesive finite elements. journal of the mechanical behavior of biomedical materials, 28, 94-110.
13. Morgan, E. F., Unnikrisnan, G. U., & Hussein, A. I. (2018). Bone mechanical properties in healthy and diseased states. Annual review of biomedical engineering, 20, 119-143.
14. Chan, B. P., & Leong, K. W. (2008). Scaffolding in tissue engineering: general approaches and tissue-specific considerations. European spine journal, 17(4), 467-479.
15. Hollister, S. J. (2005). Porous scaffold design for tissue engineering. Nature materials, 4(7), 518-524.
16. Tripathy, S. K., Goyal, T., & Sen, R. K. (2015). Management of femoral head osteonecrosis: Current concepts. Indian journal of orthopaedics, 49(1), 28–45.
17. Onal, E.; Frith, J. E.; Jurg, M.; Wu, X.; Molotnikov, A. Mechanical Properties and In Vitro Behavior of Additively Manufactured and Functionally Graded Ti6Al4V Porous Scaffolds. 2018, 21.

18. Chartrain, N. A., Williams, C. B., & Whittington, A. R. (2018). A review on fabricating tissue scaffolds using vat photopolymerization. Acta biomaterialia, 74, 90-111.
19. Al-Ketan, O.; Lee, D.-W.; Rowshan, R.; Abu Al-Rub, R. K. Functionally Graded and Multi-Morphology Sheet TPMS Lattices: Design, Manufacturing, and Mechanical Properties. J. Mech. Behav. Biomed. Mater. 2020, 102, 103520.
20. Wubneh, A., Tsekoura, E. K., Ayranci, C., & Uludağ, H. (2018). Current state of fabrication technologies and materials for bone tissue engineering. Acta Biomaterialia, 80, 1-30.
21. Zhang, K., Fan, Y., Dunne, N., & Li, X. (2018). Effect of microporosity on scaffolds for bone tissue engineering. Regenerative biomaterials, 5(2), 115-124.
22. Kim, B. S., Baez, C. E., & Atala, A. (2000). Biomaterials for tissue engineering. *World journal of urology*, *18*(1), 2-9.
23. Mohd Yusoff, M.F.; Abdul Kadir, M.R.; Iqbal, N.; Hassan, M.A.; Hussain, R. Dipcoating of Poly ("-Caprolactone)/Hydroxyapatite Composite Coating on Ti6Al4V for Enhanced Corrosion Protection. Surf. Coat. Technol. 2014, 245, 102–107.

3. Biomaterials

List of abbreviations

PHA - Polyhydroxyalkanoates

ECM - Extracellular matrix

FDA - Food and Drug Administration

PLA - Polylactic acid

PGA - Polyglycolic acid

PLGA - Polylactic co-glycolic acid

PCL - Polycaprolactone

MSCs - Mesenchymal stem cells

PEG - Polyethylene glycol

PBT - Polybutylene terephthalate

PET - Polyethylene terephthalate

PPF - Polypropylene fumarate

PPA - Polyacrylic acid

VPP - Vat photopolymerization

CaPs - Calcium Phosphates

HA - Hydroxyapatite

TCP - Tricalcium phosphate

BCP - Biphasic calcium phosphate

A biomaterial is a material that must be endowed with biocompatibility, having to coexist with biological systems. The biocompatibility definition, which achieved consensus in the 2018 conference[3], confirmed the definition agreed in 1985[4], as "the ability of a material to perform with an appropriate host response in a specific application". Therefore, biocompatibility is the ability of a material to induce an appropriate host response in a specific application and to interact with living systems without the risk of injury, toxicity, or rejection by the immune system and undesirable or inappropriate local or systemic effects.

Although the definition of biocompatibility focuses on the material-derived processes, it is worth noting that there are several mediators of the biocompatibility of a material, such as the nature and quality of the clinical intervention that places the material in contact with the host tissues. The characteristics of the patients in whom the device is implanted are also important. It is to be anticipated that considerable variability will be seen among patients. Age, sex, general health and concurrent disease, physical mobility, lifestyle features and pharmacological status contribute to this variation. The design of the device and the physical relationship between the device and the body also play significant roles [1].

Consequently, the definition of biomaterial that achieved a consensus in the 2018 conference is as follows: "A material designed to take a form that can direct, through interactions with living systems, the course of any therapeutic or diagnostic procedure" [2, 3].

Biomaterials can be classified in terms of their response with host tissues [4]:

- Inert materials cause minimal or null tissue response;
- Active biomaterial elicits a specific biological response at the interface, resulting in the formation of a bond with the surrounding tissues;
- Resorbable biomaterial gradually degrades over time. Degradation products should be nontoxic and be metabolized and eliminated from the body [5, 6]. The degradation behavior of scaffold material is a crucial feature, and the rate should be closely correlated with the rate of remodeling of the target tissue. Excessively rapid degradation may lead to internal structure collapse, hindering mass transfer and potentially resulting in necrosis at the defect site. Prolonged scaffold absorption can increase the risk of chronic inflammatory and foreign body responses and impede the integration of newly formed tissue [6].

Generally, metals are inert; polymers may be inert or resorbable; and ceramics may be inert, resorbable or active [4].

[3] In March 1986, a consensus conference was held in Chester (UK) under the auspices of the European Society of Biomaterials, focusing on "Amplification of the definitions presented in biomaterials". The proceedings were published in 1987 by Elsevier.

[4] A new consensus conference was convened in 2018 in Chengdu (China), organized under the auspices of the International Union of Societies of Biomaterials Science and Engineering (IUSBSE). The Proceedings of this conference are to be published by Elsevier.

3.5. Metals

Metals are preferred for the production of load-bearing devices such as hip joints and femur plates due to their high modulus of elasticity and yield strength. Metals currently used in manufacturing implants mostly contain iron (Fe), chromium (Cr), cobalt (Co), nickel (Ni), titanium (Ti), tantalum (Ta), molybdenum (Mo), vanadium (V), and tungsten (W). By combining several metallic elements, alloys with improved properties can be prepared beyond those of a single element. The alloys used in orthopedic surgery need to have specific properties:

- All alloys have a modulus of elasticity significantly higher than bone. This mechanical incompatibility causes a gradual atrophy of the bones due to the phenomenon of stress shielding [7, 8]. Thus, alloys mechanical properties should be tailored closer to the bone by the customization of the design;
- Since the implant is immersed in body fluid, a low rate of corrosion and relative inertness is essential to avoid inflammatory and allergic reactions from the body. The principal paradigm of biocompatibility of metallic biomaterials has been "the more corrosion resistant, the more biocompatible." Corrosion of metallic implants, due to chloride, dissolved oxygen and pH levels of body fluids, can affect surrounding tissues in three ways:

  (i) Electrical current may affect the behaviour of cells;
  (ii) The corrosion process may change the chemical environment;
  (iii) Metal ions may affect cellular metabolism.

  Therefore, most metals and alloys used today in implants and other medical devices are characterized by high corrosion resistance. Corrosion could be attained either due to low thermodynamic driving force for corrosion, as in the case of noble metals (e.g., aurum (Au), silver (Ag) and platinum (Pt)). Alternatively, corrosion may be due to a passive metal-oxide thin film that spontaneously forms on the surface and acts as a kinetic barrier such as stainless steels, Co-Cr, Ti, zirconium (Zr), niobium (Nb) and Ta alloys. However, since the latter has a high driving force to corrode when the oxide film on the surface is ruptured or interrupted, oxidation of the underlying metal occurs, leading to possible ion release into the environment. This process will happen until the oxide film regenerates, taking perhaps milliseconds. The time required for repassivation, also known as regeneration, differs for different biomaterials (Figure 3.1). The stability of surface oxide layers in 316L stainless steel is lower than Ti–6Al–4V and Co–Cr alloys. Therefore, surface modification (e.g., coating) may improve corrosion resistance [9].

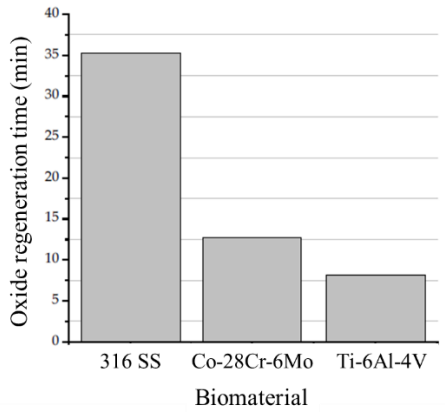

Figure 3.1 - Regeneration time of surface oxide films on metals for bone tissue engineering applications. Adapted from [9].

3.5.1. Titanium alloys

Titanium and titanium alloys have great corrosion resistance, making them inert biomaterials. Pure titanium is called "commercially pure titanium" (cp-Ti). Pure titanium is generally used in implants where high strength is unnecessary, such as in layers of metal fibers bonded to the implant's surface to allow bone ingrowth or enable cement to better bond with the implant for stronger fixation. The most used titanium alloy in implants is Ti-6Al-4V. Titanium has two crystallographic forms. The α-Ti phase has a hexagonal close-packed (hcp) crystallographic structure, stable below 883 °C. At this temperature, α-Ti transforms in β-Ti, which has a body-centred cubic (bcc) crystallographic structure. Titanium alloys with microstructure formed of a mixture of α-Ti and β-Ti are commonly named "α-β alloys" [7]. Although Ti–6Al–4V is the most common titanium alloy used in bone repair and replacement, its use as a biomaterial has some constraints. Possible release of vanadium (V) ions, a toxic element, and low wear resistance of the Ti–6Al–4V alloy are serious concerns associated with its use. This has led to the search for alternative V-free Ti alloys. Among the V-free Ti alloys investigated are new generations of γ-based TiAl intermetallic alloys, originally developed for aerospace and automotive applications. γ -TiAl alloys possess low density (3.8 g/cm^3), high stiffness and mechanical strength (up to 1,000 MPa), and good oxidation and corrosion properties. Recently, the biocompatibility of Ti–48Al–2Cr–2Nb (at.%), a second-generation γ -titanium aluminide, has been demonstrated *in vitro* and *in vivo* [10].

3.5.2. Stainless Steels

Stainless steel is most often used in implants intended to repair fractures, such as orthopedic implants and joint replacement. Many surgical and dental instruments, bone plates, bone screws, pins, rods, and coronary stents are made up of stainless steel. Stainless steel is mostly iron and contains other metals such as chromium (at least 10.5%, wt.%), cobalt, molybdenum, and carbon (less than 1.2 wt.%) which is added to improve corrosion

resistance. Many types of stainless steel with different chemical compositions are available. The 316 type is an austenitic chromium-nickel-molybdenum-containing stainless steel with acceptable biocompatibility [7]. A limitation in using stainless steel is its tendency to corrode under physiological conditions, leading to the release of metallic ions, mainly nickel, to nearby tissues. Nickel ions are considered the main cause of allergic contact dermatitis. Duplex stainless steels provide excellent mechanical properties and stress corrosion resistance compared with austenitic stainless steels. Due to the balance between chromium and nickel composition, these materials have a partly austenite and a partly ferrite structure [11]. Knowledge of the magnetic properties of biomaterial is also crucial because exposure to external static and/or variable magnetic fields could induce heat or movement that can injure the human body [12].

3.6. Polymers

Polymers can be natural or synthetic materials. Natural polymers, derived from polysaccharides, proteins and microorganisms, usually have excellent biodegradable and biocompatible properties:

- Polysaccharide-based natural polymers that have been widely used for in situ tissue regeneration include alginate, hyaluronic acid and chitosan;
- Proteins such as collagen, fibrin, gelatin and silk form the other class of natural-based polymers;
- Microorganisms naturally produce various biopolymers. For instance, several bacteria under nutrient-deficient conditions and in the presence of an excess of carbon produce different polyhydroxyalkanoates (PHAs) through intracellular carbon storage mechanisms. Genetic manipulation of microorganisms allows the biotechnological production of biopolymers with tailored properties.

Natural polymers better mimic extracellular matrix (ECM), although they are difficult to process in the required shapes while maintaining unaltered biological function. In addition, batch-to-batch variations hinder their mass production for medical use [13, 14, 15].

Synthetic polymers represent an attractive solution because of their physicochemical and mechanical properties. Synthetic polymers are already approved by the US Food and Drug Administration (FDA) for clinical applications. PLA (polylactic acid) and PGA (polyglycolic acid) are non-inflammatory, biocompatible and biodegradable polymers that support cell adhesion. Copolymer PLGA (polylactic co-glycolic acid) and PCL (polycaprolactone show relatively slow degradation rate (Figure 3.2) and high compatibility with human MSCs.

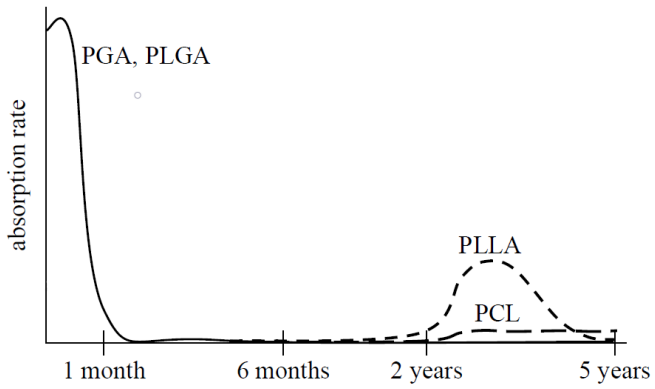

Figure 3.2 - Schematic for an absorption rate of absorbable polyesters. PGA, polyglycolide; PLGA, lactide–glycolide copolymer; PLLA, poly-L-lactide; PCL, poly-3-caprolactone. Adapted from [16].

PEG (polyethylene glycol) is another synthetic polymer that is very widely used. Among polymers showing high mechanical strengths are PBT (polybutylene terephthalate) and PET (polyethylene terephthalate), both highly biocompatible, biodegradable and impact resistant. However, due to the harmful effects of PET on the endocrine system, its use in biomedical applications needs further investigation. Since PPF (polypropylene fumarate) is biocompatible with good mechanical properties and a suitable decomposition rate, it has been used for biomedical engineering and orthopedic applications. Finally, PAA (polyacrylic acid) is worth mentioning for applications as permanent implants as they are not biodegradable [17].

A wide range of advanced photosensitive biocompatible polymers has been developed, and many are commercially available. They are typically composed of multi-functional monomers based on methacrylates or acrylic esters. However, their exact chemical compositions are often confidential and not provided by manufacturers. This means that physicochemical and mechanical properties, as well as cytotoxicity, remain unclear. Methacrylate- and acrylate-based monomers are primarily used since they demonstrate fast reaction rates, long-term stability and tunable mechanical properties. One major drawback of such monomers is the volume shrinkage that occurs during the chain growth free radical polymerization, which results in highly brittle printed parts [18]. Photosensitive biocompatible polymers have been widely used for dentistry applications [19].

3.6.1. Polycaprolactone

Polycaprolactone (PCL) is an aliphatic semi-crystalline polymer with a melting temperature ranging between 59 and 64 °C and a glass transition temperature of -60 °C. Hence, PCL attains a rubbery state at physiological temperature, resulting in high toughness and superior mechanical properties (high strength, elasticity depending on molecular weight). PCL is soluble in most organic solvents at room temperature, such as chloroform, dichloromethane, and tetrahydrofuran, whereas it does not dissolve in alcohol and water. It is

nontoxic, tissue compatible and slow-degrades under physiological conditions. Physiological degradation of polymers occurs primarily through the action of oxidative, enzymatic, and pH-related catalysis of hydrolysis. Small polymer fragments are completely metabolised by cells after an initial decrease in molecular weight, resulting in macroscopic structural breakdown. Being a chemically inert, biocompatible and low-cost bioabsorbable synthetic polymer, PCL has been widely applied in many TE applications. PCL alone has few limitations *in vivo*, such as its hydrophobicity, which hinders cell attachment and proliferation. To overcome this limitation, blending has proven successful. The ability to blend with other polymer or ceramics and therefore alter its properties according to the required application is one of the most beneficial aspects of the PCL polymer. This characteristic has made it a popular choice as a scaffold biomaterial. In particular, incorporating calcium phosphate-based ceramics, bioactive glasses and polymers into PCL has led to improved biomaterials with better mechanical properties, controllable degradation rates and enhanced bioactivity [22-24].

3.6.2. Acrylic acid ester

DS3000 is a photosensitive biocompatible polymer (acrylic acid ester) developed and commercialized by DWS Srl for highly precise surgical guides and medical applications that require a limited contact time with the body. According to the technical datasheet, DS3000 works directly from intraoral digital capture devices as a replacement of the traditional physical ones. The young modulus of 2.45 ± 0.13 GPa was experimentally calculated by Accardo et al. [25]. DS3000 was used in dentistry application to create surgical splints for surgical planning of jaw repositioning in bimaxillary orthognathic surgery [26]. Also, customized dental impressions were manufactured in DS3000 by vat photopolymerization (VPP) to facilitate the visualization of margins preparation for fillings [27]. Although the polymer is considered in Class I (no FDA approval needed), Han et al. [28] created an in vitro model of bone metastasis from breast cancer and reproduced the trabecular architecture of the bone tissue with DS3000. This device offered an adequate substrate to seed primary breast cancer bone metastatic cells [28].

3.7. Ceramics

Ceramics are inorganic materials composed of metallic and nonmetallic (oxides, hydrides, carbides, phosphates, sulfides, and silicates) elements bonded with ionic or covalent bonds. Ionic bonds are strong and directional, and therefore ceramics have melting temperatures higher than those of metals and polymers, which have metallic and covalent bonds, respectively. Ceramics are produced from materials in powder form by sintering. They are hard, strong and brittle. Since they do not have any free electrons, they are poor conductors of heat and electricity. Ceramics are now extensively used in dentistry, in the production of orthopedic implants for the spine and particularly in total hip implants due to their resistance against compression and wear. Ceramics are more expensive compared to other materials such as metals and polymers. Some inherent

advantages include no wear debris, high resistance to corrosion and the ability to be engineered to closely match the properties of the natural bone [7].
Ceramics are categorized into the following groups [13, 14]:

- Nearly inert (based on alumina and zirconia);
- Bioactive (based on bioactive glass);
- Resorbable ceramics (based on calcium phosphates).

3.3.2. Calcium phosphates

The most common calcium phosphates (CaPs) used in bone tissue engineering are hydroxyapatite (HA), tricalcium phosphate (TCP) and a combination of both, known as biphasic calcium phosphate (BCP). They have a composition similar to that of natural bone, good biocompatibility, osteoconductivity and can osteointegrate [17, 30].

Hydroxyapatite chemistry is similar to the natural apatite structure in the natural bone. The calcium to phosphate ratio (Ca/P) in hydroxyapatite is 1.67, which is the value of stoichiometric hydroxyapatite $Ca_{10}(PO_4)_6(OH)_2$, higher than many phosphate ceramics. In biological media, HA ceramics react with the ions present in the body fluid and form a surface apatite coat which induces protein adsorption and cell attachment and lead to bone formation and resorption of the biomaterial. The calcium phosphate ceramics' chemistry, composition, and crystallinity determine their solubility and resorption rate [7].

TCP is available in two forms: alpha-tricalcium phosphate (α-TCP, α-Ca3(PO4)2) and beta-tricalcium phosphate (β-TCP, β-Ca3(PO4)2). The different forms are based on temperature modification; α-TCP is produced at a temperature above 1125 °C, whereas β-TCP is produced at a temperature below 1125 °C. Unlike α-TCP, β-TCP is thermodynamically stable in a biological system and has a faster biodegradation rate because it is hydrolyzed. While HA has relatively high crystallinity and is difficult to degrade *in vivo*, TCP is more degradable than HA and rapidly becomes soluble. Additionally, β-TCP shows a higher resorption rate than HA. These findings eventually led to the development of biphasic calcium phosphate (BCP), a mixture of β-TCP and HA [31].

Biphasic calcium phosphate (BCP) consists of a mixture of HA and β-TCP, in varying ratios. Due to the preferential dissolution of the β-TCP component, the bioreactivity is inversely proportional to the HA/β-TCP ratio and can be controlled by manipulating the BCP composition. Thus, the advantage of BCP is the controlled dissolution [32].

3.8. Composites

A composite material is the combination of two materials, in which one of them serves as the reinforcing phase (in the form of fibers, sheets, or particles) embedded in the second material, the matrix. The properties of the final composite material depend on the chemical composition and physical form of each constituent and the interactions at the interfaces between these constituents. The minor component should be homogeneously distributed within the matrix and create a product with uniform properties throughout the structure. In the medical field, composites are formed by the combination of polymers and ceramics, polymers and metals, and metals and ceramics or a combination of several of these composites. For example, polymer-coated metals are used as heart valves, polymers combined with hydroxyapatite particles are used to produce bone tissue or bone engineering scaffolds, and polymeric nanoparticles and fibers are combined with magnetic particles to be used as drug delivery devices.

From the biological point of view, polymer-ceramic composites are highly similar to natural bone tissue composed of collagen (polymeric) fibrils and hydroxyapatite (ceramic) crystals. The combination of polymers and ceramics improves the mechanical property of the final construct and offers biological benefits. The goal is to enhance stiffness, strength, and biocompatibility, make the product more suitable for the host location, and achieve proper interactions with the surrounding tissue [7].

3.8.1. Polycaprolactone/Hydroxyapatite

Pure PCL shows a long degradation time, high hydrophobicity, poor bioactivity and low cell adhesion. To overcome these limitations and improve mechanical properties, PCL is usually combined with ceramic materials similar to the mineral constituents of natural bone, such as hydroxyapatite (HA). HA provides an osteo-friendly environment for MSCs and induces osteointegration with the host tissue. Kim et al. demonstrated that the increase of phosphate ion concentration during calcium phosphate scaffold degradation plays a key role in inducing the osteogenic differentiation of stem cells [31].

References

[1] Williams, D. F. (2008). On the mechanisms of biocompatibility. Biomaterials, 29(20), 2941-2953.

[2] Williams, D. F. (2019). The language of biomaterials-based technologies. Regenerative Engineering and Translational Medicine, 5(1), 53-60.

[3] Ghasemi-Mobarakeh, L., Kolahreez, D., Ramakrishna, S., & Williams, D. (2019). Key terminology in biomaterials and biocompatibility. Current Opinion in Biomedical Engineering, 10, 45-50.

[4] Hudecki, A., Kiryczyński, G., & Łos, M. J. (2019). Biomaterials, definition, overview. In Stem cells and biomaterials for regenerative medicine (pp. 85-98). Academic Press.

[5] Velasco, M. A., Narváez-Tovar, C. A., & Garzón-Alvarado, D. A. (2015). Design, materials, and mechanobiology of biodegradable scaffolds for bone tissue engineering. BioMed research international, 2015.

[6] Umuhoza, D., Yang, F., Long, D., Hao, Z., Dai, J., & Zhao, A. (2020). Strategies for tuning the biodegradation of silk fibroin-based materials for tissue engineering applications. ACS Biomaterials Science & Engineering, 6(3), 1290-1310.

[7] Hasirci, V., & Hasirci, N. (2018). Fundamentals of biomaterials. Verlag: Springer New York.

[8] Kanwar, S., & Vijayavenkataraman, S. (2021). Design of 3D printed scaffolds for bone tissue engineering: A review. Bioprinting, 24, e00167.

[9] Eliaz, N. (2019). Corrosion of metallic biomaterials: a review. Materials, 12(3), 407.

[10] Bello, S. A., de Jesús-Maldonado, I., Rosim-Fachini, E., Sundaram, P. A., & Diffoot-Carlo, N. (2010). In vitro evaluation of human osteoblast adhesion to a thermally oxidized γ-TiAl intermetallic alloy of composition Ti–48Al–2Cr–2Nb (at.%). Journal of Materials Science: Materials in Medicine, 21(5), 1739-1750.

[11] Beloti, M. M., Rollo, J. M. D. A., Filho, A. I., & Rosa, A. L. (2004). In vitro biocompatibility of duplex stainless steel with and without 0.2% niobium. Journal of Applied Biomaterials and Biomechanics, 2(3), 162-168.

[12] Gregorutti, R. W., Grau, J. E., Sives, F., & Elsner, C. I. (2015). Mechanical, electrochemical and magnetic behaviour of duplex stainless steel for biomedical applications. Materials Science and Technology, 31(15), 1818-1824.

[13] Abdulghani, S., & Mitchell, G. R. (2019). Biomaterials for in situ tissue regeneration: A review. Biomolecules, 9(11), 750.

[14] Codrea, C. I., Croitoru, A. M., Baciu, C. C., Melinescu, A., Ficai, D., Fruth, V., & Ficai, A. (2021). Advances in osteoporotic bone tissue engineering. Journal of Clinical Medicine, 10(2), 253.

[15] Park, S. B., Lih, E., Park, K. S., Joung, Y. K., & Han, D. K. (2017). Biopolymer-based functional composites for medical applications. Progress in Polymer Science, 68, 77-105.

[16] Ikada, Y. (2006). Challenges in tissue engineering. Journal of the Royal Society Interface, 3(10), 589-601.

[17] Battafarano, G., Rossi, M., De Martino, V., Marampon, F., Borro, L., Secinaro, A., & Del Fattore, A. (2021). Strategies for bone regeneration: from graft to tissue engineering. International Journal of Molecular Sciences, 22(3), 1128.

[18] Xu, X., Awad, A., Robles-Martinez, P., Gaisford, S., Goyanes, A., & Basit, A. W. (2021). Vat photopolymerization 3D printing for advanced drug delivery and medical device applications. Journal of Controlled Release, 329, 743-757.

[19] Bhola, R., Bhola, S. M., Liang, H., & Mishra, B. (2010). Biocompatible denture polymers-a review. Trends Biomater Artif Organs, 23(3), 129-136.

[20] Chen, G. Q., & Wu, Q. (2005). The application of polyhydroxyalkanoates as tissue engineering materials. Biomaterials, 26(33), 6565-6578.

[21] Koller, M. (2018). Biodegradable and biocompatible polyhydroxy-alkanoates (PHA): auspicious microbial macromolecules for pharmaceutical and therapeutic applications. Molecules, 23(2), 362.

[22] Dwivedi, R., Pandey, R., Kumar, S., & Mehrotra, D. (2020). Poly hydroxyalkanoates (PHA): Role in bone scaffolds. Journal of oral biology and craniofacial research, 10(1), 389-392.

[23] Siddiqui, N., Asawa, S., Birru, B., Baadhe, R., & Rao, S. (2018). PCL-based composite scaffold matrices for tissue engineering applications. Molecular Biotechnology, 60(7), 506-532.

[24] Bartnikowski, M., Dargaville, T. R., Ivanovski, S., & Hutmacher, D. W. (2019). Degradation mechanisms of polycaprolactone in the context of chemistry, geometry and environment. Progress in Polymer Science, 96, 1-20.

[25] Accardo, A., Courson, R., Riesco, R., Raimbault, V., & Malaquin, L. (2018). Direct laser fabrication of meso-scale 2D and 3D architectures with micrometric feature resolution. Additive Manufacturing, 22, 440-446.

[26] Barone, M., De Stefani, A., Baciliero, U., Bruno, G., & Gracco, A. (2020). The accuracy of jaws repositioning in bimaxillary orthognathic surgery with traditional surgical planning compared to digital surgical planning in skeletal class III patients: a retrospective observational study. Journal of clinical medicine, 9(6), 1840.

[27] Mangano, F. G., Margiani, B., Solop, I., Latuta, N., & Admakin, O. (2020). An Experimental Strategy for Capturing the Margins of Prepared Single Teeth with an Intraoral Scanner: A Prospective Clinical Study on 30 Patients. International Journal of Environmental Research and Public Health, 17(2), 392.

[28] Han, W., El Botty, R., Montaudon, E., Malaquin, L., Deschaseaux, F., Espagnolle, N., ... & Camonis, J. (2021). In vitro bone metastasis dwelling in a 3D bioengineered niche. Biomaterials, 269, 120624.

[29] Weng, W., Wu, W., Hou, M., Liu, T., Wang, T., & Yang, H. (2021). Review of zirconia-based biomimetic scaffolds for bone tissue engineering. Journal of Materials Science, 56(14), 8309-8333.

[30] Ghassemi, T., Shahroodi, A., Ebrahimzadeh, M. H., Mousavian, A., Movaffagh, J., & Moradi, A. (2018). Current concepts in scaffolding for bone tissue engineering. Archives of bone and joint surgery, 6(2), 90.

[31] Kim, H. D., Amirthalingam, S., Kim, S. L., Lee, S. S., Rangasamy, J., & Hwang, N. S. (2017). Biomimetic materials and fabrication approaches for bone tissue engineering. Advanced healthcare materials, 6(23), 1700612.

[32] LeGeros, R. Z., Lin, S., Rohanizadeh, R., Mijares, D., & LeGeros, J. P. (2003). Biphasic calcium phosphate bioceramics: preparation, properties and applications. Journal of materials science: Materials in Medicine, 14(3), 201-209.

4. Additive Manufacturing

List of abbreviations

RP - Rapid Prototyping

SSF - Solid Freeform Fabrication

AM - Additive Manufacturing

3DP Three Dimensional Printing -

ASTM - American Society for Testing and Materials

ISO - International Organization for Standardization

Three Dimensional Printing - 3DP

Material Extrusion - ME

Computed tomography - CT

Magnetic resonance imaging - MRI

Vat photopolymerization - VPP

Material jetting - MJ

Binder jetting – BJ

Sheet lamination - SL

Directed energy deposition - DED

Selective Laser Sintering - SLS

Selective Laser Melting - SLM

Direct Metal Laser Sintering - DMLS

Electron beam Melting - EBM

Laser Powder Bed Fusion - L-PBF

Electron Beam Powder Bed Fusion - EB-PBF

FDA – Food and Drug Administration

Over the past three decades, the terms *Rapid Prototyping* (RP) and *Solid Freeform Fabrication* (SFF) were used as synonyms of *Additive Manufacturing* (AM), officially approved in 2009 by the ASTM F42 Committee. Additive Manufacturing is currently the international standard term used for "those technologies that, based on a geometrical representation, create physical objects by successive addition of material", according to the official definition provided by UNI EN ISO/ASTM 52900:2017. Nowadays, Additive Manufacturing is often improperly defined as *3D printing*. However, the term *Three Dimensional Printing* (3DP) originates from patents and trademarks filed by MIT in 1989.

Additive manufacturing technologies have been developed since the first half of the '80s of the 20th century, when Charles W. Hull founded 3D Systems Inc., the first company to commercialize AM solutions and that still remains the benchmark for the AM market. In particular, the patent US-4575330-A, filed by Charles W. Hull in 1984, referring to an "Apparatus for production of three-dimensional objects from stereolithography", is recognized as the fundamental patent which highlighted the real potential of AM. From this date, other companies and universities have pursued this idea, creating systems that achieve the same result by using different technologies, [1, 2].

4.1. Application in orthopedy and dentistry

Medical applications of additive manufacturing can be classified into the following categories [3, 4]:

- Medical models for pre, intra and post operative planning and simulation, education and training (e.g. patient bronchi model in Figure 4.1);
- Medical aid and orthoses (motion guides, splints, fixators, orthopedic and orthodontic braces and appliances) for providing an external anatomic-personalized support;
- Tools and instruments with patient-specific features to improve the efficacy of a medical or surgical procedure. The Vat photopolymerization process to create clear orthodontic aligners is the largest and most successful technique used for this application;
- Prostheses for tissue replacement. This class also includes dental applications such as crowns and bridges;
- Biomanufacturing, i.e. a combination of additive manufacturing and tissue engineering, for tissue regeneration (e.g. biodegradable stent for tracheomalacia in Figure 4.1).

Figure 4.1 - Biodegradable stent for tracheomalacia (condition of excessive collapse of the airways during breathing that can lead to cardiopulmonary arrest) mounted on the patient bronchi model. Stent was manufactured by Prosilas Srl (Civitanova Marche, Italy) and implanted at the Bambino Gesù Children's Hospital (Rome, Italy). Adapted from https://www.prosilas.com/en/biomedical-2/.

4.2. From 3D to 2D problem

Additive Manufacturing is based on the consideration that any object can be figured as a union of many layers of thickness ΔS. The fabrication of a layer, even reducing the thickness, requires a finite time different from zero. Thus, the fabrication of an object using layers implies that the obtainable surface (Σ) of the object produced by layers (whose profile is a broken line), can only be an approximation of the designed surface (S). This approximation becomes more refined increasing the number of layers (Eq. 4.1):

$$\lim_{\Delta S \to 0} \Sigma = S \tag{4.1}$$

However, this leads to an increase of the production time, and therefore of the production cost, as demonstrable considering (Eq. 4.2):

$$\lim_{\Delta s \to 0} \frac{h}{\Delta s} = \infty \tag{4.2}$$

Where h is the height of the part and $\frac{h}{\Delta s}$ is the number of layers (n) required to complete the object of height h, resulting from the *slicing* of the object. *Slicing* is the division of three-dimensional virtual model in a certain number of parallel *slices*, perpendicular to the Z axis, which will then compose the physical prototype

The surface effect represented in Figure 4.2 is known as *staircase* and is due to the fabrication of layers with a finite thickness. Additive manufacturing systems operate with fixed *slicing*, whereas it would be appropriate to adopt an adaptive *slicing*, which modifies the thickness of the layers according to the curvature, to reduce the presence of material shortage or excess after the manufacturing.

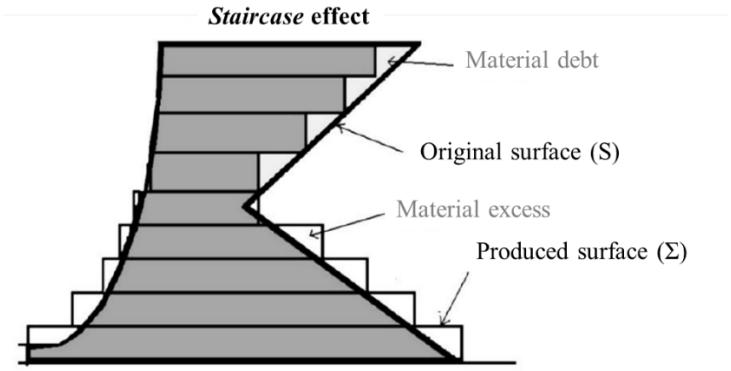

Figure 4.2- Schematic of staircase effect, due to the approximation of manufactured part (surface Σ) respect to the ideal part (surface S). Adapted from [1].

Furthermore, since the total fabrication time is given by the time of layer consolidation and the repositioning of the printing head, it is clear that there is another lower limit in the AM processes. This limit is quantified as the product of the time required to bring the system to the conditions of making a new layer, for the number of layers. Thus, the total construction time (t_c) can be calculated as (Eq. 4.3):

$$t_c = \sum_1^n t_i \tag{4.3}$$

where $t_i = \frac{A_i}{vD} + t_d$

• t_i = time to complete the i-th layer;

• A_i = area of the i-th layer;

• v = average scanning speed of the generating head. In the case of a laser it is the speed of the spot; in *Material Extrusion* (ME) it is the extrusion speed;

• D = diameter of the area currently subject to the consolidation, i.e. the diameter of the spot in the case of laser, diameter of the extrudate in ME;

• t_d = time required to reposition the system to the conditions for creating a new layer after the completion of the previous one; i.e. the time necessary for the redistribution of a layer of virgin material, the repositioning of the head and the eventual cycle of heating;

Thus, the use of additive manufacturing for the fabrication of a massive part without particularly sophisticated shape, results to be always not convenient compared to traditional production processes. This leads to a delimitation of the application field of these technologies, that must be centered on the term *freeform*, in which the complexity of production precludes the use of traditional technologies. On the other hand, the layer-by-layer manufacturing presents the enormous advantage of transforming the problem of a 3D complex part production, in a two-dimensional problem: the fabrication of a layer [1].

4.3. Phases of AM process for Bone Tissue Engineering

After the diagnosis, first step for any medical process, objective and expected outcome of the AM application are determined. The phases of the standard approach used by additive manufacturing process for typical biomedical components, can be summarized as follows:

1. Patient anatomical data are obtained via medical imaging, such as computed tomography (CT), magnetic resonance imaging (MRI) or ultrasound, in order to create an image-based CAD model. These imaging methods produce continuous volumetric data (voxel-based data), which provide the input data for the digital model generation. These datasets often need considerable processing to

extract the relevant sections before it can be built as a model or further incorporated into a product design. There are a few software systems that can process medical data in a suitable way, and a range of applications have emerged (e.g. Materialise) [2]. The achieving of an analytical image of the damaged area using segmentation algorithms, allows to produce computational tissue models, distinguish heterogeneous tissue types and show vascular structure [5].

2. The component is designed by CAD and then converted into a unmodifiable STL model. The various CAD software use different algorithms to represent the solid object. For consistency reasons, the CAD project is converted to a standardized exchange format, accepted by all AM processes. This graphic exchange standard has a Solid To Layer (STL) extension.

3. The STL model is processed by the machine to define the orientation of the part, the building direction and supports. The external surface of the solid is decomposed into a set of elementary triangles. The higher the accuracy required, the smaller the triangles size must be. In particular, smaller triangles are required to fit curved surfaces and near the edges. Therefore, according to the quality of the object to be obtained, the resolution is customized in terms of number of triangles, by affecting processing time and the file heaviness. Low resolution allows short production time, however the manufactured object will present worse aesthetic qualities.
   Additionally, plans positioning is important as it determines processing time and accuracy of the product. It is generally advisable to orient the part so that the direction of least encumbrance of part coincides with the Z axis of the machine. In fact, the model is often less accurate and weaker according to the direction of growth (Z axis).

4. The virtual model in STL format is sliced and each individual slice constitutes the input for the control of the additive manufacturing machine. The *slicing* affects the dimensional accuracy, the surface finishing, the production and post-process time and cost of the part, being the layer thickness defined a priori and constant during the fabrication process.

5. When all these operations have been defined, the machine can start with the production of the part. Ultimately, it can be argued that the creation of a physical model by additive manufacturing is based on the physical approximation of a virtual model, which is in turn approximated, and on which errors due to the resolution of the machine used, are grafted. Nevertheless, the results obtained are acceptable in the measure in which the component respects the geometric, dimensional and mechanical characteristics of the physical object to realize, according to its application.

6. The object produced must be post-treated to improve its mechanical and aesthetic characteristics.

However, the use of these technologies for the construction of scaffolds presents further complications related to the increase in the parameters to control during the process. For example, the single layer is not homogeneous but rather can be assimilated to a network, with alternating pores and struts, oriented in the space. Therefore, the bone scaffold production, compared to industrial component produced by additive manufacturing, evidences higher levels of complexity.

4.4. AM Technologies

The ASTM and ISO standardization organization categorizes the AM process into seven different categories: powder bed fusion (PBF), material extrusion (ME), VAT photopolymerization (VPP), material jetting (MJ), binder jetting (BJ), sheet lamination (SL) and directed energy deposition (DED). Each category includes many different vendors, solutions and material options, as reported in Table 4.1 [4].

Table 4.1 – AM technologies with process description, material form and typology (metal, polymer or ceramic). +++, widely available/many studies exist; ++, available/several studies exist; +, R&D phase/studies exist; -, no studies exist. Adapted from [4].

AM technology	Process description	Material			
		Form	Typology		
			Metal	Polymer	Ceramic
Powder bed fusion (PBF)	Thermal energy melts regions of a powder bed	powder	+++	+++	+
Material extrusion (MEX)	Material dispensed through a nozzle	filament, pellets, paste	+++	++	++
VAT photo-polymerization (VP)	Liquid photopolymer in a vat is cured by light	liquid	+++	+	++
Material jetting (MJ)	Droplets of material are selectively deposited	liquid	+++	+	+
Binder jetting (BJ)	A liquid bonding agent is selectively deposited	powder	+++	++	+
Sheet lamination (SL)	Sheets of material are bonded	sheets	++	++	-
Directed energy deposition (DED)	Focused thermal energy used to fuse materials by melting when depositing	powder, wire	-	+++	+

Powder bed fusion, material extrusion and VAT photopolymerization are well-established processes for all the categories of medical and dental applications [4]. The doctorate research reported was performed by powder bed fusion and vat photopolymerization using the biomaterial illustrated in the previous chapter.

4.4.1. Powder Bed Fusion

Powder Bed Fusion, defined as “an additive manufacturing process in which thermal energy selectively fuses regions of a powder bed” by the fixed designation ASTM F2792-12a [7], encompasses the technologies previously mentioned as *Selective Laser Sintering (SLS)*, *Selective Laser Melting (SLM)*, *Direct Metal Laser*

Sintering (DMLS) and *Electron beam Melting (EBM)*, which differ in energy source (laser or electron beam), energy density per unit of volume or surface, process parameters and particle size.

4.4.1.1. Sintering

Sintering indicates the fusion of powder particles in their "solid-state" (without melting) at elevated temperatures, i.e. $0.5T_{melting} \div T_{melting}$, where $T_{melting}$ is the melting temperature. The driving force for solid-state sintering is the minimization of total free energy of the powder particles and applies to all material classes (metals, polymers and ceramics). When particles are joined together at elevated temperatures under the $T_{melting}$ (Figure 4.3), the total surface area decreases, thus surface energy decreases and the rate of sintering slows. To achieve very low porosity levels, long sintering times or high sintering temperatures are required. As total surface area in a powder bed is a function of particle size, the driving force for sintering is directly related to the surface area to volume ratio for a set of particles (the larger the surface area to volume ratio, the greater the free-energy driving force). Thus, smaller particles experience a greater driving force for necking and consolidation, and hence, smaller particles sinter more rapidly and initiate sintering at a lower temperature than larger particles [1, 2].

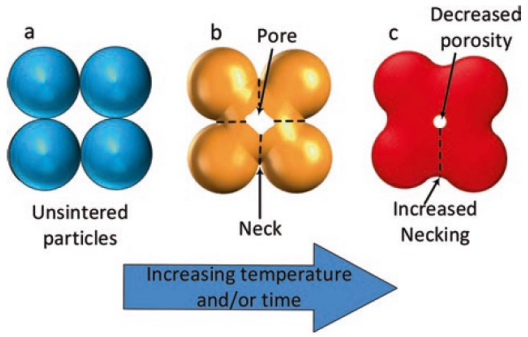

Figure 4.3 - Solid-state sintering. (a) Closely packed particles prior to sintering. (b) Particles agglomerate due to diffusion at temperatures above one half of the absolute melting temperature, as they seek to minimize free energy by decreasing surface area. (c) As sintering progresses, neck size increases and pore size decreases. From [2] with permission.

However, even at temperatures approaching the melting temperature, diffusion-induced solid-state sintering is the slowest mechanism for selectively fusing regions of powder within a PBF process. For AM, the shorter the time it takes to form a layer, the more economically competitive the process becomes. Since the time it takes for fusion by sintering is typically much longer than for fusion by melting, few AM processes use sintering as a primary fusion mechanism. Sintering, however, is still important in most thermal powder processes, as if affects the build in secondary ways:

1) If the manufacturing powder within the build platform is held at an elevated temperature, the powder bed particles will begin to sinter to one another. This is typically considered a negative

effect, as agglomeration of powder particles means that each time the powder is recycled the average particle size increases, inducing physical characteristics change and the probably deterioration of manufactured part quality [1, 2]. In addition, if the sintered particles agglomeration remains trapped inside scaffold pores, they can occlude partially and sometimes totally the pores and could not be removed even after repeated blasting processes. Unremoved residual powder could have effect on mechanical and biological behavior of scaffold;

2) Rapid fusion of a powder bed makes it difficult to achieve 100% dense, porosity-free parts. Thus, a feature of many parts built using PBF techniques (especially for polymers) is distributed porosity throughout the part. This is typically detrimental to the intended part properties. However, this uneven porosity can be controlled, by carefully controlling the part bed temperature, cooling rate, scanning speed, laser spot and other processing parameters [1, 2], and allows a second level of porosity to scaffold. In addition to designed macro-porosity, micro-porosity helps degradable polymer scaffold enhancing cell interaction and degradation rate.

4.4.1.2. Melting

Full melting is the mechanism most commonly associated with PBF processing of tissue engineering metal alloys and polymers. In these materials, the entire region of material subjected to impinging heat energy is melted to a depth exceeding the layer thickness. Thermal energy of subsequent scans of a laser or electron beam is typically sufficient to remelt a portion of the previously solidified solid structure (up to 5-6 layers); and thus, this type of full melting is very effective at creating high-density structures from tissue engineering metals and polymers. An important aspect for achieving maximum part density in PBF technologies is particle size distribution, which should be Gaussian to promote the compaction. A higher packing density of the powder bed is preferred for powder bed fusion processes because of the lower internal stresses, part distortion, porosity and surface roughness in the built part. The packing density of the powder bed is significantly affected by the particle morphology, size and distribution [8].

4.4.1.3. Powder recycling

To achieve a high level of feedstock utilization, unmelted powder can be used for subsequent builds. However, the physical and chemical properties of powder particles may change during the build process, which may cause defects and produce parts out of specifications. When reusing powder, oxygen contamination and loss of elemental alloys are other potential problems. The oxygen affects the mechanical properties, corrosion resistance, and powder recyclability. The loss of elemental alloys is related to the lower boiling point of alloy elements. For instance, in Ti-6Al-4V at melting temperature, both Aluminum and Vanadium can partially vaporize. As a consequence, alloy feedstocks are often prepared with higher than specification percentages of low-temperature alloying elements such that after melting, and partial vaporization, the chemical composition

in fabricated parts falls within acceptable ranges. Additionally, to help prevent significant changes in chemical composition, reused powder should be mixed with new virgin powder [2].

4.4.1.4. Process parameters

The PBF process parameters can be lumped into four categories:

1) laser-related parameters (laser power (P), spot size, pulse duration, pulse frequency, etc.);
2) scan-related parameters (scan speed (v), scan spacing (h), and scan pattern);
3) powder-related parameters (particle shape, size and distribution, powder bed density, layer thickness (t), material properties, etc.);
4) temperature-related parameters (powder bed temperature, powder feeder temperature, temperature uniformity, etc.). It should be noted that most of these parameters are strongly interdependent and are mutually interacting.

A number of key variables defined by the processing parameters can be used to characterize the process, as [8]:

Volumetric energy density (E_V), the energy conveyed by the laser beam per unit volume of material (J/mm^3) (Eq. 4.4):

$$E_v = \frac{P}{v\,h\,t} \tag{4.4}$$

Surface energy density (E_s), the energy density applied to the surface of the powder bed (J/mm^2) (Eq. 4.5):

$$E_s = \frac{P}{v\,h} \tag{4.5}$$

Liner energy density (LED), the power input per unit speed (J/mm) (Eq. 4.6):

$$LED = \frac{P}{v} \tag{4.6}$$

where P is the laser power, v the laser scanning speed, t the layer thickness and h the hatching distance. However, the depth of the melted zone by the laser or electron beam path is in the range of 5-6 layer thickness. Therefore, the single-layer thickness (t) does not represent a significant value for data comparison, due to dependence of the actual melted layer thickness on laser or electron beam power and scanning speed. As a consequence, E_v does not effectively correspond to the energy absorbed by the unit volume of the material.

4.3.1.1. Laser Powder Bed Fusion vs Electron Beam Powder Bed Fusion

Prior to 2014 there were only two major producers of polymer L-PBF machines, EOS and 3D Systems. The expiration of key patents in 2014 opened the door for many new companies to enter the marketplace. On the other hand, there are many companies which make commercially available L-PBF systems for metal: EOS

(Germany), Renishaw (UK), Concept Laser (Germany), SLM Solutions (Germany), Realizer (Germany), 3D Systems (France/USA), Trumpf (Germany), Additive Industries (Netherlands), Velo3D (USA), Farsoon (China), and others are actively competing for market share [2]. It is necessary to highlight that the market has an high instability with high frequency of born and death enterprises.

L-PBF system composition is illustrated in Figure 4.4:

1) Powder delivery system, comprising a device to supply powder, a coater to create the powder layer and a piston that holds the fabricated part;
2) Energy delivery system, made up of a laser and a scanner system with optic galvanometer that enable the delivery of a focused spot to all points of the build platform.
3) A flow of gas (usually nitrogen or argon) passes over the powder bed to protect the part from oxygen and to clear any "spatter" and metal fumes created by the laser.

During production, the laser executes a scanning or exposure strategy. The strategies associated with the laser path are characterized by the length, direction, and separation or superposition (hatch spacing) of neighboring scan vectors [9].

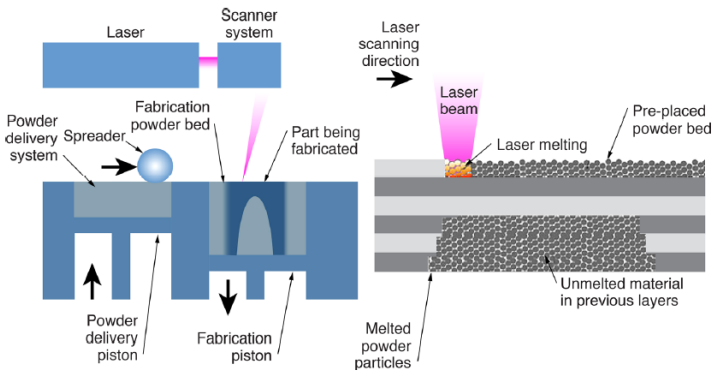

Figure 4.4 - Schematic overview of the laser powder bed fusion process both at the machine and powder scales.

Electron Beam Powder Bed Fusion (EB-PBF), in contrast to laser-based systems, uses a high-energy electron beam to induce fusion between metal powder particles. This process, developed at Chalmers University of Technology (Sweden), was commercialized by Arcam AB (Sweden) in 2001 and now owned by GE.

Similarly to L-PBF, in the EB-PBF process, a focused electron beam scans across a thin layer of pre-laid powder, causing localized melting and resolidification per the slice cross-section [2].

However, while laser beam heats the powder when photons are absorbed by powder particles, electron beam heats powder by transfer of kinetic energy from incoming electrons into powder particles. Thus, EB-PBF can only be used to process conductive materials (e.g., metals), whereas lasers can be used with any material that absorbs energy at the laser wavelength (e.g., metals, polymers, and ceramics).

The principle of EB-PBF process is illustrated in Figure 4.5. Electrons are emitted from a heated tungsten filament (cathode) (arrow 1 in Figure 4.5A). The accelerating voltage between the cathode and anode is usually of about 60 kV. In contrast to the SLM method, in which the detection and focus of the photons are conducted

by mirrors, in the EBM system, the electron beam is focused and oriented by electromagnetic lenses [10]. There are three magnetic lenses in the electron column, including an astigmatism lens and focus lens, and the deflection coils control the direction of the electron beam. The astigmatism lens (arrow 2 in Figure 4.5A) controls circular beam with a Gaussian energy distribution, while the focus lens (arrow 3 in Figure 4.5A) focuses the beam to the required diameter and the deflection coil (arrow 4 in Figure 4.5A) deflects the focused beam to the building area, according to a sliced geometry. There are two hoppers (arrow 5 in Figure 4.5A) to hold the stock material and the rake is used to spread the powder over the build area (arrow 6 in Figure 4.5A). The build table (arrow 7 in Figure 4.5A) moves down the Z-axis as the build progresses. During the process, each layer is first preheated through a series of defocused beam passages at high power and high speed, to sinter the particles. Sintering improves powder thermal conductivity and mechanical strength, thus allowing production of parts with a reduced number of supports or even without any supporting structure. The power and the scan speed are decreased in the subsequent melting step and the entire process takes place under a vacuum of 10^{-4} mbar in the chamber and 10^{-6} mbar in the gun. After building, the part is left to cool down under an increased helium pressure. At the end of the process, when the part is removed from the building chamber, a soft agglomerate powder adheres to the fabricated part and covers it completely (Figure 4.5B). This agglomerate is called breakaway powder, and it is removed by means of sandblasting, using the same powder used in the EB-PBF process. Since there is no remarkable oxygen uptake inside the build chamber during the melting process, the unused powder can be recycled several times without any alteration of its chemical composition or physical properties [2, 11-13].

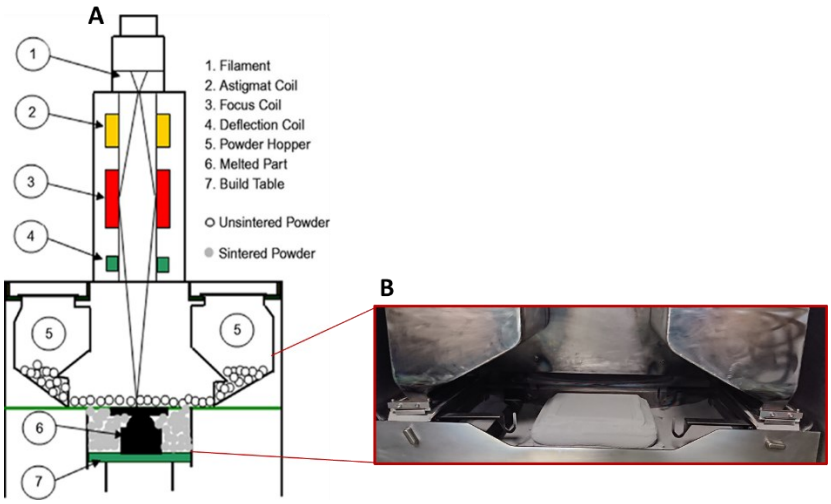

Figure 4.5 - Schematic of an EB-PBF apparatus (A), from [12], and detail of breakaway powder (B).

Although feedstock particles for EB-PBF are typically fine, with an average size around 70 μm (typical size range: 45 ÷ 105 μm), they are sensibly larger than those commonly used for L-PBF, whose average size is around 30 μm (typical size range: 15 ÷ 45 μm). EB-PBF still presents some limitations, such as residual surface roughness. The surface roughness of the finished part depends on many variables, including powder size, beam

diameter, sample geometry, and various processing parameters, especially layer thickness. On average, the surface roughness is higher for EB-PBF parts than for L-PBF parts as a result of larger powder size, beam diameter, and layer thickness. Typical values of Ra approach 25 ÷ 35 μm for EBM and 10 ÷ 12 μm for L-PBF. It is worth noting that the EB-PBF technique produces rougher surfaces with a rippled exterior appearance in comparison to the L-PBF method (Figure 4.6) [10]. For different Ti-6Al-4V porous surfaces produced by the EB-PBF process, Ponader et al. [15] found that cell proliferation decreased significantly on porous surfaces with higher Ra values, and the best surface roughness for cell proliferation was Ra ≤ 24.9 mm.

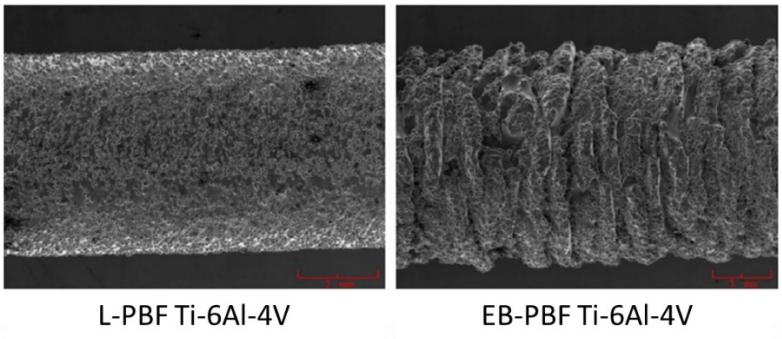

Figure 4.6 - Comparison of surface roughness on cylinders made by different methods: (a) L-PBF, (b) EB-PBF. Adapted from [10].

4.4.2. Vat Photopolymerization

Stereolithography was the first type of Vat Photopolymerization (VPP) process and was developed by Charles Hull as an extension of the work he had done previously with photopolymers. VPP processes were the first commercialized AM technology and they continue to be broadly used across many industries and applications. Laser scan VPP creates solid parts by selectively solidifying a liquid photopolymer resin using an UV laser. The part being built rests on a platform that is dipped into the vat of resin, as shown schematically in Fig. 4.7. After each slice is created, the platform is lowered, the surface of the vat is recoated, and then the laser starts to trace the next slice of the CAD model, building the prototype from the bottom up. After building, the part must be cleaned, post-cured, and finished. This technology allows the highest resolution among all the AM techniques, with average resolution approximately 150 μm [2].

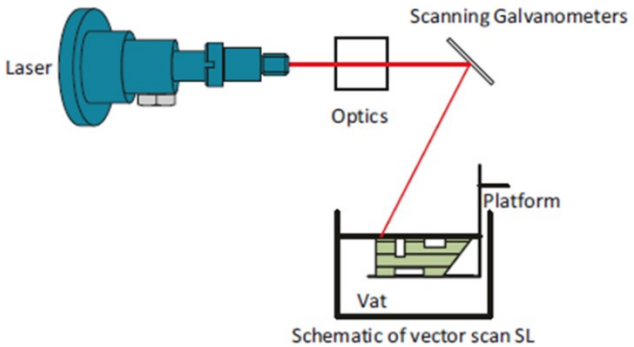

Fig. 4.7 - Schematic diagrams of photopolymerization process approaches. Adapted from [2].

4.5. AM challenges

While a number of biomaterials are accepted by the FDA for use in medical applications, there are still questions regarding the acceptability of additively manufactured biomaterials. Approval and certification of ASTM and ISO will certainly help to pave the way toward FDA approval, but this can be a very long and laborious process. In addition, the medical industry is understandably conservative about the introduction of these new technologies. Furthermore, many hospitals around the world treat patients according to their level of insurance coverage. Similar to the aforementioned issue of approvals, insurance companies need protocols for coverage using AM as a stage in the treatment process [2]. All these issues must overcome to legitimize AM in the medical industry.

References

[1] Gatto, A., Bassoli, E., Denti, L., Iuliano, L., Produrre, Pitagora Editrice Bologna, 2017.

[2] Gibson, I., Rosen, D. W., Stucker, B., Khorasani, M., Rosen, D., Stucker, B., & Khorasani, M. (2021). Additive manufacturing technologies (Vol. 17). Cham, Switzerland: Springer.

[3] Tuomi, J., Paloheimo, K. S., Vehviläinen, J., Björkstrand, R., Salmi, M., Huotilainen, E., ... & Mäkitie, A. A. (2014). A novel classification and online platform for planning and documentation of medical applications of additive manufacturing. Surgical innovation, 21(6), 553-559.

[4] Salmi, M. (2021). Additive manufacturing processes in medical applications. Materials, 14(1), 191.

[5] Top, N., Şahin, İ., Gökçe, H., & Gökçe, H. (2021). Computer-aided design and additive manufacturing of bone scaffolds for tissue engineering: state of the art. Journal of Materials Research, 36(19), 3725-3745.

[6] Pei, E., Monzón, M., & Bernard, A. (Eds.). (2019). Additive manufacturing-Developments in training and education. London: Springer International Publishing.

[7] Standard terminology for additive manufacturing technologies: designation F2792-12a. Current edition approved March 1, 2012. Published March 2012. Originally approved in 2009. Last previous edition approved in 2012 as F2792–12. DOI: 10.1520/F2792-12A.

[8] Sun, S., Brandt, M., & Easton, M. J. L. A. M. (2017). Powder bed fusion processes: An overview. Laser Additive Manufacturing, 55-77.

[9] King, W. E., Anderson, A. T., Ferencz, R. M., Hodge, N. E., Kamath, C., Khairallah, S. A., & Rubenchik, A. M. (2015). Laser powder bed fusion additive manufacturing of metals; physics, computational, and materials challenges. Applied Physics Reviews, 2(4), 041304.

[10] Ataee, A., Li, Y., Song, G., & Wen, C. (2017). Metal scaffolds processed by electron beam melting for biomedical applications. In Metallic Foam Bone (pp. 83-110). Woodhead Publishing.

[11] Ameen, W., Al-Ahmari, A., Mohammed, M. K., & Mian, S. H. (2018). Manufacturability of overhanging holes using electron beam melting. Metals, 8(6), 397.

[12] Singh, D. D., Mahender, T., & Reddy, A. R. (2021). Powder bed fusion process: A brief review. Materials Today: Proceedings, 46, 350-355.

[13] Galati, M., & Iuliano, L. (2018). A literature review of powder-based electron beam melting focusing on numerical simulations. Additive Manufacturing, 19, 1-20.

[14] Nouri, A., & Sola, A. (2020). Electron beam melting in biomedical manufacturing. In Metallic Biomaterials Processing and Medical Device Manufacturing (pp. 271-314). Woodhead Publishing.

[15] Ponader, S., Vairaktaris, E., Heinl, P., Wilmowsky, C. V., Rottmair, A., Körner, C., ... & Nkenke, E. (2008). Effects of topographical surface modifications of electron beam melted Ti-6Al-4V titanium on human fetal osteoblasts. Journal of Biomedical Materials Research Part A: An Official Journal of The Society for Biomaterials, The Japanese Society for Biomaterials, and The Australian Society for Biomaterials and the Korean Society for Biomaterials, 84(4), 1111-1119.

5. Characterization techniques

List of abbreviations

5.1. Scanning Electron Microscopy
- 5.1.1. SEM operation and image formation
- 5.1.2. Electron beam critical parameters
- 5.1.3. Electron beam - matter intearction
  - *5.1.3.1. Secondary electrons*
  - *5.1.3.2. Backscattered electrons*
- 5.1.4. SEM layout
  - *5.1.4.1. Electron gun*
  - *5.1.4.2. Electromagnetic lenses*
  - *5.1.4.3. Scanning coils*
  - *5.1.4.4. Detectors*
- 5.1.5. Image optimization
- 5.1.6. Sample preparation

5.2. Energy dispersive spectroscopy
- 5.2.1. Generation of X-Ray
  - *5.2.1.1.*Continuum X-Ray (Bremsstrahlung)
  - *5.2.1.2.*Characteristic X-Ray
- 5.2.2. EDS Analysis
  - *5.2.2.1.* Qualitative analysis
  - *5.2.2.2.*Quantitative analysis

5.3. X-Ray Diffraction
- 5.3.1. Geometry of Crystal
- 5.3.2. Diffraction from Crystals
- 5.3.3. X-ray diffractometer
- 5.3.4. Diffraction measurements
  - *5.3.4.1. Phase Identification*
  - *5.3.4.2. Quantitative analysis*
- 5.3.5. Sample preparation

5.4. X-ray micro Computed Tomography
- 5.4.1. Image formation
  - *5.4.1.1. Absorption Contrast*
  - *5.4.1.2. Phase Contrast*
- 5.4.2. From Projections to the 3D Analysis
  - *5.4.2.1. Sample preparation*
  - *5.4.2.2. Acquisition*
  - *5.4.2.3. Reconstruction*
  - *5.4.2.4. Segmentation*
  - *5.4.2.5. Quantification*

5.5. Mechanical tests
- 5.5.1. Compressive test
- 5.5.2. Incompressible materials
  - *5.5.2.1. Porous and cellular metal specimen*

List of abbreviations

SEM - Scanning Electron Microscope

EDS - Energy dispersive spectroscopy

SE - Secondary electrons

BSE - Backscattered electrons

FEG - Field emission gun

ETD - Everhart-Thornley detector

TTLD - Through the lens detector

SSD - Solid state detector

WD - Working distance

XRD - X-Ray diffraction

XμCT - X-ray micro Computed Tomography

ANSI - American National Standards Institute

ISO - International Standardization Organization

MG-63 - human osteosarcoma cells

hMSCs - human Mesenchymal Stem Cells

NIH-3T3- Murine fibroblast cell line

RS - Rapidly self-renewing

FC - Flattened cells

DMEM -FDulbecco Modified Eagle's Medium

PBS - Phosphate buffered saline

5.1. Scanning electron microscopy

5.1.1. SEM operation and image formation

Scanning Electron Microscope (SEM) uses a focused beam of electrons to create a magnified image of a sample, as illustrated in Figure 5.1. The electron beam is generated by an electron gun and is focalized on sample surface by electromagnetic lenses (condenser and final lens). Through deflection coils, the electron beam is scanned in a regular pattern across the surface of the sample and the electrons that come out of the sample are used to create the image. Signals generated from the specimen are collected by an electron detector, converted to photons via a scintillator, amplified in a photomultiplier, and converted to electrical signals to modulate the intensity of the image on the viewing screen. SEM is a sequential image forming system: the image is formed point by point, without image forming lenses.

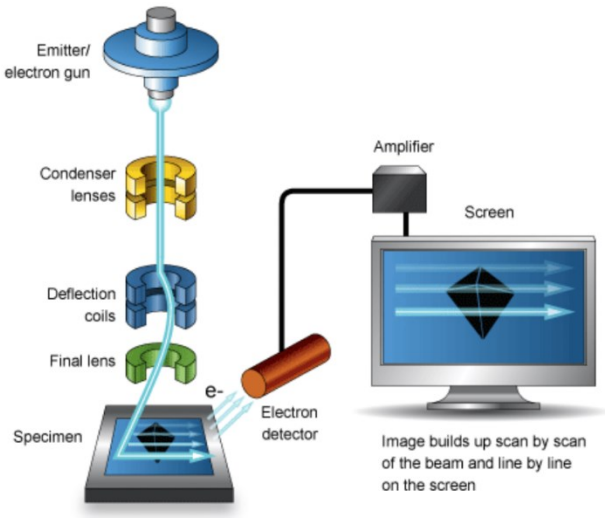

Figure 5.1 – Schematic of scanning Electron Microscope operation.

5.1.2. Electron beam critical parameters

SEM resolution refers to the size of the finest details that can be observed and is limited by the spot size of the beam (or electron probe size (d_p), defined as the diameter of the final beam at the surface of the specimen). Details smaller than spot size cannot be resolved, therefore spot size must be as small as possible (Figure 5.2). In the SEM, electron lenses are used to produce a small spot size at the sample surface.

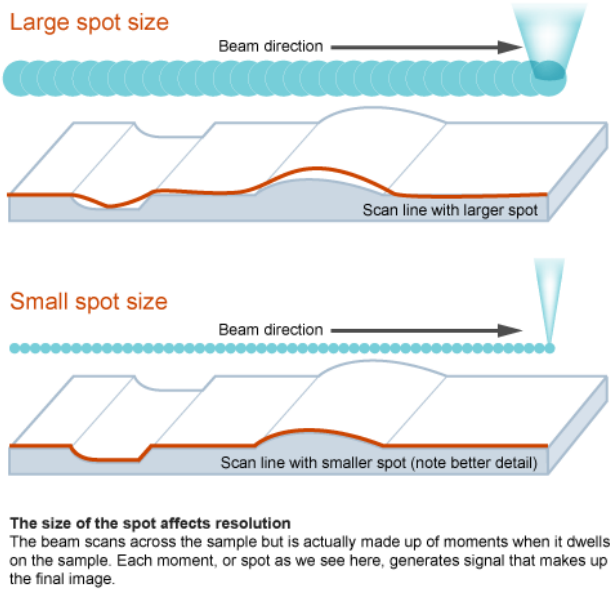

Figure 5.2 – Schematic of size of spot affecting resolution: smaller spot size allows to note better detail respect to larger spot.

In addition to the electron probe size, other critical parameters of electron beam influence the quality of image, as showed in Figure 5.3:

- Electron beam accelerating voltage V_0 (kV) is the accelerating voltage of the electron gun. At low accelerating voltages (≤ 5 kV), the beam interaction with the specimen is confined to regions very close to the surface. This provides an image which is rich in surface detail compared to those obtained at higher accelerating voltages (15–30 kV), where the beam penetrates beneath the surface and the emerging signal electrons mostly carry information about the interior of the sample;
- Electron probe current i_p (1 pA -1 μA) is the current that impinges upon the specimen and generates the various imaging signals. For the best image visibility and quality, large beam currents i_p are required. Unless the contrast between an image feature and background is distinguishable above random signal fluctuations (noise), detail cannot be observed even if the spot size is small enough for it to be easily resolved. Large beam currents are also necessary for successful X-ray energy dispersive spectroscopy (EDS) because only a small fraction of beam interactions result in X-ray emission;
- Electron probe convergence angle α_p (10^{-4} - 10^{-1} rad) is the half-angle of the cone of electrons converging onto the specimen. For the best depth of field, α_p must be as small as possible. By making the beam convergence angle low, the beam diameter changes only a little over a long vertical distance and so features on the surface at different heights will all appear to be in focus at the same time.

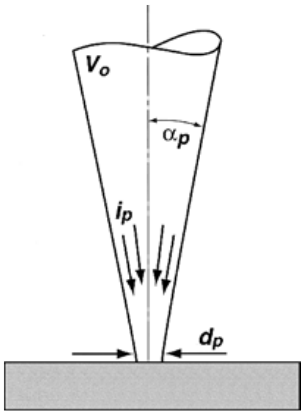

Figure 5.3 - Electron beam critical parameters which influence image quality: d_p - electron probe diameter, i_p - electron probe current, α_p - electron probe convergence and V_0 - electron beam accelerating voltage.

In most cases, the benefits of all these electron beam critical parameters are needed simultaneously; however, some effects tend to be mutually exclusive: i_p is inescapably reduced when d_p and α_p are reduced. When the voltage is lowered, d_p increases and i_p decreases. The four beam parameters must be chosen to obtain appropriate imaging conditions in each situation.

5.1.3. Electron beam-matter interaction

Electrons are charged particles that strongly interact with the matter. Elastic scattering occurs when the incident electron beam is attracted by the electrostatic potential of the nucleus. Negligible energy loss in the incident electron and high scattering angle are allowed in such interaction. Inelastic scattering involves an energy transfer between the incident electron and the electron cloud of the sample atoms and low scattering angle. The combined effect of elastic and inelastic scattering processes is to distribute the beam electrons over a three-dimensional interaction volume (Figure 5.4) with dimensions in the micrometer range, from which signals are generated.

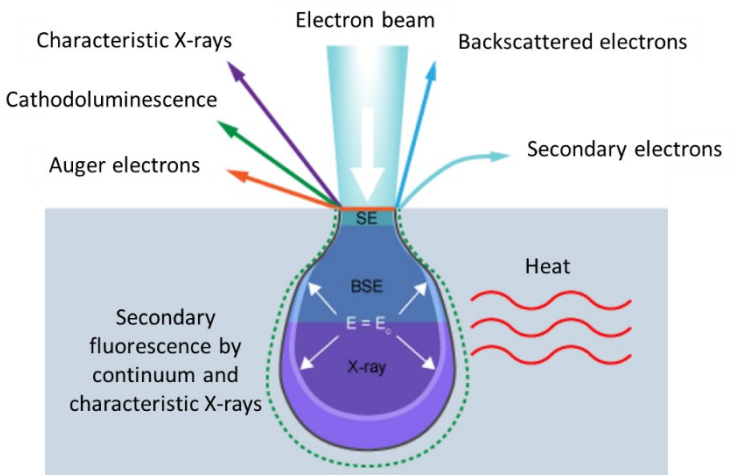

Figure 5.4 – Schematic of signals from interaction volume.

The main signals used in conventional SEM are secondary electrons (SE), backscattered electrons (BSE) and characteristic X-ray. Characteristic X-ray contributes to Energy Dispersive Spectroscopy (EDS) analysis together with Bremsstrahlung radiation and are discussed more in detail in the next paragraph. Furthermore, the energy of electrons which are not emitted from the sample will contribute to sample heating. It can be negligible for metals, while is considerably high in non-conducting samples.

5.1.3.1. Secondary electrons

Secondary Electron (SE), generated from inelastic scattering, are emitted with energy lower than 50 eV (Figure 5.5). SE are easily reabsorbed by matter, thus only SE generate at low depth (10 nm) are able to be emitted. These effects are connected to little interaction volume, that makes SE able to provide morphological information of the sample. It is possible to define the secondary electron emission coefficient δ as (Eq. 5.1):

$$\delta = \frac{I_{SE}}{I_0} \tag{5.1}$$

where:

- I_0 is the beam current injected into the specimen;
- I_{SE} is the secondary electron current passing out of the specimen.

Secondary electron yield δ does not have a strong dependence on the sample atomic number (Figure 5.6), thus they carry a low compositional contrast information. Secondary electron, due to their small energy, can leave the specimen from a small exit depth. Since the sample tilting with respect to the beam increases the path length of the primary beam inside the exit depth, the SE increases with the tilt angle (Figure 5.7A) and SE images show a topographical contrast.

5.1.3.2. Backscattered electrons

Backscattered electrons (BSE) are electrons of incident beam deflected by high angle elastic scattering (> 90°) and emitted from a depth of 0.5-1 μm by surface, being literally diffused back. BSE have an energy ranging from 50 eV to the value of the incident beam (E_0) one, as showed in Figure 5.5, depending on the number of scattering events and on the energy lost in each scattering event.

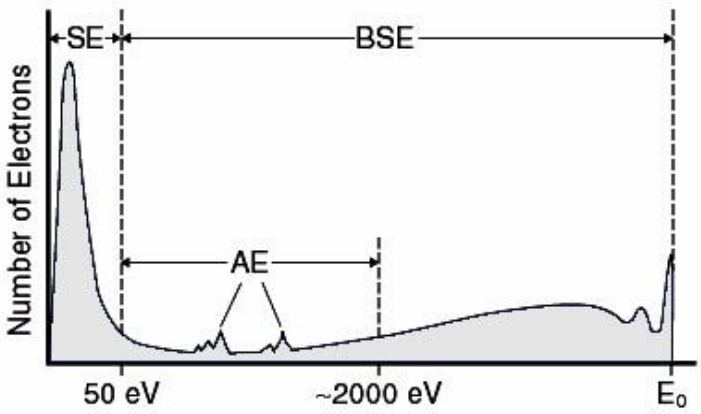

Figure 5.5 – Low-energy SE (Secondary electrons) and high-energy BSE (Backscattered electrons) are the signals mainly used in a conventional SEM (A).

Fraction of the backscattered electrons is quantified by the backscattering emission coefficient η (Eq. 5.2):

$$\eta = \frac{I_{BSE}}{I_0} \tag{5.2}$$

where:

- I_0 is the beam current injected into the specimen
- I_{BSE} is the backscattered electron current passing out of the specimen.

There is a monotonically increasing dependence of η from atomic number (Z) at primary beam energies higher than 5 KeV (Figure 5.6). Thus BSE carry compositional information of the sample.

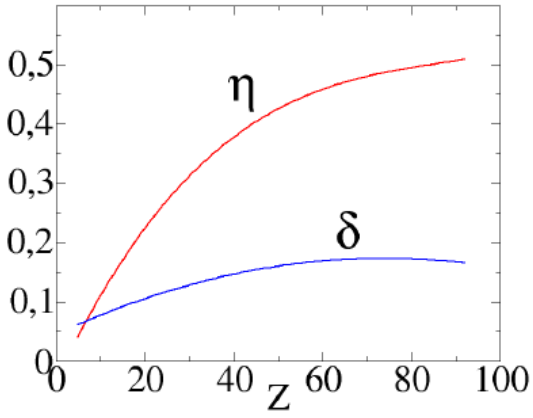

Figure 5.6 – Dependence of secondary electron emission coefficient δ and backscattering emission coefficient η from sample atomic number (Z).

Sample tilting increases escaping probability and BSE generation. Different surface tilt generates topographic contrast. However, dependence of BSE emission from tilt is very low (Figure 5.7B), thus BSE allow a low resolution topographic contrast.

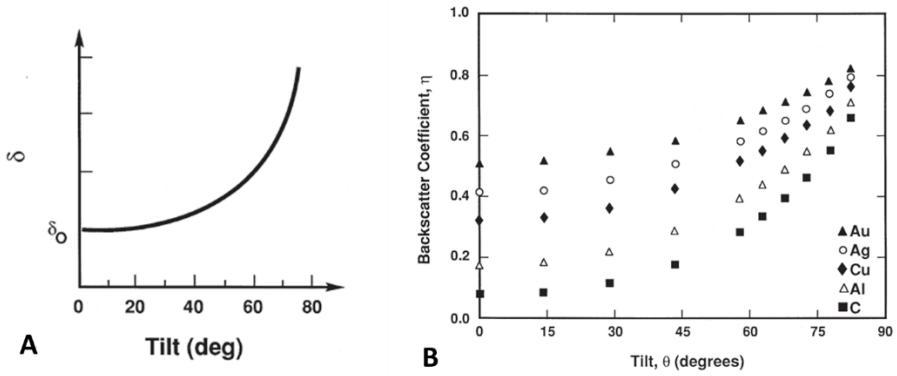

Figure 5.7 – Dependence of SE coefficient η (A) and BSE coefficient δ (B) from sample tilt angle.

5.1.4. SEM layout

5.1.4.1.1. Electron gun

Electron gun (Figure 5.8) provides a stable beam of electrons of adjustable energy. Electron guns can be classified into two types: thermionic gun and field emission gun (FEG). In thermionic emission, a metal filament is heated by a current and allows the emission of thermally excited electrons, while in FEG, electrons are pulled off from a pointed single crystal by a strong electrostatic field. Older SEMs employ tungsten or LaB6 thermoionic emitters, although new microscopes are equipped with cold, thermal or Schottky field emission sources, due to enhanced performance, reliability, and lifetime.

There are several measures of electron gun performance, as reported in Table 5.1: electron emission current, brightness, lifetime, source size, energy spread (the spread in electron energies leaving the filament), and stability (measure of how constant the electron emission is over periods of minutes or hours). However, brightness β is the most important of these, since image quality at high magnification is almost entirely dependent on this parameter. Brightness is the current density per solid angle (A/cm^2 sr) (Eq. 5.3) and is constant along the optical path (neglecting lens aberrations).

$$\beta = \frac{4\, i_b}{\pi^2\, d^2\, \alpha^2} \tag{5.3}$$

where:

- i_b = beam current;
- d = beam diameter;
- α = beam convergence angle.

Table 5.1 - Characteristic parameters of electron sources.

Emitter type	Brightness [A/cm^{2}sr]	Life time [h]	Tip radius	Energy spread ΔE [eV]	Stability	Vacuum [Pa]
Thermionic						
W	106	30-100	30-100 µm	1-3	1%	<10-3
LaB6	107	200-1000	5-50µm	1-2	1%	<10-5
Field emission						
Cold	108	>1000	<5 nm	0.3	5%	10-8
Thermal	108	>1000	<5 nm	1	5%	10-8
Schottky	108	>1000	15-30 nm	0.3-1.0	2%	10-8

5.1.4.2. Electromagnetic lenses

SEM employs electromagnetic lenses to focus electrons. Electromagnetic lenses (Figure 5.8) consist of a cylindrical body of soft iron, containing windings with copper coils. The passage of current in the coils generates an electromagnetic field that interacts with the electrons and controls their trajectory. Two different kinds of electromagnetic lenses assure small spot size:

1) The first lens is the condenser, which control the size of the beam and regulate the level of shrinkage of the source image. Condenser lens focuses the beam at the crossover point.
2) The final lens of the column is the objective lens, that focus the electron beam on the surface of the sample and creates the image of the object with a gaussian probe size (d_g). Gaussian probe size is the ideal final spot at the specimen surface, neglecting aberrations. A method to estimate the Gaussian probe size involves the brightness (β) (Eq. 5.4):

$$d_g = \sqrt{\frac{4\, i_p}{\beta\, \pi^2\, \alpha_2^2}} \tag{5.4}$$

Unfortunately, each lens suffers of all the following aberrations and the Gaussian probe is broadened by the action of lens aberrations of the final lens:

- Aperture diffraction, an error introduced by beam passing through the lens (that behaves as aperture) inside the column, due to the wave nature of electrons;
- Spherical aberration arises because converging lenses are more convergent in the edge than in the centre of the lens. Thus, electrons far away from the optic axis are bent more strongly than those near the axis;
- Chromatic aberration, due to the effect of spread energy of the beam. Electrons from a point of slightly different energies are focused at different locations in the image plane;

- Astigmatism, caused by electrons in sagittal and meridional planes focusing at different distances. Asymmetry in the focusing field originates magnetic inhomogeneities in the pole piece, elliptical pole piece bores, charging effects. Astigmatism can be corrected by stigmator, a device that applies a weak supplement magnetic field to make the lens appear symmetric to the electron beam.

The ideal Gaussian probe (d_p) is broadened by the action of these lens aberrations of the final lens.

5.1.4.3. Deflection system

The deflection system (Figure 5.8) causes the beam to move to a series of discrete locations until a rectangular raster is generated on the specimen. Simultaneously, the same scan generator creates a similar raster on the viewing screen. The operator can determine the scanning speed.

5.1.4.4. Detectors

An appropriate detector must be employed to collect and convert the radiation of interest that leaves the specimen into an electrical signal, then processing to create a SEM image.

Everhart-Thornley detector (ETD) is a scintillator and collects mainly SE and few BSE. Since SE come out of the sample with low energies to be detected, they do not excite the scintillator. Thus, SE must be accelerated up to an energy of a few keV. The detector has a positively polarized grid (10 kV) with respect to the sample at the potential ground, to attract a greater number of electrons. The electrons are accelerated towards the scintillator and radiate it, that emits light. By measuring the electron-induced emission of light, the number of secondary electrons is calculated. The scintillator is placed at about 90 degrees from the normal of the sample (Figure 5.8), mainly for two reasons:

1) Deflects SE that it must collect, discriminating SE and BSE. In fact, BSE escape from the sample at energies such that their trajectory is not significantly inflected by the electric field due to the scintillator, even if some of them are revealed;
2) To observe the morphology and the "shadows" of the sample. Indeed, since the electrons must follow a curved path before reaching the scintillator, should they find a roughness of important dimensions near the exit point, they could hit it and therefore would not be revealed.

Through the lens detector (TTLD) is a solid state ring detector and collects SE, without any BSE. TTLD is installed in GEMINI columns between condenser and the objective lenses. When the sample is very close to the electromagnetic lens, SE that emerge from the sample are attracted by the magnetic field of the objective lens, and by spiralling they re-enter the column until they are focused on the TTLD ring detector. This type of SE collection does not interfere with the primary beam. TTLD provides high resolution images, shadow free images and allows reducing working distance.

Robinson detector is a large scintillator converting the BSE into photons and guides the light signal to a photomultiplier tube. Very large acceptance angle gives high signal levels, enhanced by photo-multiplier. This detector is very effective in producing compositional contrast, while topographical contrast is modest and can be varied by tilting specimen.

Solid state detector (SSD) is a thin wafer placed just below the objective lens (Figure 5.8), allowing a low working distance. Thus SSD enables large acceptance angle, that increases the depth of field. SSD is not sensitive to SE because of an energy filter at about 200-300 eV. BSE interact with the semiconductor detector and produce electron-hole pairs. The production of these charges, inside the bulk of the device, generates an induced charge to the electrodes and therefore a current. From the measurement of this current it is possible to trace the energy and the number of particles that interacted.

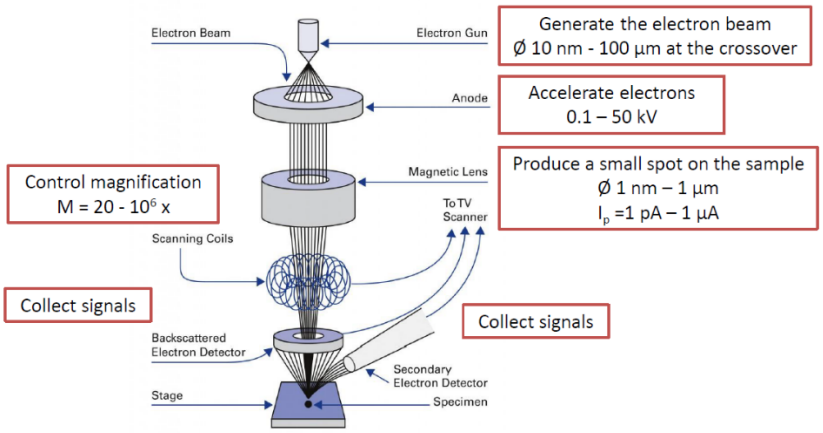

Figure 5.8 – SEM layout and functions.

In the present Ph.D. thesis, Zeiss Supra 40 field emission scanning electron microscope and Tescan Vega 3 scanning electron microscope were used.

5.1.5. Image optimization

Image is produced by the mapping operation which transmits information from the specimen space to the display space. Each point of sample scanned by the beam corresponds to a point of monitor. The sample scanned area (B) and the size of monitor (A) in Figure 5.9A are correlated by the magnification (M), that is controlled only by scan coils (Eq. 5.5):

$$M = \frac{A}{B} \tag{5.5}$$

Specimen and display scans are synchronous and geometric relationships are maintained (Figure 5.9B).

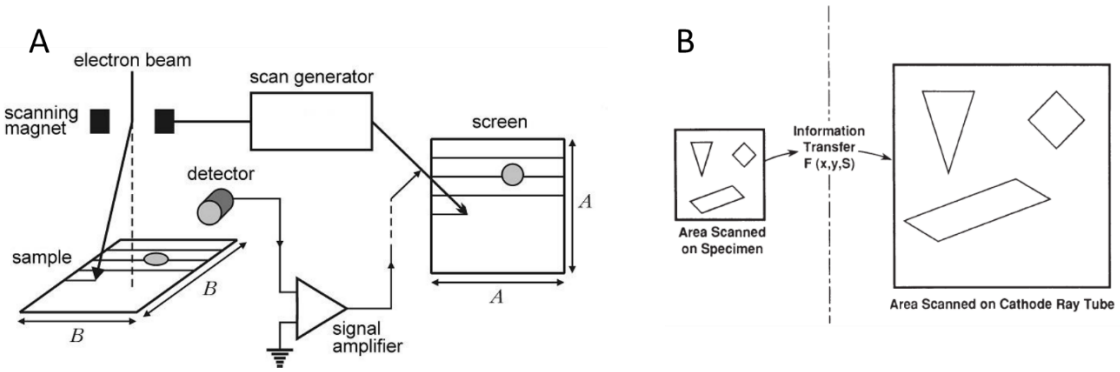

Figure 5.9 - Image is produced by the mapping operation which transmits information from the specimen space to the display space (A), maintaining the geometric relationship (B).

The image consists of a discrete set of dots (pixels). Each Pixel has a physical dimension D (size on the display) given by the size of the display (A in Figure 5.9A) divided by the number of pixels on the same axis N (D = A/N). The size of the display (A) is defined and the first operative step is the definition of the number of pixels (N), which automatically defines their size (D), that in turn should be related to the observer resolution. The grid of dots with the size of the display (D) is shrinked by a factor equal to the magnification (M), and projected on the sample giving rise to a lattice of object pixel with size d = D/M (pixel size on sample). Thus, pixel size on the specimen depends on magnification and determines sharp focus and depth of field (distance within which the object is seen in focus).

Image in sharp focus requires the area sampled on the specimen not larger than the pixel. For the best focus, probe size must be appropriate to magnification (the smaller beam size, the higher magnification).

In SEM the signal to noise ratio (S/N) determines image quality. Noise is due to statistically random fluctuations of signals collected by detectors and electronically amplified. S/N increases with high beam current and low scan rate. In addition, also working distance (WD), i.e. the distance between objective lens and sample plane, affects image quality. Increasing the WD produces a larger spot size d_p at the specimen and a consequent decreasing of the image resolution. Furthermore, WD increasing causes the convergence angle α_2 decreases, giving an improved depth of focus.

5.1.6. Sample preparation

Biological samples preparation for SEM observation usually include fixation, dehydration and drying. Once the sample is fully dried it can be mounted on an SEM stub and then coated with a thin layer of a conductive material (eg. gold). A thin metal film is defined as being between 1 and 10 nm thick. The more popular way of applying thin-metal and carbon films as coating layers on specimens, is the sputtering method. A negatively charged conductive metal target is hit by positive ions in a low-vacuum gas discharge, and the eroded metal

atoms land on the specimen surface. Also polymers and ceramics need to be coated with conductive thin layer, even if low accelerating voltage (< 5 kV) allows to observe sample without charging effects.
If the sample is inherently conductive it will not require coating. When mounting the sample, there must be a continuous electrical connection between the stub and the sample so that the charge does not build up locally. This connection can be achieved using conductive tapes or glues in combination with a conductive coating [1-6].

5.2. Energy dispersive spectroscopy

Energy Dispersive Spectroscopy (EDS) is a semi quantitative X-ray microanalytical technique that provides compositional information for elements from Boron to Uranium (unreliable for light elements).

5.2.1. Generation of X-Ray

As mentioned above, when an electron beam is focused on the sample in a scanning electron microscope (SEM), the electrons from the primary beam penetrate the sample and two types of X-rays result from the interactions: Continuum or background X-rays, and Characteristic X-rays.

5.2.1.1.Continuum X-Ray

Electron beam can undergo deceleration, interacting with the Coulombic field of outer shell electrons of the sample's atoms. The loss in electron energy (ΔE) that occurs due to the deceleration event, is emitted as a photon. The energy of this photon is $\Delta E = h\nu$, where h is the Planck constant and ν is the frequency of the electromagnetic radiation. This radiation is referred as *Bremsstrahlung*. Since the interactions are random, the electron can lose any amount of energy (from zero up to the original energy of the incident electron E_0) in a single deceleration event, forming a continuous electromagnetic spectrum. Continuum X-ray forms the background under the characteristic peaks (Figure 5.10) to be subtracted for reliable quantitative analysis of elements. The intensity of continuous radiation increases with increasing electron probe current, the energy of the incident beam and the average atomic number of the sample. Once the photon is generated with a specific energy, it is impossible to determine whether it is a continuous or characteristic x-ray. Therefore, the intensity of the background due to the continuous radiation, occurring at the same energies as the characteristic X-rays, sets a limit to the minimum identifiable amount of an element. Continuous radiation contains information on the average atomic number of the sample and therefore on the total composition. Consequently, regions of the sample with different average atomic numbers, will emit continuous radiation with different intensity at all energy levels.

5.2.1.2.Characteristic X-Ray

An incident electron can interact with the inner shell electrons of a specimen's atom, by ejecting electron of the inner shells (ionization). The atom becomes energetically unstable, having lost at least E_k, i.e. the binding energy of the K shell electron, and tends to return to the configuration of lowest energy (electrons occupy the orbitals closest to the nucleus). Then, an allowed transition of an outer shell electron fills the inner shell vacancy, relaxing the atom to the state of lowest energy. The energy difference between electron shells is a specific feature of each element. The excess energy is released as a photon. The photon emitted can be absorbed from the atom and eject one electron of the outer shells (Auger electron) or escape the atom as X-ray photon with an energy corresponding to the energy difference of shells involved (Characteristic X-ray, in Figure 5.10).

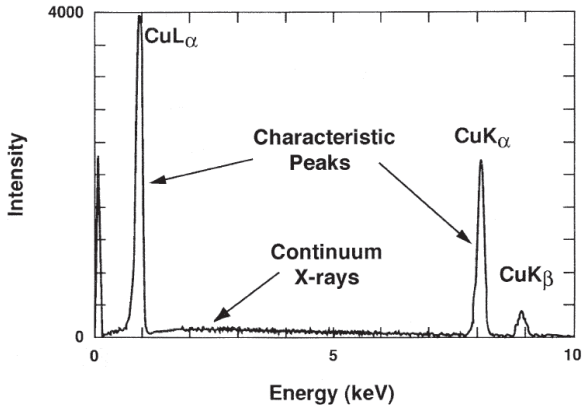

Figure 5.10 - X-ray spectrum of copper (Cu) showing the continuous x-ray spectrum (bremsstrahlung or continuum) and K-series and L-series X-ray peaks.

The two mechanism of Auger electron and characteristic X-ray, schematized in Figure 5.11A, are competitive: for high atomic number Auger electrons emission is favoured, otherwise, for low atomic number, characteristic x-rays emission prevails (Figure 5.11B). EDS works better with high atomic number elements. The highest production efficiency of characteristic X-rays occurs when the energy of incident beam is 2-3 times higher than the energy required for the transition. All elements have at least one transition with $E_0 < 10$ keV.

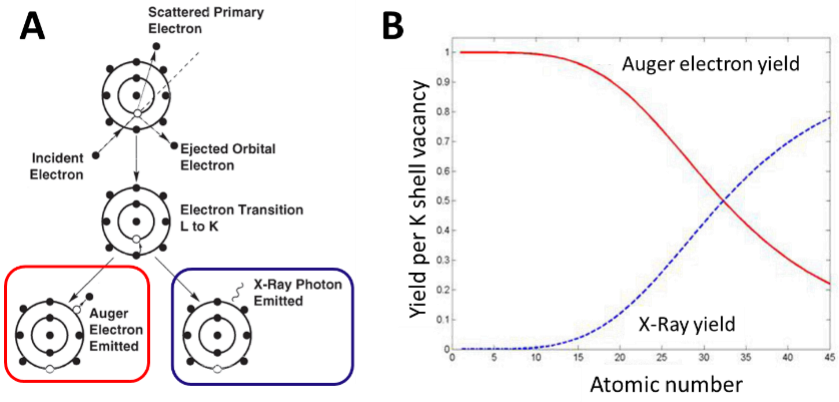

Figure 5.11 – Characteristic X-ray and Auger electron: scheme of emission process (A) and (B) yields as a function of atomic number for K shell vacancies. Auger electron yield - red curve; X-ray yield - dotted blue curve. Similar plots can be obtained for L and M shell transitions.

All the main possible transitions are reported in Figure 5.12A. Because the energy of each shell and subshell is defined, the minimum energy necessary to remove an electron from a specific shell has a defined value as well. This energy is called critical ionization or excitation energy (Figure 5.12 B). Each shell and subshell of an atom requires a different critical ionization energy for electron removal. The K shell has the highest ionisation energy or critical ionisation energy in the atom. The further from the nucleus the electron is, the lower its ionisation energy. X-rays emitted during an electron transition are called characteristic X-rays, due to their specific energies and wavelengths are characteristic of the particular element which is excited. The nomenclature adopted for the emission lines (Siegbahn notation) is as follows:

- K, L, M, N = series into which the de-excited electron falls;
- α, β, γ, δ = level of the most probable transition;
- 1, 2, 3 = sublevel of the most likely transition.

The energies of the electron shells vary in a discrete fashion with atomic number, so that the X-rays emitted in the process have energies characteristic of that atomic number, according to the Mosely Law (Eq. 5.6):

$$E = A(Z - C)^2 \tag{5.6}$$

where E is the energy of the X-ray line, A and C are constants which differ for each X-ray series (C = 1.13 for the K series and approximately 7 for the L series). Thus, Mosely Law may be used to find the energy of any element K or L line, representing the basis for qualitative X-ray analysis, i.e. the identification of elemental constituents.

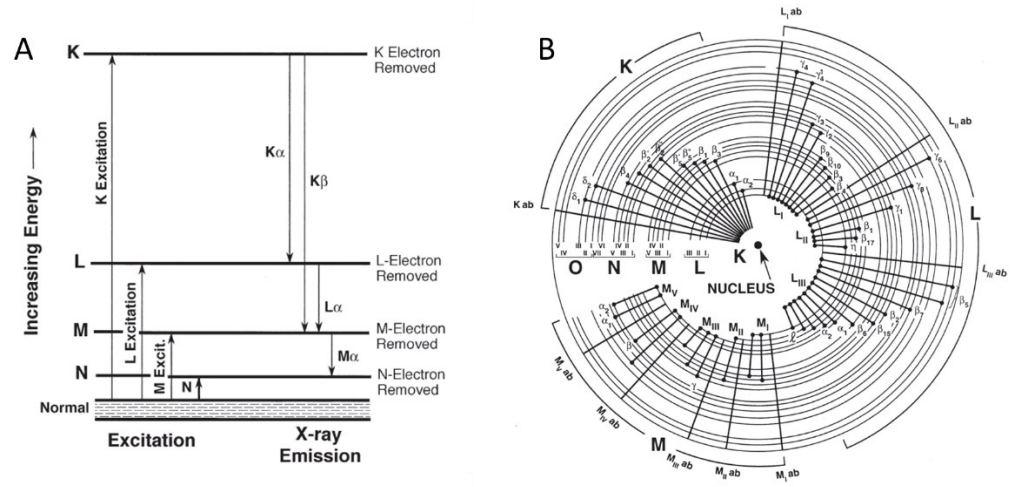

Figure 5.12 – Energy level diagram for an atom: ach horizontal line represents the energy of an electron state. Zero energy represents an atom at rest with no electrons missing (normal) (A) and scheme of nomenclature adopted for the emission lines (B).

5.1.1. EDS analysis

Qualitative microanalysis allows the identification of elements present in the sample from their characteristic X-ray peaks (Figure 5.13A), while in quantitative EDS microanalysis in SEM, the mass fractions or weight percentage of the elements present in the sample are calculated (Figure 5.13B).

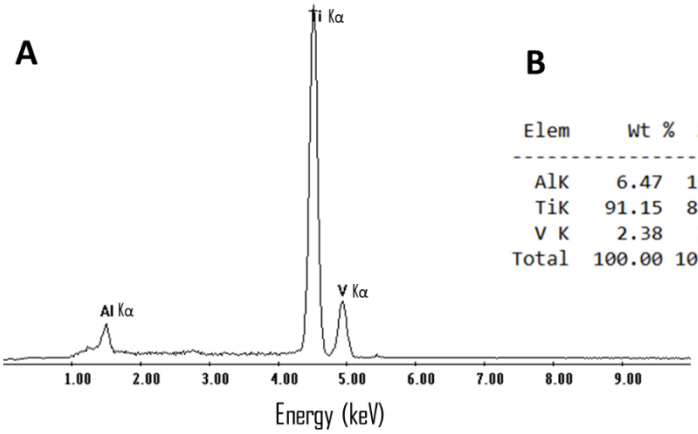

B

Elem	Wt %	At %	K-Ratio	Z	A	F
AlK	6.47	10.96	0.0313	1.0821	0.4451	1.0029
TiK	91.15	86.91	0.9008	0.9941	0.9942	1.0000
V K	2.38	2.13	0.0232	0.9737	1.0024	1.0000
Total	100.00	100.00				

Figure 5.13 - Qualitative (A) and quantitative (B) analysis of Ti6Al4V scaffold surface, from EDAX PHOENIX EDS. Aluminum (Al), Titanium (Ti) and Vanadium (V) elements are detected based on X-ray lines energy (A) and quantified (B).

5.1.1.1. Qualitative Analysis

Qualitative analysis is based on the measurement of the X-ray lines energy and represents the first stage in the analysis of a sample (Figure 5.13A), allowing the rough identification of the elements present, together with a broad classification of their concentration into categories (such as major, minor or trace). In general, the basic steps are as follows: background removal, peak searching (positions and amplitudes), peak recognition (candidate elements for assignment are catalogued from look-up tables) and peak stripping (minor and artifact peaks are stripped to determine if any other elements are present).

5.1.1.2. Quantitative Analysis

Quantative analysis is based by the comparison of the characteristic X-ray intensity emitted by the sample and by a reference standard, collected in the same experimental conditions (Figure 5.13B). At a first approximation the ratio of the emitted intensities (i.e. N_{sample}/N_{std}, where N_{sample} is the X-rays number of sample and N_{std} the X-rays number of standard) is equal to the weight concentration of the analyzed element (C_{sample}/C_{std}) (Eq. 5.7):

$$C_{sample} = \frac{N_{sample}}{N_{std}} C_{std} \quad (5.7)$$

However, to calculate the composition, atomic number (Z), absorption (A) and fluorescence corrections (F), are required, owing the fact that sample and standard have different composition (Eq. 5.8).

$$C_{sample} = \frac{N_{sample}}{N_{std}} Z\ A\ F\ C_{std} = K_{ratio}\, Z\ A\ F\ C_{std} \quad (5.8)$$

Difference in atomic number (Z) are related to:

1) Different backscattering and thus different energy penetrating the sample;
2) Different depth distribution of generated X-rays and thus different paths for escaping the surface.

The absorption of X-Rays (A) depends on the chemical composition, which is different from sample to standard. Consequently, secondary fluorescence (F) is different from sample to standard [1-6].

Bruker Z200 energy dispersive microanalysis and EDAX Elements EDS system were employed in this doctoral research project.

5.1. X-Ray Diffraction

X-Ray diffraction (XRD) uses X-Rays to investigate and quantify the crystalline nature of materials by measuring the diffraction of X-Rays from the planes of atoms within the material.

5.1.1. Geometry of crystal

The structure of all crystals can be described by a lattice, with a group of atoms allocated to every lattice point. Any point indicates identical surroundings as any other point in the lattice. Thus, the lattice point can be reproduced by repeating a small unit, referred as unit cell. All unit cell sequences can be given by three lengths *a*, *b*, and *c* and the interaxial angles between them (α, β, and γ), representing the lattice parameters of the unit cell. The relationship between *a*, *b*, and *c* and α, β, and γ is illustrated in Figure 5.14A.

By putting lattice points at the corner of these crystal systems for finding a certain minimum set of symmetry elements, seven kinds of crystal systems are obtained. Nevertheless, there are other ways for fulfilling the condition that each point has identical surroundings, forming 14 possible point lattices and no more (Bravais lattices) as shown in Figure 5.14B.

In order to indicate a lattice plane, Miller indices are usually employed. Miller indices (h k l) are defined as the reciprocals of the fractional intercepts which the plane makes with the crystallographic axes (x, y, z). The planes of a family {h k l} are parallel to each other and equidistant The value of the interplanar spacing (d_{hkl}) is a function of both the plane indices and the lattice parameters.

Solids that do not contain order (e.g. glass) are referred to as amorphous. Many polymers are a mixture of crystalline and amorphous phases.

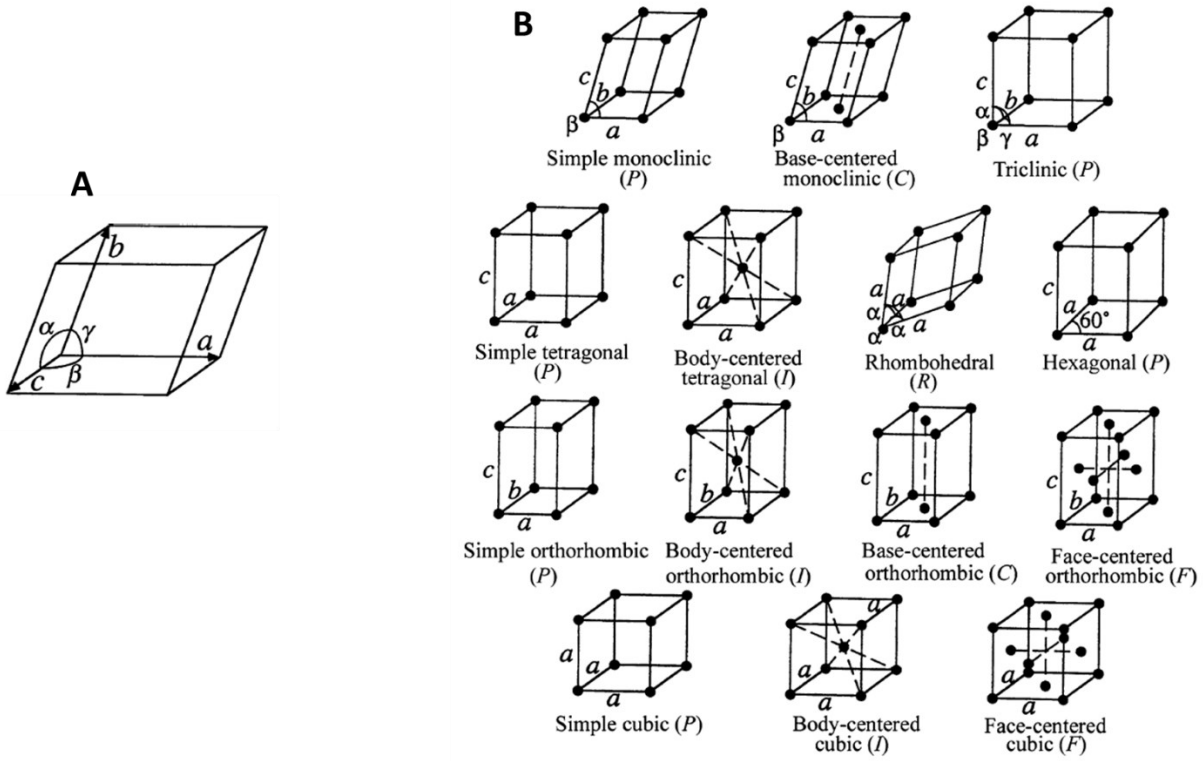

Figure 5.14 – Geometry of crystal: (A) Relationship of lattice parameters of unit cell (lengths: a, b, c and interaxial angles between them: α, β, γ); (B) Bravais lattices.

5.1.2. Diffraction from crystal

The diffraction phenomena of X-rays by crystals is attributed to the phase relations between two or more waves, such as differences in phase produced from the differences in path length of waves and a change in amplitude related to the phase difference. The phase of any two waves generally shows deviation of Δ, corresponding to their path difference, which depends on direction of X-ray with respect to the crystal. Since the phase of two waves is completely coincident (in phase) if the value of Δ is given by an integer multiple of wavelength λ, two waves will combine to form one synthesized wave just like the original one, and its amplitude will be double. This phenomenon of constructive interference (Figure 5.15A) is the basis of the diffraction theory. When the value of Δ is λ/2, the two waves cancel each other and they are completely out of phase (destructive interference, in Figure 5.15B), resulting from the fact that the waves have the same magnitude but opposite amplitude at any point along its path.

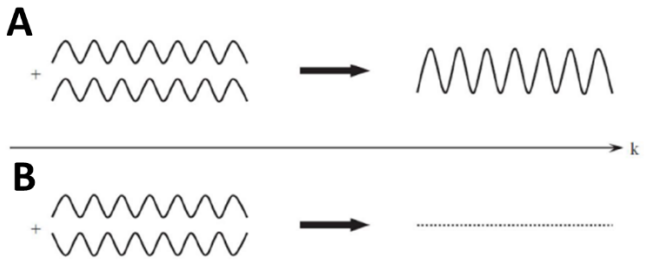

Figure 5.15 - Phenomenon of constructive (A) and destructive (B) interference.

Therefore, only the elastic interactions conserving energy, contribute to the diffracted signal used in XRD. However, the interaction of the X-ray beam with the specimen originates many other signals from inelastic scattering, such as fluorescence and Compton scattering, which contribute to the background of diffraction measurements.

The main target of X-ray diffraction by crystals is to know the particular condition in which the scattered X-rays from atoms and the incident X-rays are completely in phase and reinforce each other to produce a detectable diffraction beam. In other words, the common relationship that the differences in path length between X-rays scattered from crystals and that of the incident X-rays is an integer multiple of wavelength λ. For this purpose, the most familiar method is given by Bragg's law. If the incident X-rays of wavelength λ (1.54 Å in the case of a copper tube source) strike a crystal where all atoms are placed in a regular periodic array with interplanar spacing d_{hkl}, diffraction beam of sufficient intensity is detected only when the Bragg law (Eq. 5.9) is satisfied (Figure 5.16):

$$2\, d_{hkl}\, \sin\theta = n\, \lambda \tag{5.9}$$

Where:

- n is the order of reflection. It is equal to the number of wavelengths in the path difference between diffracted X-rays from adjacent crystal planes;

- θ is the incidence angle of parallel and monochromatic X-Rays beam, on the family planes hkl, whose spacing is d_{hkl}.

It is clear from Bragg law that lab-based instruments are usually monochromated to guarantee a single wavelength.

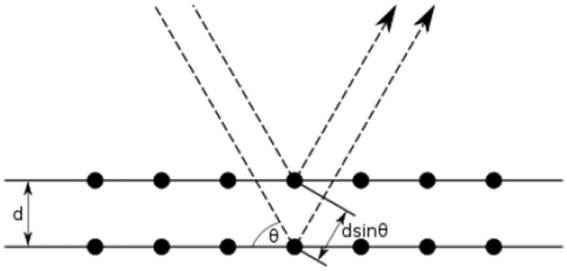

Figure 5.16 – Schematic of interaction of incident beam with lattice planes placed at distance d, in according to Bragg law.

5.1.3. X-ray diffractometer

The most common method for measuring the intensity of a scattered X-ray beam from crystalline materials is to measure the X-ray diffraction intensity from a sample as a function of diffraction angle, by using a diffractometer. Most diffractometers are based on the Bragg-Brentano geometry (Figure 5.17), where the X-ray source and detector are on the same side of the sample. There are several different types of instrument design. In the θ–2θ geometry, the X-ray source is fixed, while the sample holder moves around θ and the detector moves around 2θ. In the θ–θ geometry the sample position is fixed while the X-ray source and the detector both move around θ. The essential characteristic of both geometries is the relationship between θ (the angle between the incident X-ray beam and the sample surface) and 2θ (the angle between the incident X-ray beam and the receiving slit-detector) maintained throughout the analysis. The distance between the X-ray source and the sample, and between the sample and the detector, is fixed and equal.

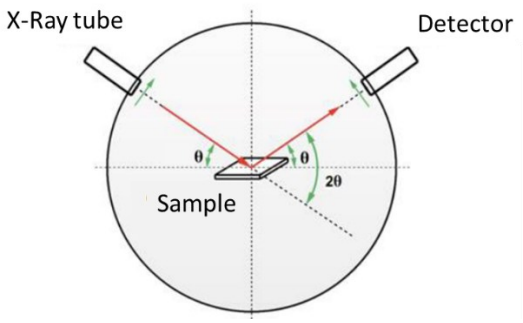

Figure 5.17 - Bragg-Brentano diffractometer geometry.

The source is an X-ray tube. It consists of an evacuated ceramic or glass vessel that contains a tungsten filament as the cathode which emits electrons, and an anode (common in Copper) onto which these electrons are accelerated with a potential of several tens of thousands of volts. In most instruments a monochromator is put before the detector (only wavelengths meet the Bragg condition are directed to the detector). The scintillator detector emits photons when irradiated with X-rays. A photomultiplier detects the light and emits a pulse, enabling an accurate measurement of intensities and positions. In the generated signal, the most intense characteristic lines are the Kα1 and Kα2 radiation and the Kβ. The first two are usually used in diffraction experiments. All other types of radiation (including the Bremsstrahlung) are unwanted by-products.
For X-ray diffraction measurements of this thesis are carried out by using a Bruker D8 Advance diffractometer, operating at V = 40 kV and I =40 mA, with Cu-Kα radiation.

5.1.4. Diffraction measurements

The XRD data are typically plotted as a diffractogram with the X-ray intensity in function of 2θ angle (Figure 5.18). Each phase produces a unique and distinctive diffraction pattern, as illustrated in the pattern in Figure 5.18.

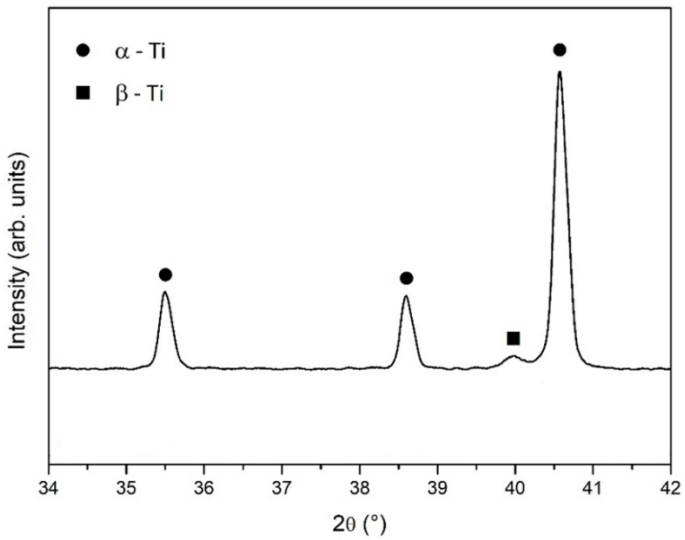

Figure 5.18 – XRD pattern of Ti6Al4V scaffold from Bruker D8 Advance diffractometer. α-Ti and β-Ti phases peaks are identified.

5.1.4.1. Phase identification

Phase identification is a qualitative process based on the analysis of the XRD spectrum (position of peaks and eventually their intensity in Figure 5.18) for identifying the phases present in the specimen. Also a presence of amorphous phase is detectable. Phase identification occurs by matching peak positions with a known library of spectra. The most common sources of diffraction spectra is the database made by the International Centre

for Diffraction Data (ICDD, https://www.icdd.com/). Diffraction data is provided as a Powder diffractions file, PDF, with a unique identifier. Alternatively to commercially purchased databases, online open access databases are growing. The main open access website for crystallographic and XRD data is the Crystallography Open database (COD, http://www.crystallography.net/cod/). In many cases, very newly additively manufactured biomaterials will not yet appear in these databases, thus the best place to find their spectra is in the literature publication.

5.1.4.2. Quantitative analysis

Quantitative analysis refers to the use of the XRD spectrum to extract quantitative data. Position and intensity of diffraction peaks in an X-ray diffraction pattern are due to the crystal structure. Specifically, positions of the diffraction peaks is determined by the interatomic distances; while the intensity of the diffraction peak are influenced by the types of atoms and their positions. Widths and shapes of the diffraction peaks are mainly a function of the instrument and microstructural parameters.

Additionally, Rietveld refinement is a technique allowing the quantification of crystalline phases from diffraction spectra. The Rietveld method uses a least squares approach to refine a theoretical line profile until it matches the measured profile. It includes an approximation of peak shape, peak width, preferred orientation and peak intensity [6, 7].

Qualitative and quantitative information from XRD can be useful indications for biological performances of scaffold or coating. Results from Hu et al. [8] study provide evidence of the effects of calcium phosphate crystallinity on promoting cell attachment efficiency, proliferation, and differentiation of BMSCs. Also Cui et al. [9] observed that highly crystalline and rigid PCL and PGA surfaces are significantly more efficient in supporting NIH-3T3 fibroblast growth, respect to amorphous/flexible PCL/PGA. Thus, crystallinity represents a fundamental characteristic of scaffold surface or coating, in order to improve the biological events beyond the interaction with the biological environment.

5.1.5. Sample preparation

The main requirement for the correct execution of a XRD measurement, is the flatness of the sample. Since scaffold is inhomogeneous sample, scaffold porous surface is aligned so that the incident beam is directed along the path with the higher number of connected struts. In the case of additive manufacturing powder, the powder is levelled and pressed into a sample holder with a hallow, until a flat surface is obtained.

5.1. X-ray micro Computed Tomography

X-ray micro Computed Tomography (XμCT) allows 3D investigation of small radiopaque objects, with a high resolution of few micrometers, in a non-invasive and non-destructive way. Laboratory- or desktop-based XμCT systems typically operate with a X-ray cone geometry, using the raw spectrum from the X-ray source, while most synchrotron-based XμCT measurements are performed using monochromatic X-ray beam in a parallel beam geometry [10].

5.1.1. Image formation

The principle on which relies the image formation in conventional imaging is the differences in X-ray absorption of the sample details. However, absorption contrast is not well suited for the characterization of biomaterials composed of constituents with low absorption and only small difference in atomic number, such as polymers and nonmineralized biological materials. If structures with a weak absorption or with similar absorption properties are observed, the overall image contrast may be insufficient to obtain a meaningful image. Notwithstanding, phase-contrast effect becomes an essential modality to obtain sufficient image contrast for soft biological tissues and biological samples, where conventional absorption radiography fails.

5.1.1.1. Absorption contrast

In the present Ph.D. work, absorption-contrast XμCT is based on the mapping of the linear attenuation coefficient of X-ray crossing the investigated sample. The attenuation depends upon the composition and density of the object. The absorption of a monoenergetic incident X-ray beam in a homogeneous material can be described by the Beer-Lambert's law (Eq. 5.10) [11]:

$$I = I_0 \, e^{-\mu \Delta x} \tag{5.10}$$

where:

- I = intensity of the beam after running through the matter;
- I_0 = incident intensity;
- μ = linear attenuation coefficient, given by a linear combination of the photoelectric, Compton, and coherent scattering effect;
- Δx = thickness of the material.

Absorption-contrast XμCT analysis are performed by a Bruker Skyscan 1174 system. The X-ray source operates at accelerating voltage 20-50 kV, current 0-800 μA and exposure time 1.5-10 ms. The X-ray CCD-camera is based on a 1.3 Megapixel (1304x1024 pixels) CCD-sensor, connected to PC. This camera acquires images from a scintillator screen using a high-resolution motorized macro lens which allows variable magnification of the system (pixel size of 6 μm). An object manipulator can move the object up and down and rotate the object to acquire angular shadow projections for tomographic reconstruction.

5.1.1.2. *Phase Contrast*

Phase-contrast XμCT is based on phase variation of the X-ray electromagnetic wave after interaction with the sample. For X-ray the refractive index (n) of the material is a complex number (Eq. 5.11):

$$n = 1 - \delta + i\beta \tag{5.11}$$

Where δ is the decrement of the real part of the complex refractive index n, related to the phase shifts of the electromagnetic wave in the matter and, therefore, its deviation from the incident direction. Whereas, the imaginary part β is the extinction coefficient, which describes the material absorption, due to the photoelectric effect and scattering. For common tissues and cells used in biological experiments, δ is about three order of magnitude higher than β, thus resulting in higher sensitivity of the phase-contrast approach respect to absorption contrast. Consequently, the phase shift effects can be much larger than the absorption effects, on which conventional techniques are based. Therefore, thanks to the phase shifts contributions, the sensitivity of the imaging system can be greatly enhanced, particularly when the contrast rising from the differences in absorption are not sufficient to distinguish tiny details from the background [10, 12].

Since phase-contrast imaging requires a homogeneous X-ray beam with spatial coherence, synchrotron radiation is particularly well suited for this technique [12]. Phase-contrast XμCT measurements of this thesis are carried out at the SYRMEP beamline of the ELETTRA Synchrotron Radiation facility (Trieste, Italy), using white X-ray beam with 19 keV peak energy, sample-to-detector distance of 10 cm and pixel size of 0.9 μm.

5.1.2. From Projections to the 3D Analysis

Starting from the totality of 2D projections (radiographic images), 3D tomographic slices (i.e., images of the internal structure of the sample in a plane parallel to the beam propagation direction) are reconstructed. The reconstructed images are then digitally analyzed to extrapolate quantitative data and to support the qualitative visual interpretation, by following a precise workflow (Figure 5.19) [10]. Workflow treated in this paragraph refers to typical benchtop microtomographic system.

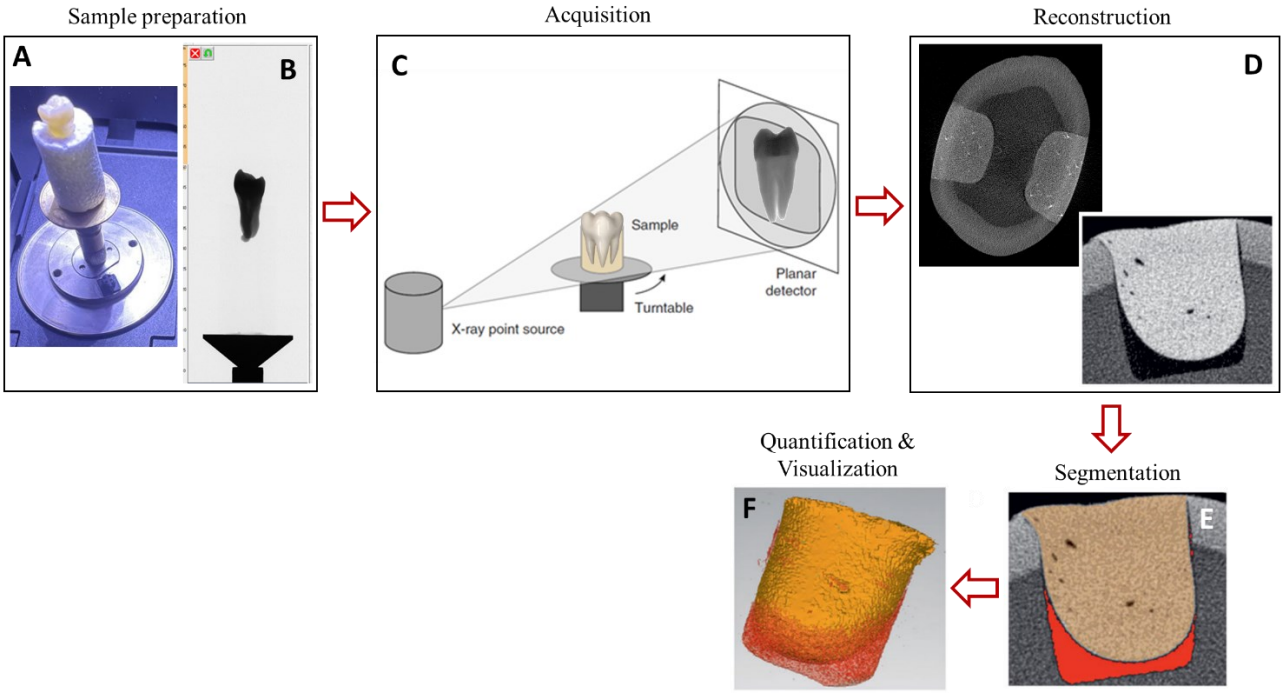

Figure 5.19 - XμCT workflow for gap detection in tooth restoration: Sample preparation articulated in sample mounting (A) and scanning parameters optimization (B); Acquisition (C); Reconstruction (D); Segmentation (E); Quantification and 3D visualization (F). Modified from [10, 13].

5.1.2.1. Sample preparation

Sample is mounted in the rotation center of sample holder, using radio-transparent fixing materials such as polystyrene foam or wax, to avoid misalignment artifacts and to allow for maximum zooming (Figure 5.19A). Then, the region of interest (ROI) is positioned in the camera field of view (FOV), pixel size is set and the energy transmission through the sample is optimized by configuring the correct filter and adjusting voltage, current and exposure time (Figure 5.19B). By using metal filter (Aluminum or Copper) placed in the beam path between the x-ray source and camera, it is possible to change the shape of the spectrum towards higher energy peaks.

5.1.2.2. Acquisition

X-rays beam, after passing through the sample, is collected by detector. A series of bi-dimensional projections (shadow images) are taken, usually at a fixed angular increment (Figure 5.19C). Total rotational angle is typically 360°, when a cone-beam geometry is used. For preclinical and industrial applications, very often source and detector are fixed and the sample is placed on a rotating stage.

5.1.2.3. Reconstruction

The obtained shadow angular projections will be used for the reconstruction of the virtual slices through the object. A raw data cross section is generated using a reconstruction algorithm (Figure 5.19D). This raw data is not yet an image, it is a floating point matrix holding the absorption values in the reconstructed cross section

(size NxN, where N is the number of pixels in the lines of the angular projection images). The reconstruction results can be saved, by selecting minimum and maximum values of the density window. All values between these will be displayed as half tone image of the cross section with linear conversion to 256-grades of gray inside the selected density interval. In addition, image quality can be improved, mainly in terms of artifacts compensation and noise reduction.

5.1.2.4. Segmentation

Segmentation roughly implies a classification of the voxels aimed at identifying the interesting objects within the reconstructed volume and labels each of them with a single value. Segmentation involves reading the grayscale volume and producing an image having as many labels as the number of identified objects or phases (Figure 5.19E).

5.1.2.5. Quantification and Visualization

XμCT is a technique that enables a good visualization of the structure of mineralized bone and of biomaterials (Figure 5.19F). Furthermore, for quantitatively describing bone architecture and bone-inspired structures, a few families of features are commonly identified:

- A set of basic morphometric indices such as relative density (or porosity) and surface density is used to characterize the sample;
- Thickness measurements (struts and pores) are useful indications, since the regenerated tissue is composed of small structural elements. For example in bone tissue engineering, the quantification of the size of the trabeculae is of great interest as it directly correlates with the biomechanical properties of the regenerated tissue;
- Another parameter often used to understand the biomechanical properties of the regenerated tissue is the geometric degree of anisotropy. It is constituted under the influence of strengths applied to the tissue and permits to establish the resistance to these strengths in a given preferential direction;
- When the regenerated tissue features an interconnected pore space, one of the goals of the analysis might be the quantification of the degree of connectivity. The connectivity density does not carry information about positions or size of connections, but it is a simple global measure of connectivity, which gives higher values for better-connected structures and lower values for poorly connected structures.

5.2. Mechanical tests

Tensile, flexion and compression tests are the fundamental types of mechanical testing. Compression tests are used to determine material behavior under an increasing axial compressive load to a test specimen, usually of either cuboid or cylindrical shape. The load is applied using specialized fixtures on an universal testing machine. The test method determines important mechanical properties such as yield strength, yield point,

Young Modulus, stress-strain curve and compressive strength. In the case of a material that does not fail in compression by a shattering fracture, compressive strength is a value that is dependent on total strain and geometry. Testing in (uniaxial) compression is sometimes an attractive alternative to tensile testing. Specimens can be simpler in shape and smaller, since there is no gripping requirement. For bone scaffold, whose integrity under compressive forces is critical, compression testing is often used. The key question is whether corresponding information from compression and tensile tests can be obtained. In the majority of cases, the underlying plasticity response is symmetrical. However, there are important aspects to consider:

1) Scaffold macro-structure (preferential direction and tortuosity of porous network, connectivity, etc.) adds a level of complexity to dependence of biomaterial response on stress;
2) In some biomaterials, a phase transformation occurs during loading, then asymmetry is possible;
3) The friction between sample and plates effects the results;
4) Buckling or shearing specimens instability is possible as obviously the necking is absent.

5.2.1. Compressive test

Compressive strength is calculated by dividing the maximum load for the original cross-sectional area of a specimen in a compression test. It is the maximum stress a material can sustain under crush loading. When brittle materials reach their ultimate compressive strength they are crushed, and the load drops drastically (Figure 5.20A). However, the compressive strength of materials that do not shatter in compression must be defined as the amount of stress required to distort the material an arbitrary amount. Materials with higher ductility do not rupture, but instead continue deforming until the load is no longer being applied to the specimen, but rather between the two compression platens (Figure 5.20B). In these cases, compressive strength can be reported as specific deformation (%) of the tested specimen original height. A semi-ductile material shows an intermediate behavior (Figure 5.20C)

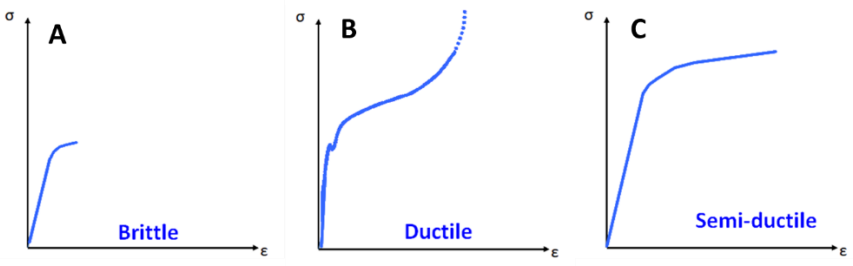

Figure 5.20 - Different compression behavior of brittle (A), ductile (B) and semi-ductile (C) materials.

Before the compression testing, sample requirements concern width and thickness (or diameter) and the average cross-sectional area of the specimen section. Long samples are prone to buckling therefore the length of the specimen must be limited. The specimen length must not exceed 10 times it diameter to avoid buckling. On the other hand small samples results in inaccuracies in results, while using large samples requires testing machines with large capacities. Both ends of the specimen must be flat and parallel. The specimen must be

placed in the test fixture and centered in the middle. Eccentricity may cause instability. Friction between the machine head and the sample effects the results causing stresses to have a small inclination (Figure 5.21). Because the size of the specimen may be small compared to the size of the testing machine head, bearing blocks are used between the specimens and the machine head to ensure proper distribution of the load.

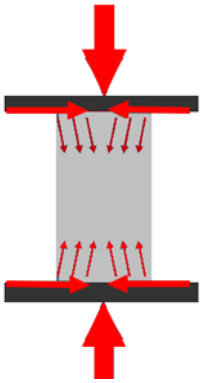

Figure 5.21 - Stresses direction inclined respect the applied load due to the friction effect.

An Instron 5567 machine equipped with 30 kN max load cell and extensometer Instron 2630, gauge length 25 mm, was used for compressive tests.

5.2.2. Incompressible materials

The engineering stress, or conventional stress, in conventional mechanical testing of materials is calculated from the force divided by the sample original area, A_0. Because of the constancy of volume in incompressible solids, $A_0 l_0 = A_s l_s$ (where l_0 is the original length of the specimen, A_0 is the original cross-sectional area, A_s is the instantaneous cross-sectional area of the sample and l_s is the instantaneous length of the sample). Expressions for the true strain (ε_t) can therefore be written in terms of either the length or the area of the test sample. Accordingly, the true stress (σ_t) is calculated from the signal measured of the transmitted force divided by the instantaneous cross-sectional area, A_s, of the specimen over which it acts (Eq. 5.12):

$$\sigma_t = \frac{A_0 E \varepsilon_t}{A_s} \tag{5.12}$$

Without the assumption of incompressible (i.e., there is a fixed relationship between sample cross-sectional area and its length) there is no basis for using the transmitted signal to measure force. Materials for which this problem exists include metallic and polymeric foams, honeycomb structures, and porous compacts for which mechanical loading produces compaction, densification, or porosity during testing [14]. These samples not possessing constant volumes by their very nature of compacting or exhibiting nonhomogeneous deformation processes prior to achieving a “bulk” response during testing, will exhibit significant time delays before the sample attains a uniform state of uniaxial stress-state equilibrium (if at all) during testing.

5.2.2.1. Porous and cellular metal specimen

Porous and cellular metals have attractive properties due to their unique cell morphology. The deformation behavior of porous metals and metallic foams is quite different from conventional bulk metals, and the test methods for conventional metal materials are not suitable for porous metals and metallic foams. Standardization of a test method for porous metals and metallic foams is required.

Standard ISO 13314:2011 [15] defines a test method to evaluate the compressive properties of porous and cellular metals with a porosity of 50% or more. Compressive stress is defined as the compressive force divided by the initial cross-sectional area perpendicular to the loading direction, and compressive strain, the compressive displacement divided by the initial height of the specimen. Other relevant mechanical properties are reported in Table 5.2.

Table 5.2 – Mechanical parameters from stress-strain curve of porous and cellular metals.

Mechanical parameter	**Description**
First maximum compressive strength	Compressive stress corresponding to the first local maximum in the stress-strain curve (arrow 3 in Figure 5.22). It cannot be determined if no local maximum occurs.
Plateau stress (σ_{pl})	Arithmetical mean of the stresses at 0.1% or smaller strain intervals between 20% and 30% or 20% and 40% compressive strain. The strain range 20% and 30% or 20% and 40% varies depending on the plateau end strain (σ_{pl} in Figure 5.22).
Plateau end (e_{ple})	Point in the stress-strain curve at which the stress is 1.3 times the plateau stress (e_{ple} in Figure 5.22). If this point does not adequately represent the end of the plateau range, another stress can be selected which corresponds to the curve trace.
Quasi-elastic gradient	Gradient of the straight line determined within the linear deformation region, at the beginning of the compressive stress-strain curve. This gradient is not a modulus for the material. The quasi-elastic gradient is optionally measured and it is used to determine the zero point for the compressive strain (arrow 1 in Figure 5.22 and 5.23).
Compressive offset stress	Compressive stress at the plastic compressive strain of 0.2%, unless otherwise specified or recorded (arrow 2 in Figure 5.23). The plastic strain is determined using of the quasi-elastic gradient. The compressive 0.2% offset stress is optionally measured and it can be used as an alternative to the compressive yield strength.
Elastic gradient	Gradient of the elastic straight lines determined by elastic loading and unloading between stresses σ_{70} and σ_{20} that correspond to 70% and 20% of the plateau stress, respectively (arrow 2 in Figure 5.22 and arrow 1 in 5.24). The elastic straight line is the secant line obtained from the hysteresis loop which occurs during unloading and subsequent loading. The elastic gradient represents a porosity-dependent rigidity, not a modulus of the material, and generally changes during the course of compression. The elastic gradient is optionally measured and it is used to determine the zero point for the compressive strain.

Compressive proof strength	Compressive stress at a plastic compressive strain of 1.0%, unless otherwise specified or recorded (arrow 2 in Figure 5.24). Plastic strain is determined using of the elastic gradient. The compressive proof strength is optionally measured and it can be used as an alternative to the compressive yield strength.

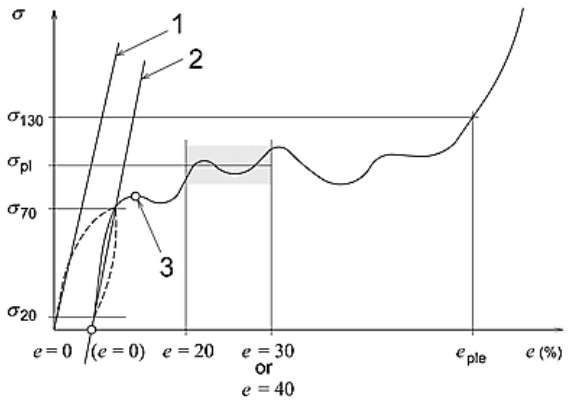

Figure 5.22 - Stress-strain curve to determine the characteristic values from compression testing of porous and cellular metals: 1) quasi-elastic gradient; 2) elastic gradient; 3) first maximum compressive strength.

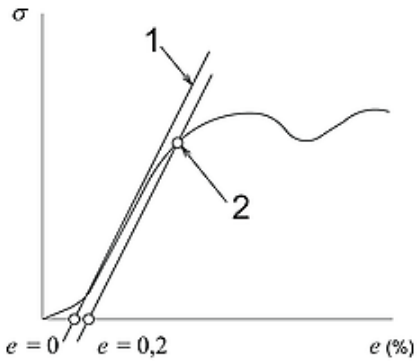

Figure 5.23 - Stress-strain curve to determine the optional characteristic values from compression testing of porous and cellular metals: 1) quasi-elastic gradient; 2) compressive offset stress.

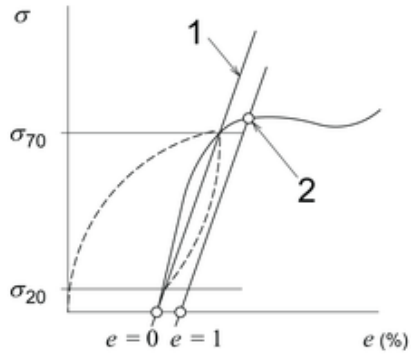

Figure 5.24 - Stress-strain curve to determine the optional characteristic values from compression testing of porous and cellular metals: 1) elastic gradient; 2) compressive proof strength.

5.2.2.2. Rigid Cellular Plastics

Test method proposed by [16] provides information regarding the behavior of plastic cellular materials under compressive loads. Deformation data can be obtained, and from a complete load-deformation curve it is possible to compute the compressive stress at any load (such as compressive stress at proportional limit load or compressive strength at maximum load) and to compute the effective modulus of elasticity.

5.1.1.1. Advanced ceramics

Compression testing of ceramics is concerned with the cumulative failure processes leading to failure in uniaxial compression. Test methods [17] reveal such properties as strength, fracture resistance, and slow crack growth, which contribute to design, scientific understanding and estimations of service life of ceramic implant [18].

5.2. Roughness measurements

Scaffold surface shows structure and properties depending on biomaterial nature and manufacturing process. Surface roughness influence *in vitro* and *in vivo* cellular morphology, proliferation and phenotype expression, and modulates the biological response of tissues in contact with the implant [19].

Surface roughness most commonly refers to the variations in the height of the surface relative to a reference plane. It is measured either along a single line profile or along a set of parallel line profiles (surface maps). It is usually characterized by statistical height descriptors advocated by the American National Standards Institute (ANSI) and the International Standardization Organization (ISO).

Depending on the scale of irregularities of the material surface, surface roughness can be divided to macro-roughness (100 μm - millimeters), micro-roughness (100 nm - 100 μm), and nano-roughness (less than 100 nm), each with its specific influence on cell response, also depending on cell type [19].

In this thesis the roughness was measured in accordance with DIN EN ISO 4287/4288 and DIN EN ISO 25178. A Nikon LV 150 Confovis Microscope was used to assess surface topography with:

- Microscopic objective of 20x;
- Lateral resolution of 0.595 μm, vertical quantization of 10 nm and automatic field stitching;
- Scanned area of 0.5 x 1.5 mm^2.

The following roughness parameters were measured:

- Sa (arithmetical mean height) is the extension of Ra (arithmetical mean height of a line) to a surface (A). It expresses, as an absolute value, the difference in height (Z) of each point compared to the arithmetical mean of the surface (Eq. 5.13):

$$Sa = \frac{1}{A}\iint_A |Z(x,y)|dxdy \tag{5.13}$$

This parameter is generally used to evaluate surface roughness.

- Sz (Maximum height) is defined as the sum of the largest peak height value and the largest valley depth value within the definition area.

- Sq (Root mean square height) represents the root mean square value of ordinate values within the definition area (A). It is equivalent to the standard deviation of heights (Z) (Eq. 5.14):

$$\mathrm{Sq} = \sqrt{\frac{1}{\mathrm{A}} \iint_{\mathrm{A}} \mathrm{Z}^2(\mathrm{x},\mathrm{y})\mathrm{dxdy}} \tag{5.14}$$

- Ssk (skewness) values represent the degree of bias of the roughness shape (asperity). A useful parameter in defining variables with an asymmetric spread, it represents the degree of symmetry of the distribution function. It is usual normalized for Sq^3 (Eq. 5.15):

$$Ssk = \frac{1}{Sq^3}\left[\iint_A Z^3(x,y)dxdy\right] \tag{5.15}$$

As illustrated in Figure 5.25A:

· For Ssk < 0, the height distribution is biased above the mean plane;
· For Ssk = 0, the height distribution (peaks and valleys) is symmetrical against the mean plane;
· For Ssk > 0, the height distribution is biased below the mean plane.

- Sku (kurtosis) value is a measure of the sharpness of the roughness profile. It represents the peakedness of the distribution and is a measure of the degree of pointedness or bluntness of a distribution function. Again, it is usual normalized for Sq^4 (Eq. 5.16):

$$Sku = \frac{1}{Sq^4}\left[\iint_A Z^4(x,y)dxdy\right] \tag{5.16}$$

As illustrated in Figure 5.25B:

· For Sku < 3, the height distribution is biased above the mean plane;
· For Sku = 3, the height distribution is a normal distribution (sharp portions and indented portions co-exist);
· For Sku > 3, the height distribution is spiked.

A Gaussian distribution of surface roughness (black line in Figure 5.25A and B) has Ssk = 0 and Sku = 3, showing an equal number of local maxima and minima at a certain height above and below the mean line.

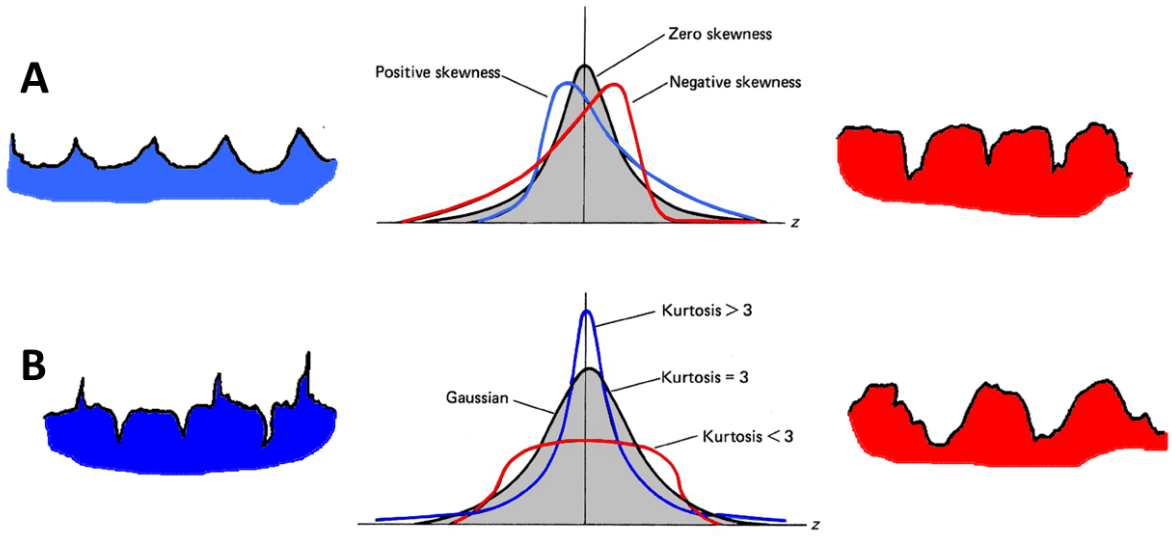

Figure 5.25 – Gaussian distribution (black line in A and B with Ssk = 0 and Sku > 3, respectively) of surface roughness is compared with skewness (A) and kurtosis (B) values. A surface with Ssk < 0 (red line and surface in A) has a larger number of local maxima above the mean as compared to a Gaussian distribution; for Ssk > 0 the converse is true (blue line and surface in A). Similarly, a surface with a Sku < 3 (red line and surface in B) has a larger number of local maxima above the mean as compared to that of a Gaussian distribution; again, for a Sku > 3 the converse is true (blue line and surface in B) [20].

5.3. Biological tests

5.3.1. Cell culture

MG-63 human osteosarcoma cells, human Mesenchymal Stem Cells (hMSCs) derived from bone marrow and Murine fibroblast cell line (NIH-3T3) are employed for biological tests of this thesis.

HMSCs can be found in various tissues of adult organism. These cells display a multilineage potential and can be *in vitro* differentiated into the osteogenic, chondrogenic and adipogenic lineage. This ability makes hMSCs promising candidates for tissue engineering strategies [21]. Upon treatment in culture, hMSCs commence the transition to the osteoblast lineage, upregulating typical osteogenic markers and depositing a mineralized matrix.

Osteosarcoma is the most common malignant bone tumor, which frequently arises within the metaphyseal growth plates, where hMSCs concentrate, proliferate and differentiate. In particular, osteogenic osteosarcoma is composed of immature bone progenitors that produce abundant, amorphous osteoid lacking the characteristics of mature bone. The MG63 cell line was derived from human bone osteosarcoma [22].

In this thesis, hMSCs are used to test how the combination of biomaterial, additive manufacturing technology and 3D design enable the differentiation process, in other words if scaffold shows osteogenic potential. MG63 are employed for short-term biological tests, targeting to adhesion and proliferation.

HMSC and MG63 cells expanded in polystyrene (T75 flasks) and monitored for their morphological appearance by Docheva et al. [22], experimentally show specific features. HMSC culture contains both, rapidly self-renewing (RS) cells with spindle shape (arrows in Figure 5.26A) and slowly replicating (mature hMSCs) flattened cells (FC) (arrow heads in Figure 5.26A), while attached MG63 cells revealed an oval to spindle-shaped appearance (Figure 5.26B). In addition, there are clear differences in the population doubling time (average of three passages), as reported in Figure 5.26C: MG63 cells proliferate at a faster rate than hMSCs (mixture of RS and FC cells). Calculation on cell area and volume determine that MG63 cells are the smallest in area, followed by RS cells. The volume of the RS, FC and MG63 cells is in a similar range. However, the cell area and the volume are influenced by the substrate.

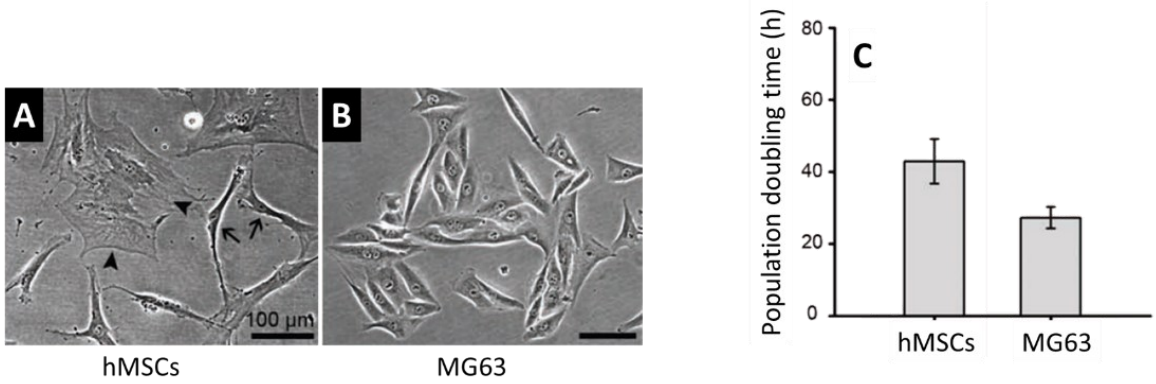

Figure 5.26 - Phase-contrast images of hMSC (A) and MG63 (B) cells and their growth characteristics (C). Modified from [22].

In vitro biocompatibility tests were also performed using the NIH-3T3 fibroblast murine cell line. This cell line is generally considered as a suitable cell model for studying material biocompatibility [23] and was already used for the determination of biological properties of titanium implant [24, 25].

Cells grow in a medium (Dulbecco Modified Eagle's Medium, DMEM) containing 10% fetal bovine serum (FBS) and 1% of penicillin/streptomycin, frequently refreshed. During routine culture, the cells where maintained at 60–80% confluence in T75 culture flasks, in a humidified incubator at 37 °C and 5% CO_2.

5.3.2. Sterilization and conditioning

Polymer-based biomaterials are sterilized with ethanol (EtOH) 70% for 30 min, washed with phosphate buffered saline (PBS) and UV irradiated for 30 min each side. On the other hand, metal biomaterials are

autoclaved at 120 °C for 20 min. After sterilization, samples were conditioned overnight with DMEM additioned with 10% of FBS and 1% of penicillin/streptomycin (conditioning medium).

5.3.3. Cytotoxicity evaluation

The conditioning medium derived from sample is used for incubating cells, in order to evaluate the cytotoxicity of biomaterial and 3D structure, intended as residues of manufacturing and/or surface coating. Viability of cells cultured with conditioning medium is tested by viability assay described below. Fresh medium is usually used as control.

5.3.4. Cell seeding

For cell culturing, scaffolds are placed in wells plate and, after preconditioning, cells are seeded in each scaffold with a seeding density depending on cell lineage, substrate and aim of experiment. Plates were incubated at 37°C and 5% CO_2, and medium is replaced frequently. After the incubation time planned by the experiment (e.g. 24 hours, 7 days, etc.), cell vitality is assessed by viability assays.

5.3.5. Cell viability assay

Cell health can be monitored by numerous methods: plasma membrane integrity, DNA synthesis, DNA content, enzyme activity, presence of ATP, and cellular reducing conditions are known indicators of cell viability and cell death.

5.3.5.1. Alamar Blue assay

The In Vitro Toxicology Assay kit, Resazurin based (TOX8-1KT Sigma) is a non-toxic vital dye known as *Alamar Blue*. The method is based on the evaluation of the relationship between NADPH/NADP, FADH/FAD, FMNH/FMN and NADH/NAD[5], which increases during cell proliferation. Alamar Blue is reduced by the above-mentioned metabolic intermediates and the process is accompanied by a variation in the fluorescence emitted, which can be quantified as a colorimetric variation from the blue (oxidized form) to the pink (reduced form) by the fluorimeter.

5.3.5.2. MTT assay

To evaluate the mitochondrial activity of all cultured cell conditions, was performed a test with 3-(4,5-dimethylthiazole-2-yl)-2,5 diphenyl tetrazolium bromide, which allows to evaluate vitality and cell growth is that which involves the use of a yellow tetrazole salt (MTT) which is transformed into formazan, purple

[5] FAD - Flavin Adenine Dinucleotide; FMN - Flavin Mono Nucleotide; NAD - Nicotinamide Adenine Dinucleotide; NADP - Nicotinamide adenine dinucleotide phosphate and their respective reduced form (NADPH, FADH, FMNH and NADHH), are coenzymes that cooperate in oxidation-reduction processes for the formation of adenosine triphosphate (ATP), primary carrier of energy in cells.

crystals from metabolically active cells, because the reaction involves NADH and NADPH cofactors. Formazan crystals are then solubilized to obtain a colored solution of which the absorbance can be measured.

5.3.6. Cell morphology

Information on cellularised scaffolds, gained from scanning electron microscope (SEM) observation, range from the overall behaviour of the cell culture to the state of wellness of individual cell. In particular, cell density and distribution are indications of scaffold biological response *in vitro*. Suitability of scaffold surface and/or coating are revealed by cell spreading and adhesion, detectable studying cell morphology. Starting from the points of contact between cell and substrate (focal adhesion), actin protrusion generates lamellipodia and filopodia, essential to understand the cell functional interactions with substrate. In addition, the production of surface vesicles is a signal of cellular communication.
Biological sample preparation for SEM observation involves:

1) fixation (in 2% glutaraldehyde in 0.1 M sodium cacodylate buffer), to interrupt the autolytic processes that develop in the cell and better preserve its structural morphology;
2) washing (in 7% sucrose in 0.1 M cacodylate buffer), to remove the excess of fixative that did not interact with the tissue components and remained in the sample;
3) post-fixation in 1% osmium tetroxide. This is an useful procedure step for increasing the compositional contrast between the biological material and the 3D substrate;
4) complete dehydration, achieved in two phases: (a) graded alcohol series, up to 100% and (b) sublimation of previously frozen biological material, under particular conditions of temperature and pressure by Critical Point Dry (CPD) or Lyophilization techniques.

5.3.7. Cell adhesion

After the culture time of interest for the experiment, the activation of the Focal Adhesion Kinase (FAK), a protein involved in the adhesive process, is measured in the substrate by Enzyme-Linked Immunosorbent Assay (ELISA). When the cell interacts with the substrate, phosphorylation of FAK in P-FAK (addition of the PO_4 group) gives rise to a signaling pathway that leads to cell anchoring on the biomaterial, accompanied by cell spreading. ELISA assay is based on the measurement of phosphorylated FAK and total FAK. The greater the amount of phosphorylated FAK (extracted from sample by cell lysis) on the total FAK quantity, the more pronounced will be the phenomenon of cell adhesion.

Characterization techniques from advanced laboratory instrumentations, allow to fully characterized biomaterials and biomedical devices, under the point of view of:

- Morphology of biomaterial starting powder, scaffold surface and inner porous network (after cut);
- Surface coating morphology and adhesion;
- Cells morphology and *in vitro* behavior;
- Chemical composition and element distribution;
- Crystallinity, phases amount and eventual modification of lattice parameters, due to manufacturing process;
- 3D porous network and material distribution quantification, defects and structure visualization;
- Surface roughness;
- Mechanical and biological performances of biomaterials and scaffold *in vitro*.

Moreover, association of these techniques enable to achieve robust correlation among scaffold properties and performances, providing reliable indications of the analysed scaffold, *in vivo* perspective.

References

[1] Goldstein, J. I., Newbury, D. E., Michael, J. R., Ritchie, N. W., Scott, J. H. J., & Joy, D. C. (2017). Scanning electron microscopy and X-ray microanalysis. Springer.

[2] Reimer, L. (2000). Scanning electron microscopy: physics of image formation and microanalysis.

[3] Goldstein, J.I. & Yakowitz, H. (1975) Practical Scanning Electron Microscopy, Plenum Press, New York.

[4] Armigliato, A. & Valdrè, U. (1984) Microscopia Elettronica a Scansione e Microanalisi, Lo Scarabeo, Bologna.

[5] Wells O.C. (1974) Scanning Electron Microscopy, McGraw Hill, New York.

[6] https://myscope.training/index.html#

[7] Waseda, Y., Matsubara, E., & Shinoda, K. (2011). X-ray diffraction crystallography: introduction, examples and solved problems. Springer Science & Business Media.

[8] Hu, Q., Tan, Z., Liu, Y., Tao, J., Cai, Y., Zhang, M., ... & Tang, R. (2007). Effect of crystallinity of calcium phosphate nanoparticles on adhesion, proliferation, and differentiation of bone marrow mesenchymal stem cells. Journal of Materials Chemistry, 17(44), 4690-4698.

[9] Cui, H., & Sinko, P. J. (2012). The role of crystallinity on differential attachment/proliferation of osteoblasts and fibroblasts on poly (caprolactone-co-glycolide) polymeric surfaces. Frontiers of Materials Science, 6(1), 47-59.

[10] Giuliani, A., & Cedola, A. (Eds.). (2018). Advanced High-Resolution Tomography in Regenerative Medicine: Three-Dimensional Exploration into the Interactions between Tissues, Cells, and Biomaterials. Springer.

[11] Landis, E. N., & Keane, D. T. (2010). X-ray microtomography. Materials characterization, 61(12), 1305-1316.

[12] Betz, O., Wegst, U., Weide, D., Heethoff, M., Helfen, L., LEE, W. K., & Cloetens, P. (2007). Imaging applications of synchrotron X-ray phase-contrast microtomography in biological morphology and biomaterials science. I. General aspects of the technique and its advantages in the analysis of millimetre-sized arthropod structure. Journal of Microscopy, 227(1), 51-71.

[13] Betz, O., Wegst, U., Weide, D., Heethoff, M., Helfen, L., LEE, W. K., & Cloetens, P. (2007). Imaging applications of synchrotron X-ray phase-contrast microtomography in biological morphology and biomaterials science. I. General aspects of the technique and its advantages in the analysis of millimetre-sized arthropod structure. Journal of Microscopy, 227(1), 51-71.

[14] ASM, I. (2000). Mechanical Testing and Evaluation, Volume 8 of the ASM Handbook.

[15] ISO. ISO 13314:2011: Mechanical Testing of Metals—Ductility Testing—Compression Test for Porous and Cellular Metals; International Organization for Standardization (ISO): Geneva, Switzerland, 2011.

[16] ASTM D 1621e10, Standard Test Method for Compressive Properties of Rigid Cellular Plastics.

[17] (ASTM C1424-15(2019) Standard Test Method for Monotonic Compressive Strength of Advanced Ceramics at Ambient Temperature).

[18] Kutz, M. (Ed.). (2002). Handbook of materials selection. John Wiley & Sons.

[19] Chang, H. I., & Wang, Y. (2011). Cell responses to surface and architecture of tissue engineering scaffolds. InTechOpen.
[20] Williamson, J.B.P. (1968), "Topography of Solid Surfaces," in Interdisciplinary Approach to Friction and Wear (P.M. Ku, ed.), SP-181 pp. 85–142, NASA, Washington, D.C.
[21] Tobiasch, E. (2011). Differentiation potential of adult human mesenchymal stem cells. In Stem Cell Engineering (pp. 61-77). Springer, Berlin, Heidelberg.
[22] Docheva, D., Padula, D., Popov, C., Mutschler, W., Clausen-Schaumann, H., & Schieker, M. (2008). Researching into the cellular shape, volume and elasticity of mesenchymal stem cells, osteoblasts and osteosarcoma cells by atomic force microscopy. Journal of cellular and molecular medicine, 12(2), 537-552.
[23] Rejmontová, P., Capáková, Z., Mikušová, N., Maráková, N., Kašpárková, V., Lehocký, M., & Humpolíček, P. (2016). Adhesion, proliferation and migration of NIH/3T3 cells on modified polyaniline surfaces. International journal of molecular sciences, 17(9), 1439.
[24] Teng, F. Y., Ko, C. L., Kuo, H. N., Hu, J. J., Lin, J. H., Lou, C. W., ... & Chen, W. C. (2012). A comparison of epithelial cells, fibroblasts, and osteoblasts in dental implant titanium topographies. Bioinorganic chemistry and applications, 2012.
[25] Alves, A. C., Thibeaux, R., Toptan, F., Pinto, A. M. P., Ponthiaux, P., & David, B. (2019). Influence of macroporosity on NIH/3T3 adhesion, proliferation, and osteogenic differentiation of MC3T3-E1 over bio-functionalized highly porous titanium implant material. Journal of Biomedical Materials Research Part B: Applied Biomaterials, 107(1), 73-85.

6. Experimental results and discussion

6.1. Metals

6.1.1. Titanium alloys

6.1.1.1. Ti6Al4V

Aim: The aim of the work[6] is to fabricate suitable scaffolds in Ti6Al4V for *in vivo* perspectives starting from industrial electron beam powder bed fusion process based on cost and waste reduction (reused powder) in order to overcome issues connected to the high costs of preclinical studies.

Abstract: Although cellularized scaffold is a promising solution for tissue regeneration and recovery of damaged physiology functions, the high cost of preclinical studies creates a gap between investigation and device market for the biomedical industry. In this work, bone scaffolds based on the Ti6Al4V alloy, manufactured by EB-PBF with reused powder, were investigated, aiming to overcome issues connected to the extensive investment for preclinical device development. Two different elementary unit cell geometries, namely diamond and rhombic dodecahedron, were adopted for scaffold creation. Surface functionalization was performed by coating scaffolds with a single layer of polycaprolactone (PCL) or with mixture of polycaprolactone and 20 wt.% hydroxyapatite (PCL/HA). The mechanical and biological performances of the produced scaffolds were investigated, and the results were compared to software simulation and experimental evidence available in literature to verify the feasibility of our industrial approach. Good mechanical properties and a favorable environment for cell growth were obtained for all combinations of scaffold geometry and surface functionalization.

State of art: Scaffold needs suitable mechanical properties for load-bearing applications and biological requirements of mass transport [2]. Both these features relate to porosity, pore size and pore interconnectivity, that in turn are determined by scaffold elementary unit cell geometry [3, 4]. Elementary unit cell geometry is mainly of two different types: a) diagonal symmetrical or b) midline symmetrical. Finite elements analysis (FEA) [5] showed that porous structure with midline symmetry exhibits superior compressive performances than diagonal symmetry, although the opposite trend was observed in case of torsion. Therefore, rhombic dodecahedron (RD) is well suited for load-bearing implants that directly support the weight of the body, while diamond (DO) is well suited for implants requiring large torsional forces. In addition, numerical analysis with computational fluid dynamics (CFD) [6] showed that DO has some advantages on implant fixation (greater tortuosity and larger aperture), gentle cell growth environment (more appropriate adhesion areas), and tissue regeneration (due to regular mechanical stimulation) compared to midline-symmetrical shape, while RD has superior mass transfer performances (due to bigger flow velocity). Therefore, DO and RD elementary unit cells promise to be valid alternatives for scaffolds with suitable mechanical and biological features for bone tissue regeneration.

[6] Published paper: [1]

Accurate control of size and topology of scaffold elementary unit cell can be efficiently obtained by using Additive Manufacturing (AM) technology of electron beam powder bed fusion (EB-PBF), commonly employed for patient-specific bone implants in titanium alloys [7, 8]. The combination of EB-PBF technology and Ti6Al4V alloy was experienced by Popov et al. [7], that produced biomedical patient-specific implants for clavicle, mandibular bone, foot osteotomy and hip. In all clinical cases reported, EBM revealed reduction of time in operation and patient recovery.

Despite key advantages of EB-PBF technology combined with Ti6Al4V alloy, only a small percentage of tissue engineering research achieves clinical application, due to the high cost of pre-clinical studies. To overcome this gap, Martinez-Marquez et al. [9] proposed a step model to follow for ensuring an effective cost-effectiveness of custom bone scaffold. One of the steps concerns cost reduction through recycling of material feedstock, whose cost can reach up to 31% of the whole EB-PBF built part [10]. Recycling of Ti6Al4V metal powder represents an affordable solution to reduce waste and save cost, providing the same quality of parts produced from virgin powder [11]. Several preheating steps and prolonged thermal holding in high vacuum conditions, cause properties change in Ti6Al4V powder, in terms of chemical composition, morphology and physical properties [12]. Furthermore, thermal cycles and manipulation induce oxygen uptake, with the risk to overcome the <0.2 wt.% content, required for Ti6Al4V ELI (ASTM F2924-14).

For implant success, also surface functionalization is an engineering aspect to be improved, to fulfill scaffold-bone interface requirements and avoid the release of toxic ions [3, 4]. The most common functionalization treatment is coating the scaffold surface by a layer of biocompatible material or a combination of biocompatible compounds, such as polycaprolactone/hydroxyapatite (PCL/HA). Among the various techniques to perform coating deposition on titanium alloys, dip coating offers several advantages such as inexpensive setup, process simplicity, uniformity of deposition, low processing temperature and the ability to uniformly coat complex shapes and patterns. Coating thickness can be easily controlled by adjusting solution concentration, dipping time and withdrawal speed. Lack of heat treatment for coating densification allows to avoid HA phase transformation into non-crystalline phase, which increases dissolution rate in body fluid and enhances micro-cracks formation due to thermal stresses at substrate-coating interface [13].

Material and methods:

- Scaffolds were produced using a mixture of Ti6Al4V powder (Arcam) in recycled and virgin new conditions, blended in unknown proportions;
- Scaffolds were additively manufactured by Arcam A2X electron beam powder bed fusion system;
- Scaffolds were designed (Magics 21.0) with diamond (DO) and rhombic dodecahedron (RD) elementary unit cell (Figure 6.1). Scaffold volume corresponds to a cube 10 mm side length, nominal porosity is 80% and strut size 420 μm for DO and 460 μm for RD;

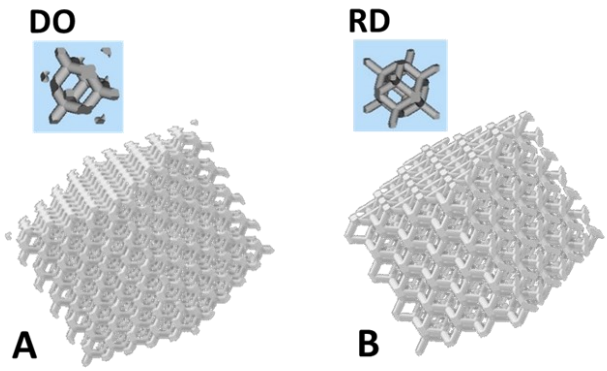

Figure 6.1 - Schematics of the scaffolds elementary unit cell geometry: (A) diamond (DO) and (B) rhombic dodecahedron (RD).

- The total volume of residual powder remained entrapped in the scaffold pores (Table 6.1) is estimated from experimental measurement of scaffold mass (m_s) by using precision balance and five weighing operations. The mass of residual powder (m_{pw}) was obtained from Eq. 6.1:

$$m_s = m_{Ti} + m_{pw} \quad (6.1)$$

  where m_s is scaffold mass, m_{Ti} mass of struts calculated from XμCT porosity data and alloy nominal density (ρ_{Ti} = 4.43 g/cm^3) and m_{pw} total mass of unremoved residual powder. Residual powder volume (V_{pw}) was calculated from residual powder density ρ_{pw} = 0.68 ρTi = 3.012 g/cm^3, as suggested by Tolochko et al. [14].
- Surface functionalization was performed by manual dip coating the scaffolds for 20 s in a bath of a) PCL or b) a mixture of PCL/HA (20 wt.%) (solutes) and tetrahydrofuran (solvent), followed by air drying.
- Scaffolds were characterized by scanning electron microscope (SEM), energy dispersive spectroscopy (EDS), X-ray diffraction (XRD), X-ray micro-computed tomography (XμCT), roughness measurements and mechanical compressive test.
- Scaffold biological performances were tested by hMSCs viability at 24h and 4 days, ELISA essay and cell morphology.

Main results and discussion:

Residual powder volume and porosity

Independently of geometry (DO or RD), the top surface of the scaffolds is formed of partially melted particles with well interconnected open pores. The scaffold inners structure showed pores partially filled with unmelted and neck-connected powder particles (Figure 6.2A and B). Images in Figure 6.2 were taken in the central part (core) of the cut scaffold (5 mm). High density residual powder in DO geometry (Figure 6.2A) with total occlusion of most pores was clearly evident. In contrast, RD geometry (Figure 6.2B) has pores only partially

occluded. It is worth noting that SEM observations of the peripheric regions, far from the scaffold core, show open pores free from residual powder.

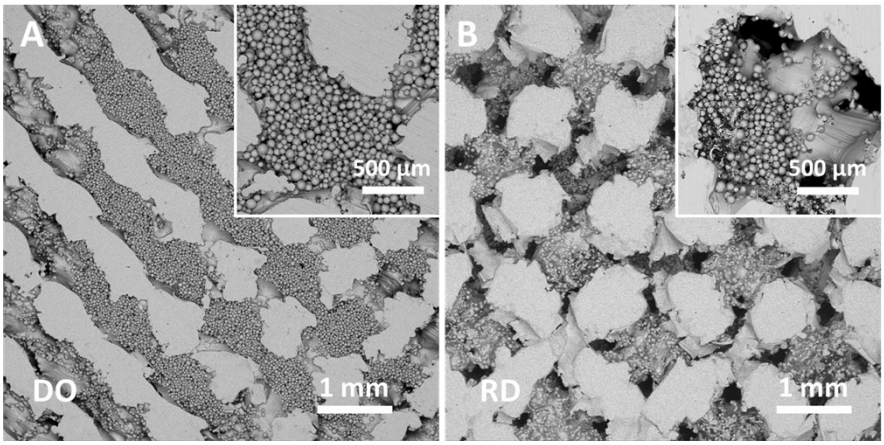

Figure 6.2 - SEM images of the scaffold inner structure: (A) DO geometry, (B) RD geometry. Insets show the same area of sample at higher magnification.

From the data in Table 6.1, it was evident that the amount of residual powder inside the scaffold strongly depended on geometry, with DO containing about 76% more residual powder than RD, due to a more intricate pore pathway for the release of unmelted powder remained entrapped inside the scaffold. The relative density ($\rho = 1 - p$), where p is the scaffold porosity, as defined by Zhou et al. [15], could be also estimated from data in Table 6.1. For both geometries, the relative density r result was 37%.

Table 6.1- Experimental values resulting from XμCT analysis and calculated values of residual powder weight (m_{pw}) and volume (V_{pw}). m_s - total scaffold mass; V_s - total scaffold volume; m_{Ti} – total mass of struts; V_{Ti} - total volume of struts; mpw - total mass of residual powder; V_{pw} - total volume of residual powder.

Geometry	***Porosity (%)***	***m_s (g)***	***V_s (cm^3)***	***m_{Ti} (g)***	***V_{Ti} (cm^3)***	***m_{pw} (g)***	***V_{pw} (cm^3)***
DO	63	1.94	1	1.64	0.37	0.30	0.0996
RD	63	1.81	1	1.64	0.37	0.17	0.0564

Scaffold characterization

Experimental chemical composition of the scaffolds obtained by EDS analysis (Table 6.2) was almost the same for both DO and RD geometries, showing a slight decrease of vanadium with respect to the experimental composition of recycled powder (P1) and new virgin Ti6Al4V powder (P2). XRD pattern of DO and RD scaffolds confirmed the presence of α-Ti and β-Ti phases, suggesting that the vanadium decrease measured by EDS was incapable of deeply changing the alloy microstructure.

Table 6.2 - Chemical composition of scaffold obtained by EDS analysis, compared with recycled (P1) and new (P2) Ti6Al4V powders. AV – Average Value, SD – Standard deviation.

	P1 [wt. %]		P2 [wt. %]		Scaffold [wt. %]	
	AV	**SD**	**AV**	**SD**	**AV**	**SD**
Al	5.8	0.2	6.1	0.4	6.0	0.5
Ti	90.60	0.14	90.5	0.2	91.7	0.7
V	3.60	0.11	3.4	0.2	2.4	0.2

Mechanical tests

Compression tests carried out on scaffolds provided the mechanical behavior shown in Figure 6.3 for DO and RD geometries. The gradual collapse of scaffold elementary unit cells arranged on the scaffold layers was clearly evident in the DO curve, up to 40% reduction of initial scaffold height. The DO curve grew rapidly up to maximum stress value, corresponding to the compression strength, then large oscillations due to collapse of unit cells under compressive load followed. The collapse mechanism was clearly described by Ahmadi et al. [16] and Del Guercio et al. [17]. On the other hand, the RD curve after its first rise showed small oscillations around the same average stress value (Figure 6.3), in agreement with the results in literature [5,16].

However, contrary to the results in literature, DO and RD curves in Figure 6.3 reached the same stress value in the final part of the curve at high strain values. The two curves were completely superimposed above 35% strain, when the unit cells were all collapsed, and the scaffold structure arrived at compaction (Figure 6.3).

Ahmadi et al. [16] reported the trend of compression strength and yield stress as a function of relative density for DO and RD geometries, showing that for relative density below 25% the two curves were superimposed, while for higher values RD always exhibited higher mechanical properties against DO.

The relative density of scaffolds, obtained by experimental calculation of porosity from XμCT analysis, was 37% with compression strength of RD (78 MPa) lower than DO (99 MPa), as reported in Table 6.3.

Generally, the mechanical behavior of the scaffolds strongly differed from the results of Li et al. [5] and Ahmadi et al. [16] for similar structures (Table 6.3). In particular, the large size of struts (ranging from 800 to 1000 μm) in tested scaffolds determined the elastic behavior (Young modulus) and compression strength of DO and RD geometries (Table 6.3).

Following Ahmadi et al. [16], the more complex unit cell geometry (RD) exhibited lower elastic properties (Table 6.3), while absolute values of Young modulus were always lower than the values from Li et al. [5] for similar cell geometries with lower strut size and lower relative density (Table 6.3). Therefore, higher strut size gives rise to stiffer structures with different behaviors for different unit cell geometries. In our case, both strut size and the absence of structural defects inside the struts (Figure 6.3) were responsible for higher compression strength of DO with respect to RD (Table 6.3).

Compression failure of a single strut caused collapse of an entire elementary unit cell, then producing the large oscillations visible in the DO curve in Figure 6.3. As the collapse of elementary unit cells occurred from outside to inside during compression, the first part of the stress–strain curve (Figure 6.3) was not influenced by the residual powder stored in the scaffold core (Figure 6.2).

However, when all external elementary unit cells had collapsed, elementary unit cells in the scaffold core that were partially filled with sintered residual powder, started to deform. On collapse of core elementary unit cells, the scaffold mechanical properties became dependent on sintered residual powder, which increased compressive stress and stress on struts in the longitudinal direction perpendicular to the compressive force. In this way, differences in mechanical properties linked to different elementary unit cell geometry vanished, overruled by the presence of residual powder, so stress-strain curves of DO and RD unit cells coincided.
It is worth noting that the compression strength at 40% of our scaffolds is very close to the experimental value of cortical bone (Table 6.3), suggesting that the presence of residual sintered powder did not deteriorate the mechanical performance of the scaffolds.

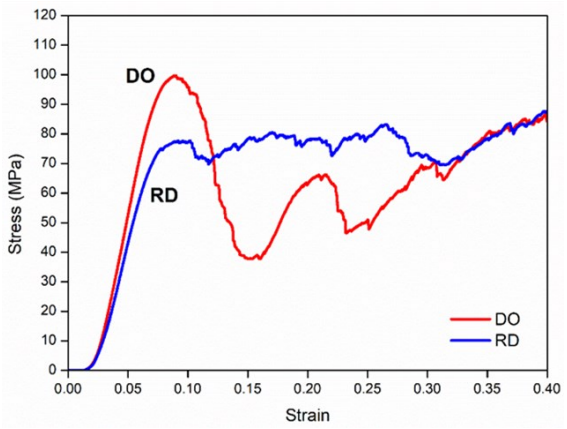

Figure 6.3 - Mechanical behavior of scaffolds under compression for DO and RD geometries.

Maximum stress value at first peak was assumed as compression strength, after Li et al. [5]. Stress-strain curves in Figure 6.3 also allowed the calculation of Young modulus and compressive strength at 40% of strain. Results are summarized in Table 6.3 with values obtained by Li et al. [5] and Ahmadi et al. [16] for comparison. Table 6.3 also shows reference values for cortical bone. It is worth underlining that the values of porosity and relative density reported in Table 6.3 for this work referred only to struts without any contribution from residual powder. Therefore, discrepancies between software calculated and experimental values were fully due to the EBM manufacturing technique. In particular, the EB-PBF processing allowed scaffold to be obtained with a strut size much larger (ranging from 800 to 1000 µm for both DO and RD geometries) than the nominal CAD values. Thus, all values in Table 6.3 can be reliably compared.

Table 6.3 - Experimental results obtained from the compression tests compared to the results obtained by Li et al. [5] and Ahmadi et al. [16]with the same scaffold geometries, and reference values for cortical bone.

Reference	Porosity (%)	Relative density (%)	Young modulus (GPa)	Compression strength (MPa)	Compression strength at 40% (MPa)

	DO	RD	DO	RD	DO	RD	DO	RD	DO	RD
This work	63	63	37	37	1.949±0.001	1.622±0.001	99	78	86	88
Li et al. (2019)	70	70	30	30	2.59±0.13	4.89±0.05	88±5	174±4		
Ahmadi et al. (2015)	80	72	20	28			45	80	30	70
Cortical bone					3.9 - 11.7				80	

Surface functionalization

Coating is continuous and well-adhered to the scaffold top surface as well as to surface of inner struts, when the coating penetrated inside the scaffold. Coating reduces scaffold surface roughness resulting in a smoothing effect leading to thickness variation of coating. The coating on the top surface always exhibits a porous structure due to solvent evaporation.

Scaffold interaction with hMSCs

In all scaffold conditions (coated and uncoated) and geometries (DO and RD), hMSCs morphology suggested that after 24 h incubation, cells were in the spreading phase on the scaffold surface. After 4 days incubation, cells starting to colonize scaffold inner layers.

ELISA essay analysis of FAK phosphorylation in hMSCs revealed that P-FAK was highly upregulated in cells grown on DO compared with cells grown on RD, indicating activation of FAK signaling by geometry cues (Figure 6.4). A higher value of P-FAK/FAK of DO geometry corresponds to a greater number of viable cells attached to the scaffold. Therefore, since cell adhesion is a regulator of cellular proliferation, migration and differentiation [18], this result suggests a better biological response of the DO unit cell geometry against RD, in perfect agreement with the numerical analysis by Li et al. [6]. Coatings improved the biological behavior of stem cells.

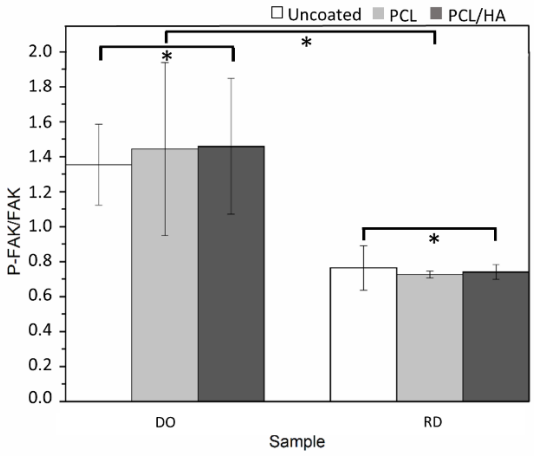

Figure 6.4 - The activation level of FAK was measured by ELISA assay after 24h of incubation onto the different scaffolds. Bar graphs show P-FAK values normalized on the total FAK - $p < 0.05$.

Conclusions:

- EB-PBF technology is suitable for the production of porous structures with controlled topology and well-defined unit cell geometry showing appropriate biological performance and surface characteristics for *in vivo* perspectives. The surface roughness typical of the EB-PBF process promotes hMSC proliferation, while the partially sintered residual powder in the scaffold core is responsible for the porosity mismatch between experimental and CAD design values;
- The mechanical performance of the scaffold is mainly influenced by elementary unit cell geometry. The presence of residual powder becomes evident for compression values outside the range of *in vivo* use of the device and tends to cancel out the differences between geometries. In general, the compression behavior of the scaffolds is quite similar to natural bone tissue and follows trends reported in literature, although strut size and the absence of structural defects inside the struts are responsible for the higher compression strength of DO against RD;
- Short-term cell viability and metabolic protein quantification identifies DO as a better biological environment than RD, in agreement with literature-reported numerical simulations. After 4 days incubation, hMSCs start to penetrate inside the scaffold, favored by adherent, continuous and protective layers of PCL and PCL/HA.

From the above results it is evident that powder recycling represents a convenient industrial practice applicable to the manufacture of biomedical devices to heavily reduce preclinical costs without altering biomechanical performance.

6.1.1.2. Ti48Al2Cr2Nb

Aim: This work[7] aimed to investigated the biological response of Ti-48Al-2Cr-2Nb (γ-TiAl alloy) in terms of adhesion, short-term viability and proliferation of NIH-3T3 cells on lattice scaffold manufactured by electron beam powder bed fusion (EB-PBF), never previously studied.

Abstract: Gamma titanium aluminides (γ-TiAl), especially Ti-48Al-2Cr-2Nb alloy, were originally developed in combination with electron beam powder bed fusion (EB-PBF) for aerospace applications, due γ-TiAl low density, very high mechanical strength and good oxidation and corrosion properties in aggressive environments. In spite of these excellent properties, the well-known biological performances of Ti-48Al-2Cr-2Nb alloy are never been investigated using complex 3D porous structures, accurately produced by EB-PBF. The present experimental study assesses the behavior of NIH-3T3 cells on Ti-48Al-2Cr-2Nb lattice scaffold with dodecahedral elementary cell, manufactured by the EB-PBF process. The results show that Ti-48Al-2Cr-2Nb lattice scaffold represents a promising new entry in the bone tissue engineering field.

State of art: Biocompatibility of γ-TiAl has extensively studied, compared to titanium alloy usually employed in bone repair and replacement. Human fetal osteoblast cells, cultured on γ-TiAl and Ti-6Al-4V disks, show comparable growth and attachment, suggesting that Ti-48Al-2Cr-2Nb is not toxic to osteoblasts. Additionally, the presence of collagen type I and osteonectin, observed on both substrates, is a clear indication that Ti-48Al-2Cr-2Nb allows cells to produce the extracellular matrix, thus resulting biocompatible with the osteoblast cells [19]. The potential of γ-TiAl as a biomaterial was successfully evaluated also *in vivo* by Castaneda-Munoz et al. [20], using a rat model. Ti–48Al–2Cr–2Nb bulk cylinders produced by hot isostatic pressing, implanted in the rat femur, allow proliferation and growth of bone cells (normal bone growth processes) and osseointegration, without signs of rejection of the implant in six months. Thus, γ-TiAl appears to elicit a normal bone tissue reaction and hence, has potential as a metallic implant material.
However, studies investigated mainly the cytotoxicity and biocompatibility, both *in vitro* [19, 21] and *in vivo* [20], and several strategies to enhance corrosion behavior of Ti-48Al-2Cr-2Nb bulk sample produced by conventional processes [22-24]. No attempts have been made so far to evaluate the biological performances of Ti-48Al-2Cr-2Nb 3D lattice structure, whose intricate shapes could be produced by metal additive manufacturing, such as Electron Beam Powder Bed Fusion (EB-PBF) technology [25]. The EB-PBF is the most commonly used method in the production of γ-TiAl alloy parts. In fact, since the γ-TiAl alloy has a brittle structure at room temperature, the use of high preheating during production prevent damage due to thermal or residual stresses, making the EB-PBF a very suitable method for γ-TiAl alloys [26].

Materials and methods:

- Scaffolds were produced using Ti48Al2Cr2Nb (Ti-48-2-2) powder (Arcam);

[7] Paper in submission to *3D Printing and Additive Manufacturing* journal: Galati, M., Gatto, M.L., Bloise, N., Fassina, L., Saboori, A., Visai, L., Mengucci, P., Iuliano, L. (2022). Electron beam powder bed fusion of Ti-48Al-2Cr-2Nb open porous scaffold for biomedical applications: process parameters optimisation, adhesion and proliferation of NIH-3T3 cells.

- Scaffolds were additively manufactured by Arcam A2X electron beam powder bed fusion system. Process parameters were optimized to obtain a fully dense structure with no defect;
- Dodecahedral elementary cell (inset in Figure 6.5) with side length of 3 mm and strut thickness of 0.29 mm was selected. Scaffold nominal volume is to a cube 10 mm side length and nominal porosity is 96% (Figure 6.5);

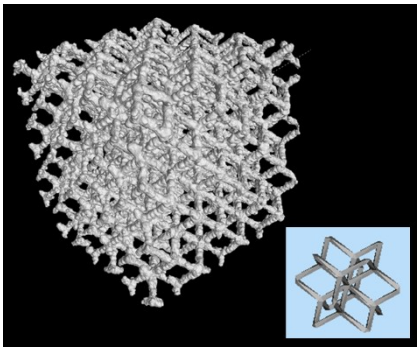

Figure 6.5 - Schematic of lattice scaffold with dodecahedral elementary cell geometry (in inset).

- Scaffold porosity [%] was calculated according to Eq. 6.2:

$$P\,[\%] = \frac{Vnom - Veff}{Vnom} \times 100 \qquad (6.2)$$

Where: V_{nom} is the nominal volume of scaffold (1 cm^3), while V_{eff} is the effective volume occupied by scaffold material. This latter term is the ratio between scaffold weight (W) and material density (ρ_{mat}). Scaffold weight from 6 measurements is W = 0.63 ± 0.03 g and Ti48Al2Cr2Nb density value was assumed ρ_{mat} = 4.04 g/cm^3.

- Scaffold was characterized by field emission scanning electron microscope (FESEM), energy dispersive spectroscopy (EDS), X-ray diffraction (XRD), X-ray micro-computed tomography (XμCT).
- Scaffold biological performances were tested by NIH-3T3 viability at 1, 4 and 7 days, DNA content after 1, 4 and 7 days of incubation and cell morphology.

Main results:

Scaffold analysis

Process parameters optimized for the scaffold production allow complete and well-defined scaffold struts with a small number of defects and relative density of 99.9%. Chemical composition of the scaffold, within the experimental error, it is close to the values of the powder. Compared to the powder counterpart, the phase γ-TiAl remains the predominant phase, though the γ-TiAl peaks of the scaffold are markedly weaker than those of the raw powder, due to non-homogeneous scaffold surface, but also suggesting a low crystallization.

Residual stresses and/or variations in crystalline state of scaffolds could be responsible for the slight angular peak shift.

Scaffold morphometry

Scaffold morphometric parameters from XμCT analysis are reported in Table 6.4. The average strut thickness of scaffold results larger than the nominal one (0.29 mm). This result is explained because of the impractical control of the effective electron beam diameter and corresponding melt pool, depending simultaneously on the beam current, focus offset, and beam speed [21]. The larger strut thickness causes a reduction of scaffold total porosity (82%) respect to the designed one (96%), as confirmed also by porosity evaluated according to Equation (2) (84%). However, this porosity value allow for easy removal of unfused powder from pores by conventional cleaning procedures, thus favoring cell colonization.

Table 6.4 - Lattice scaffold morphometric parameters obtained from XμCT analysis.

Average strut thickness [mm]	0.37 ± 0.03
Average macro-pore size [mm]	1.50 ± 0.11
Total porosity [%]	82

Biological test

Cells plated on a standard tissue culture plate (TCPS) were used as a positive control. As shown in Figure 6.6a, at day 7, a significantly difference of cell growth was observed in Ti-48-2-2 compared to day 1. Remarkably, DNA measurement corroborated the above data, significantly increasing after 7 days of cells incubation (Figure 6.6b). Overall, these data demonstrated that the metabolic activity significantly increased over time.

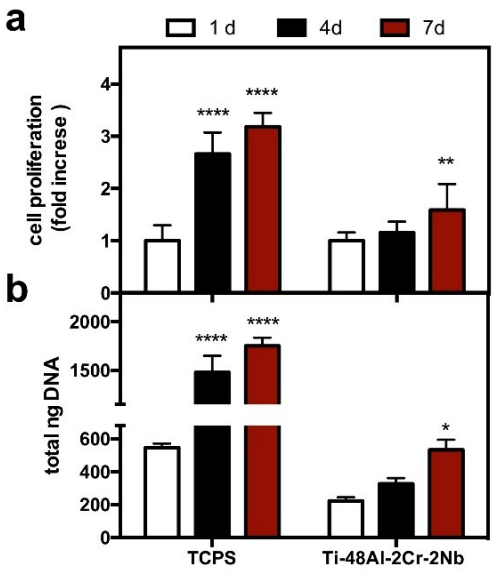

*Figure 6.6 - Ti-48-2-2 scaffold biocompatibility after 1, 4, and 7 from NIH-3T3 cell seeding (a) and DNA content (b). **** $p < 0.0001$; **$p < 0.01$; and *$p < 0.05$.*

FESEM observations of NIH3T3 cells after 7 days of culture (Figure 6.7) show cell colonization and a robust spreading of healthy and flattened-shape cells covering Ti-48-2-2 strut (Figure 6.7a). Cells adhere to powder particles partially melted on scaffold surface (Figure 6.7b) with noticeable filopodia extensions and cellular protrusions (inset in Figure 6.7b), clearly evidencing the binding between NIH-3T3 and Ti-48-2-2.

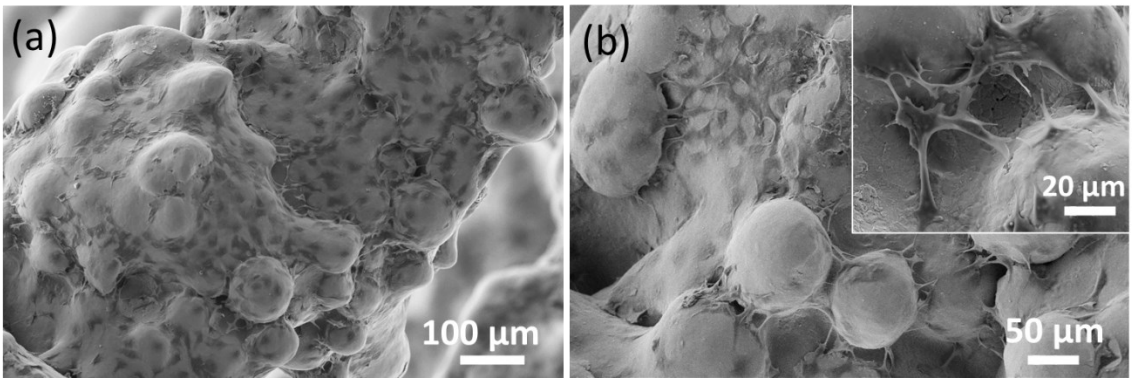

Figure 6.7 - FESEM micrographs of NIH-3T3 cells after 7 days of incubation on Ti-48-2-2 scaffold. Cells cover scaffold strut (a) by preferentially adhere to surface powder particles partially melted (b) through filopodia and protrusion (inset in b).

Conclusions:

- Optimised EB-PBF process allows obtained full dense Ti28Al2Cr2Nb lattice scaffold. Mismatch between nominal porosity from CAD and experimental calculated porosity of scaffold is due to EB-PBF manufacturing process; however the high porosity enables free-pores from residual powder and cell colonization of scaffold;
- Healthy and flattened-shaped cells have been observed on the scaffold surfaces with a uniform spreading and full cellular colonization of 3D structure has been achieved.

These preliminary results encourage further efforts and investigations on Ti-48Al-2Cr-2Nb scaffold manufactured by EB-PBF as a promising new entry in the bone tissue engineering.

6.1.2. Stainless Steels

6.1.2.1. 316L

Aim: The aim of this study[8] is programming the mechanical and biological behavior of 316L stainless steel scaffold produced by laser powder bed fusion for short-term clinical applications, by grading the lattice geometry of scaffold.

Abstract: Among the various metal materials used for tissue regeneration, the most cost-effective solution for short-term orthopedic implant is 316L stainless steel. Furthermore, graded lattice geometry is a potential solution to meet both the mechanical and biological need for bone regeneration, providing adaptative porous gradient and miming natural bone. In this experimental work, 316L graded lattice scaffolds were produced with two different strategies, starting from a rhombic dodecahedron elementary cell, using laser powder bed fusion (L-PBF) technology. Programmed mechanical performances of scaffolds were experimentally evaluated in relation of micro- and macro-structure of scaffolds. Furthermore, biological tests were performed in order to identify how environments generated by 3D structures could impact on cell behaviors.

State of art: Production technology of 316L biomedical devices could mitigate the potential failure of implant, by determining the corrosion behavior of the biomaterial. Additively manufactured 316L demonstrated superior biocompatibility in the aggressive biological environments compared to the wrought 316L [27]. In particular, the high corrosion resistance of sample produced by L-PBF limited the release of toxic ions into the biological environment, resulting in a better viability and proliferation of the pre-osteoblast cells, as investigated by Al-Mamun et al. [27]. Furthermore, Kong et al. [28] found an increase of cell concentration and proliferation in correspondence of the rise of laser power and, at about 200 W, samples showed considerably higher biocompatibility than the quenched 316L.

In the graded lattice structure, the functional grading (variation of size, typology, material or strut diameter [29]) allows to program the failure mechanism of scaffold, by controlling the local relative density of unit cells. Thus, graded filler enables to design a body implants with locally stiffness matching to that of the target bone [30].

Up to now, studies on 316L scaffolds produced by L-PBF technology covered only gyroid, lattice and lattice topology-optimized geometries [31-36]. The only study on optimization of 316L L-PBF graded lattice scaffold, for programming its plastic deformation behavior, is not applied on biomedical implant [30].

Materials and methods:

- Dense in and dense out graded lattice scaffold geometries (Figure 6.8) were designed by Autodesk Netfabb. Scaffold volume of 10×10×10 mm^3 was filled by a rhombic dodecahedral elementary cell

[8] Paper in preparation for *Journal of the Mechanical Behavior of Biomedical Materials*: Gatto, M.L., Mengucci, P. Groppo, R. Santecchia, E., Mattioli Belmonte, M., Cerqueni, G. (2022). 316L L-PBF graded lattice scaffolds with programmed mechanical performances for bone tissue regeneration.

(Figure 6.8a), repeated varying its dimension at each layer, along the scaffold built-direction. Elementary cell dimension was varied by linearly changing the strut thickness with a smooth transition between scaffold layers. Strut thickness of 0.25, 0.50 and 0.75 mm were respectively arranged in layers along scaffold built-direction, in incremental order from edge to core of scaffold in dense in geometry (Figure 6.8b) and from core to edge of scaffold for dense out geometry (Figure 6.8c). Both structures were mirrored with respect to central horizontal axis.

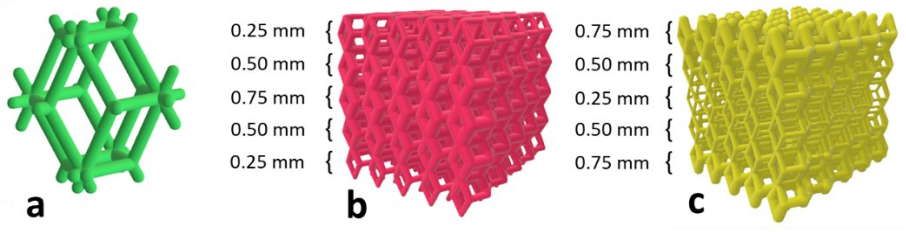

Figure 6.8 - Schematics of rhombic dodecahedron elementary cell (a), dense in (b) and dense out (c) graded lattice scaffold geometries.

- Dense in and dense out scaffold total porosity from the STL file is 58% and 72 %, respectively.
- Scaffolds were manufactured using 316L powder (LPV CARPENTER Technology) by L-PBF technology with a 3D4steel system (3D4Mec Srl, Sasso Marconi, Italy), using optimized printing parameters.
- Scaffold was characterized by scanning electron microscope (SEM), energy dispersive spectroscopy (EDS), X-ray diffraction (XRD), X-ray micro-computed tomography (XμCT), mechanical compressive test.
- Scaffold biological performances were tested by MG-63 human osteosarcoma cells viability and cell morphology at 24h and 7 days of incubation.

Main results:

Scaffold characterization

Some powder particles remained partially melted on skin-up surface of dense in and dense out graded lattice scaffold, after the manufacturing. Inner architecture of dense in and dense out scaffolds (cut at half height) shows well-defined and full dense struts. Pores are opened and interconnected in dense out, while appear partially occluded in dense in, determining the scaffolds porosity, obtained from XμCT analysis, as 50% for dense in and 70% for dense out. Within the experimental uncertainties, scaffolds present similar average chemical composition of 316L powder. XRD patterns of 316L dense in and dense out graded lattice scaffolds exhibit peaks corresponding to the austenitic phase (γ-Fe). The reduction of dense in and dense out scaffold peaks respect to the powder suggests a less crystallized γ-Fe phase.

Mechanical performances

Mechanical performances under compression of dense in and dense out graded lattice scaffolds are plotted in Figure 6.9 as load/strain curves. Scaffolds mechanical behavior under compression can be described by 4 phases, identified in Figure 6.9: I) Linear elastic phase - when loading starts, elastic behavior of porous structure generates a linear region. This structural deformation could be recovered; II) Plastic yielding phase - overcame the nominal yield point (*), the struts with lowest thickness (0.25 mm) gradually collapse causing a yield plateau; III) Plastic phase – the complete collapse of elementary cells with the lowest strut thickness provokes the compaction of the whole scaffold layer in which these cells are arranged; IV) Densification – after the total collapse of layers, the area of densified material flattened, i.e. there was no gap between layers of the lattice, by causing the sharp rise of compression curve.

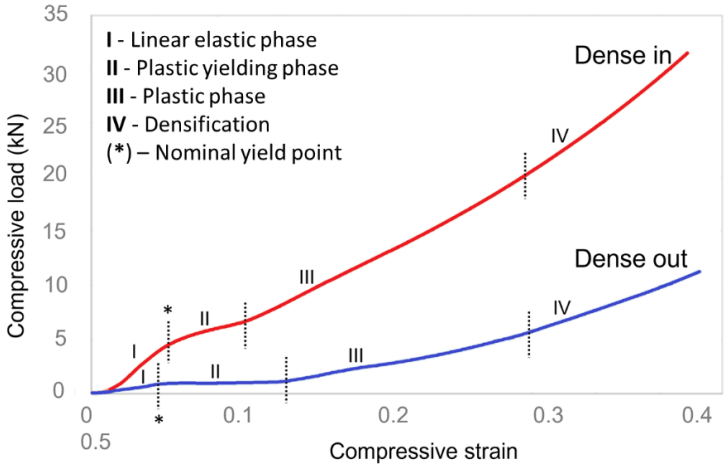

Figure 6.9 - Mechanical compressive performances of dense in (red curve) and dense out (blue curve) graded lattice scaffolds.

Mechanical parameters of scaffolds are listed in Table 6.5. Values of compressive strength at 20% of strain (σ_{20}), ultimate compressive strength (σ_{UC}) and elastic modulus (E) are compared for dense in and dense out graded lattice scaffold in Table 6.5. It is worth noting that the ultimate compression strength of dense out scaffold is very close to the experimental value of cortical bone [1].

Table 6.5 Compressive strength at 20% of strain (σ_{20}), ultimate compressive strength (σ_{UC}) and elastic modulus (E) of dense in and dense out graded lattice scaffold.

Geometry	$\boldsymbol{\sigma_{20}}$ [MPa]		$\boldsymbol{\sigma_{UC}}$ [MPa]		**E** [MPa]	
	AV	SD	AV	SD	AV	SD
Dense-in	115	10	255	15	610	90
Dense-out	20	5	80	6	310	100

SEM observations of scaffolds after mechanical compression test are displayed in Figure 6.10. From micrographs (Figure 6.10), dense in shows the outer layers densified (Figure 6.10a), while dense out the inner ones (Figure 6.10b). Therefore, the predominant failure mechanism of gradient structures initiates in correspondence of the thinnest struts, due to high stress concentrations on the thin strut junctions.

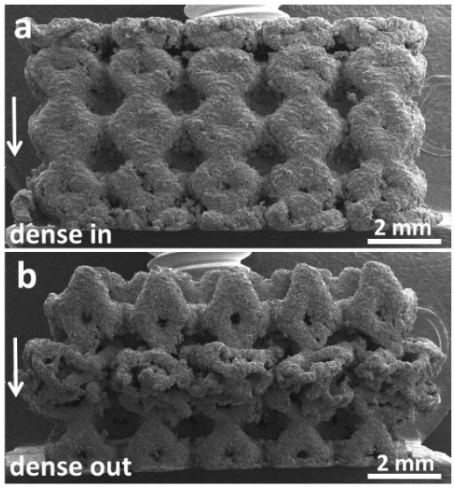

Figure 6.10 - SEM observations of dense in (a) and dense out (b) graded lattice scaffolds after mechanical compression test. Arrows indicate the direction of mechanical uniaxial compressive test.

Biological assessment

The viability of cells seeded on biomaterials and on plastic (tcp) shows no significant differences between structures and tcp after 24h from seeding (Figure 6.11A), while at day 7, an exponential proliferation was assessed with a high degree of viability on 3D scaffolds in comparison with tcp (Figure 6.11A). Moreover, significant differences were detected between structures with the highest metabolically active cells on dense out construct. This promotion could be the effect of a better degree of diffusion of nutrients, as well as the availability of oxygen for the cells, sustained by the inner distribution porosity that characterised dense out geometry.

SEM investigations revealed homogenous cell density across the entire scaffolds surfaces. Cells spread on struts of both structures even after 24h of cultures (Figure 6.11B and D) and, taking advantage from the surfaces rugosity, they accommodated their cell body in the inlets and concavities formed by partially fused particles and extended filipodia to the surrounding area. After 7 days of culture, cells covered both dense in and dense out scaffolds, anchoring and spreading even on the partially melted particles. Cells also started to produce extracellular matrix (ECM) (Figure 6.11C and E).

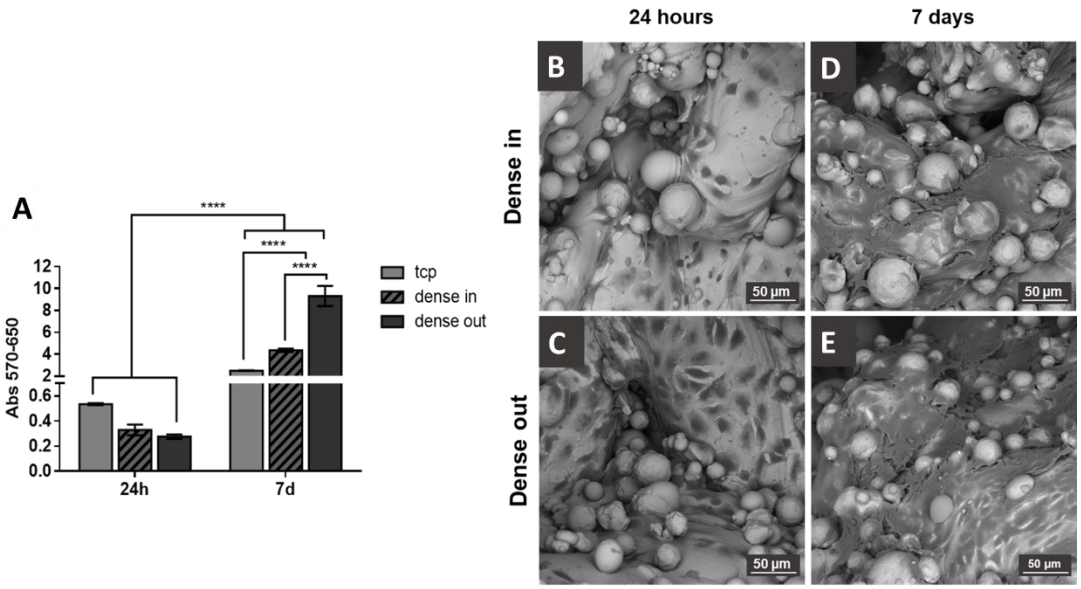

Figure 6.11 - Biological assessment: Viability of cells seeded on dense in and dense out scaffolds was monitored after 24h and 7 days (A) - Data are expressed as Absorbance; SEM observations shows the MG63 morphology and adhesion on dense in and dense out scaffolds after 24 hours (B and C) and 7 days (D and E) from seeding.

Conclusions:

- L-PBF is a suitable technology for the production of graded lattice structure with high accuracy level.
- Preferential plastic deformation of graded lattice scaffolds involves elementary cells with lowest struts thickness, followed by the compaction of scaffold layers in which these cells are arranged, regardless of the scaffold geometry (dense in or dense out). However, only compression behavior of dense out is quite similar to natural bone.
- Short-term viability tests of MG-63 human osteosarcoma cells exhibit production of extracellular matrix in both in dense in and dense out geometry, though metabolically active cells identify dense out as a better biological environment than dense in.

In conclusion, results evidenced that graded lattice geometry allows designing mechanical and biological behavior of scaffold for bone tissue applications. Results showed that best mechanical properties and biological performances were obtained with the dense out geometry.

6.1.2.2. Duplex

Aim: The aim of this experimental work[9] is to compare the *in vitro* behavior of duplex stainless steel with 316L stainless steel graded lattice scaffolds, produce by laser powder bed fusion.

Abstract: The austenitic stainless steels (316L), used for the manufacture of osteosynthesis devices, are sensitive to crevice corrosion, while is well-known that duplex stainless steel (DSS) is not susceptible to crevice corrosion in the human body and can be considered a convenient substitute of ASTM F138 for orthopedic and osteosynthesis devices. Although several articles deal with the use of DSS in orthopedic and orthodontic applications, including *in vitro* and *in vivo* studies, the comparison between austenitic stainless steel and DSS has never been conducted on 3D porous structure (scaffold). In this study, dense out graded lattice geometry produced by laser powder bed fusion (L-PBF) was used to compare biological response *in vitro* of 316L and duplex stainless steel.

State of art: Literature *in vivo* investigation tested the localized corrosion resistance, made of duplex stainless steel (DSS) and of a common austenitic stainless steel, implanted in rabbit femurs for 6 and 12 months. Metallic release and localized corrosion were observed for the specimens made of austenitic stainless steel, but not for those made of DSS [37]. DSS has a superior performance as biomaterial than austenitic stainless steel, with yield and ultimate tensile strengths almost twice than austenitic stainless steel [38]. Thus, in view of considering new alternatives of high performance stainless steels for use as biomaterial, DSS should be a possible alternative, due to their crevice resistances in chloride media and its high mechanical strength, properties that are of great importance for materials to be used for bone implants [38].
As a consequence of the particular balance between chromium and nickel contents, duplex stainless steels have a double phase structure of ferrite (α) and austenite (γ). Generally, DSS contains equal parts of ferrite (body-centered cubic) and austenite (face-centered cubic). The austenitic phase is diamagnetic, and the ferritic phase is magnetic, consequently DSS are partially magnetic [39]. Nonetheless, producing DSS with additive manufacturing technology as laser powder bed fusion (L-PBF), microstructure (phases amount, distribution and grain growth direction) can be controlled by processing parameters [40].
Although several articles deal with the use of DSS in orthopedic and orthodontic applications, including *in vitro* and *in vivo* studies, its use in the biomedical field must still be accepted and the comparison between austenitic stainless steel and DSS has never been conducted on scaffold.

Materials and methods:

- Scaffolds were designed with dense out graded lattice geometry (Figure 6.8).
- Scaffolds were manufactured using duplex stainless steel powder (Mimete Srl) by L-PBF technology with a 3D4steel system (3D4Mec Srl, Sasso Marconi, Italy), using optimized printing parameters.

[9] Paper in preparation.

- Scaffold was characterized by scanning electron microscope (FESEM), energy dispersive spectroscopy (EDS), X-ray diffraction (XRD), mechanical compression test.
- Scaffold biological performances were tested by MG-63 human osteosarcoma cells viability at 24h and 7 days, and cell morphology.

Main results:

Mechanical test

Mechanical behavior under compression of DSS is represented by load-strain curves with similar shape to 316L (Figure 6.9). Although, compressive strength values of DSS at 20% of scaffold strain σ_{20} (during the plastic deformation phase) are about 9 times higher than 316L: $\sigma_{20} = 190 \pm 10$ MPa for DSS and $\sigma_{20} = 20 \pm 5$ MPa for 316L.

Biological test

The cell-materials direct interactions were investigated by viability test (Figure 6.12A) and SEM observations (Figure 6.12B-E). Cells adhered on both 316L and duplex already from 24h after seeding displaying elongated and spread morphology (Figure 6.12B and D, respectively). After 7 days of culture, 316L and duplex samples were completely covered by cells (Figure 6.12C and E, respectively). Some MG63 cells showed elongated morphology as if to create communication bridges between different partially melted particles or between particles and the underlying surface (Figure 6.12C and E). Viability of MG63 increased in time-dependent way on both samples, however, after 7 days of culture, DSS showed a significant ($p<0.001$) greater amount of viable cells than 316L (Figure 6.12A).

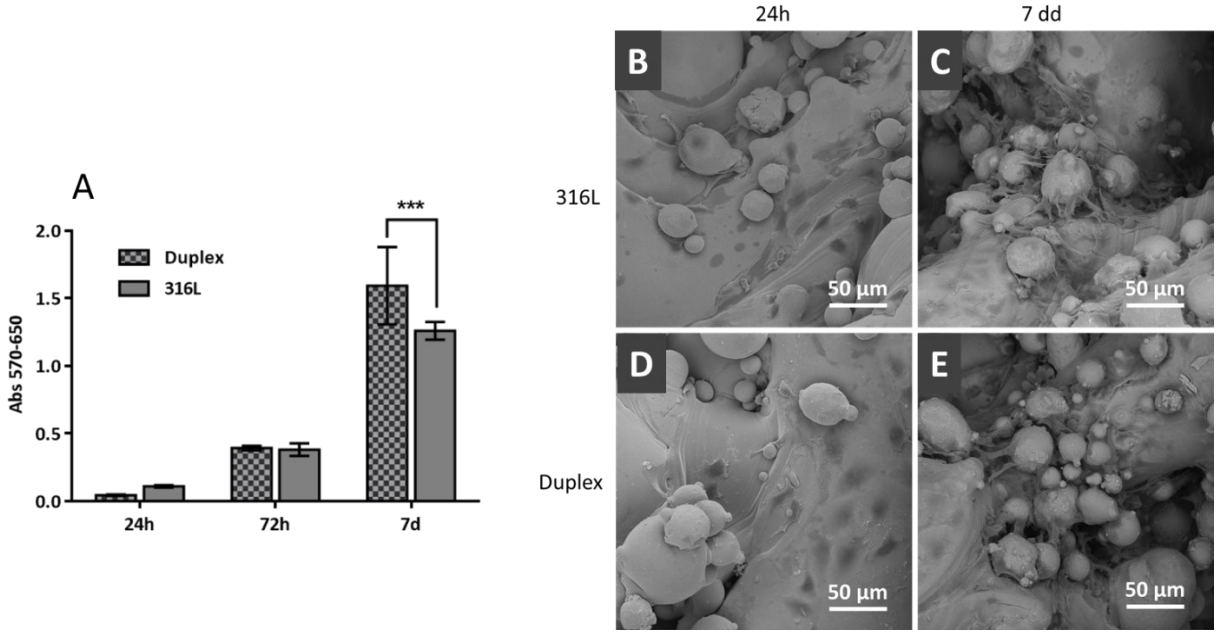

Figure 6.12: Biological assessment of 316L and Duplex scaffolds: Viability of cells incubated for 24 and 72 h (A) - Data are expressed as Absorbance; SEM observations show the MG63 morphology and adhesion on 316L (B and C) and Duplex (D and E) scaffolds after 24 hours and 7 days from seeding.

Conclusions:

- L-PBF technology allows the production of duplex stainless steel (DSS) porous scaffold, maintaining the biocompatibility of material.
- Mechanical response to compressive test of DSS is about a one order of magnitude higher than 316L.
- 316L and duplex scaffold with dense out geometry show a similar biological behavior, suitable for cell adhesion and production of extracellular matrix after 7 days of viability. Moreover, duplex scaffold exhibits a greater amount of viable cells at the end of culture time.

From the above results it is evident that duplex stainless steel show significative higher biomechanical performances *in vitro* than austenitic stainless steel.

6.2. Polymer

6.2.1. DS3000

Aim: The aim of the work[10] is finding the influence of high-definition bone biomimetic geometry produced by vat photopolymerization on biomechanical performances of scaffold, by varying the morphometric parameter of porosity (from 60% to 80%).

Abstract: In this experimental study, high-definition bone-like 3D scaffolds were optimized and produced by Vat Photopolymerization (VPP) in DS3000, a biocompatible resin developed for medical applications, with 60%, 70% and 80% of total porosity. Scaffolds material, 3D structure and mechanical performances were fully characterized. The use of well-known biocompatible material, allowed to investigate the influence of scaffold geometry on short-term cell viability.

State of art: Strategies to improve the formation of a vascular network in engineered bone scaffolds have often been cited as the most significant challenge in creating a device for clinical application. In this context, scaffold architecture plays a pivotal role in the rate and degree of new tissue ingrowth and the control of morphometric parameters could be an interesting strategy to ameliorate vascularity and osteointegration. Bone-like 3D scaffold provides advanced tools to boost the biomimicry properties. A precise spatial control distribution of material can be efficiently obtained by additive manufacturing (AM). Among the various types of additive manufacturing technologies, VPP acquired broad attention from dentistry and bone tissue engineering [41], due to high precision, smooth finishing and low waste material.
DS3000 biocompatible resin, developed for medical applications that require a limited time contact with the body, was used in combination with VPP technology in dentistry application, to created surgical splint and customized impressions, and to reproduce trabecular architecture for *in vitro* model of bone metastasis [42, 43, 44].

Materials and methods:

- Scaffolds were produced using an acrylic acid ester, commercially known as DS300 (DWS), by a DWS 029 vat photopolymerization system (405 nm wavelength);

[10] Paper in preparation.

- Scaffold design was optimized (nTopology software) starting from random lattice structure, based on Voronoi pattern (Figure 6.13).

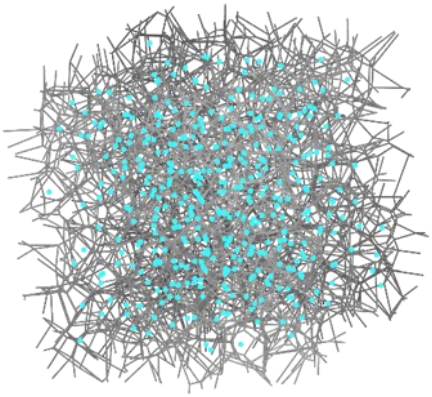

Figure 6.13 - Schematics of the starting points and wire frames of Voronoi pattern.

The strategy to achieve structures with different porosity ($P_{\%}$) is to set the thickness of beams constant and vary the number of pores adapting the structure relative density (RD = 1 – $P_{\%}$). Scaffold with increasing porosity are obtained designing 1) the distance between the points constituting the center of pores of the Voronoi structure and 2) the thickness of the beams. After several interactions necessary to fix these two parameters, respecting the mechanical properties imposed by the bone tissue, different structure with 60% (P60), 70% (P70) and 80% (P80) of porosity were created. To test the pore interconnectivity, the negative model of the scaffold volume with a Voronoi structure is created and meshed, verifying the single component and eventually isolated pores.

- Scaffolds were characterized by scanning electron microscope (SEM), X-ray diffraction (XRD), X-ray micro-computed tomography (XμCT), mechanical compressive test.
- Scaffold biological performances were tested by MG-63 human osteosarcoma cells viability at 24h and 7 days, and cell morphology.

Main results:

Geometry optimization

Results are reported only for scaffold biomimetic geometry with 60% of total porosity (P60). The final space distribution of pores centre are reported in figure 6.14A, with a colour range referring to pore size, while Figure 6.14B and 6.14C show the final pore and material distribution, respectively. The morphometric parameters of P60 are listed in Table 6.6.

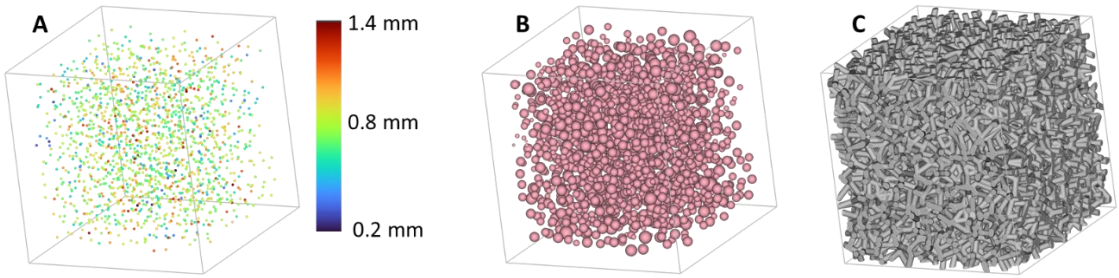

Figure 6.14 - Schematics of scaffold design: final space distribution of pores centre of P60 geometry (A) - Colour bar refers to the scaffold pore size. Final pore and material distribution of P60 (B and C, respectively).

Table 6.6 – Nominal morphometric parameters of scaffold P60.

Parameter	P60
Point spacing [mm]	1.8
Average porosity [mm]	0.8
Total porosity [%]	60
Thickness [mm]	0.6

Mechanical test

Stress-strain curves from compressive test are reported in Figure 6.15A for P60, P70 and P80 DS3000 scaffolds. After the linear phase, the overcoming of yielding point (star in Figure 6.15A) caused the scaffold plastic deformation up to struts breaking, as observable in Figure 6.15B for P60. 2D cross-sectional slices reconstructed from XμCT scan, show various struts fractures (indicated by arrows). Nominal Young modulus (E_{nom}) and nominal ultimate compressive strength (σ_{UC_nom}) are obtained from the stress-strain curves (Table 6.7).

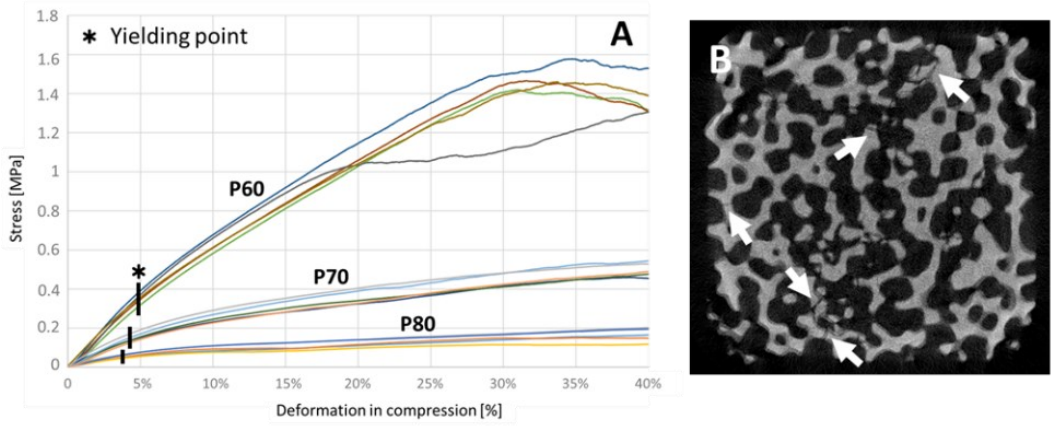

Figure 6.15 – Compression mechanical test on scaffolds: Stress-strain curves of P60, P70 and P80 scaffolds(A) and cross-sectional slice of P60 and arrows indicate fractures in the scaffold struts after the compression tests (B).

Table 6.7 – Mechanical parameters of P60, P70 and P80 from compressive stress-strain curves. E_{nom} - Nominal Young modulus; σ_{UC_nom} - Nominal ultimate compressive strength.

Scaffold geometry	E_{nom} [Mpa]	σ_{UC_nom} [MPa]
P60	8.5 ± 0.6	1.4 ± 0.1
P70	4.0 ± 0.5	0.50 ± 0.03
P80	1.6 ± 0.4	0.17 ± 0.03

XμCT analysis

Morphometric parameters of P60 DS3000 scaffold were quantified pre and post compression test. Morphometric parameters considered are average structure thickness (mm), average structure separation (mm), total porosity (%) and connectivity density (mm^{-3}). Within the experimental error, morphometry of P60 scaffold do not change after reaching 40% of strain in compression.

Then, the plastic deformation of the stress-strain curves in Figure 6.15A is attributable to the failure of oblique struts (Figure 6.15B), which do not directly bear the 3D structure.

Cell viability

Since the mechanical properties of P60 felt within the range of bone, this type of 3D scaffold was selected to conduct cytocompatibility assays. After 24h from seeding, MG63 showed an initial good viability that decreased and remain stable up to 7 days. It must be highlighted that cell diffused inside the scaffold, even in the deepest part, homogeneously. This confirmed that the scaffold 3D structure was able to guarantee the correct perfusion of oxygen and nutrients even in static condition.

The behaviours of cells on 3D scaffold were evaluated at 24h, 72h and 7 days after seeding. MTT assay showed a reduction of MG-63 viability at 72h which remained unchanged after 7 days of culture (Figure 6.16A). The formazan crystals production (identified in purple) was also located in the deepest portion of the scaffolds even at day 7 (Figure 6.16B). SEM analysis revealed that cells colonize the entire scaffold including the inner parts (Figure 6.16C) and spread on the struts assembling several focal adhesions with the material (Figure 6.16D). After 7 days of culture, few groups of cells, with apoptotic features, were detected (Figure 6.16E and Figure 16.6F).

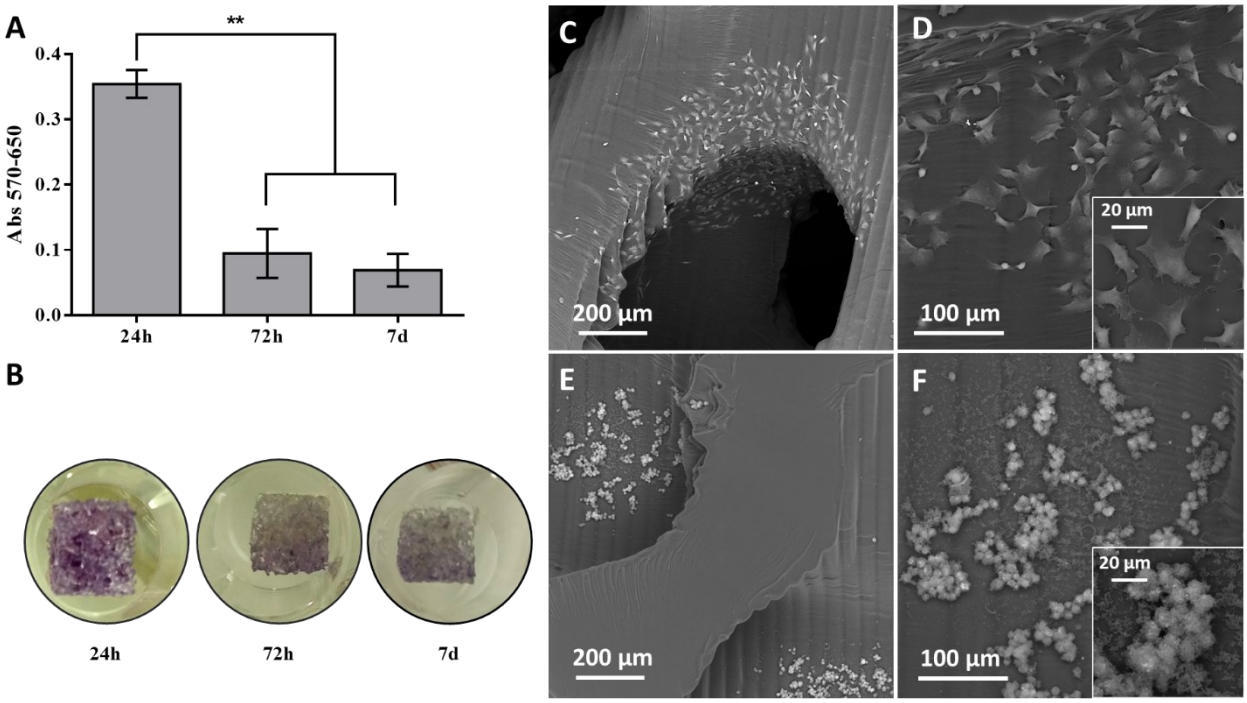

Figure 6.16 - 3D scaffolds cytocompatibility. Fig. A depicts the MG-63 viability at 24, 72h and 7d (data are expressed as abs at 570nm with background subtraction at 650nm); Fig. B shows the localisation of metabolically active cells (purple colour due to the deposition of formazan crystals after MTT incubation) in 3D structures at 24, 72h and 7d; Fig. C - F represent SEM acquisitions of MG-63 on cut 3D scaffolds after 24 h (C and D) and 7 days (E and F) from seeding.

Conclusions:

- Vat Photopolymerization technique is able to manufacture highly-defined biomimetic geometries with high level of porosity.
- The biomimetic bone geometry produced with the DS3000 photopolymer, exhibits brittle behavior under uniaxial compressive strength, while preserving the 3D structure essentially unchanged. Compressive strength values are in the range of maxillofacial applications.
- For short time of culturing the viability is maintained, even if in only 72h the viability drops down significatively. However, after 7 days of incubation, MG-63 cells colonized the inner layers of P60 scaffold. Therefore, bone biomimetic geometry stimulates a suitable biological response of scaffold for tissue engineering applications.

In conclusion, the 3D bone-like scaffold geometry is a promising tool for obtaining structure which encourages cells migration and colonization and, at the same time, support compressive loads up to the rupture without plastic deformation.

6.3. Ceramics

6.3.1. BCP

Aim: This work[11] explored, in an innovative way, the correlations of morphometry, microstructure, mechanical properties, sintering temperature, and time at peak temperature in order to find the best sintering conditions for biphasic calcium phosphate composites grafted in severe alveolar bone defects.

Abstract: Several studies showed that the sintering temperature of 1250 °C could affect the formation of alpha-tricalcium phosphate (α-TCP), which is responsible for the reduction of the hardness value of biphasic calcium phosphate (BCP), grafted in severe alveolar bone defects. However, they did not evaluate the inference of the sintering time at peak temperature on transition of beta-tricalcium phosphate (β-TCP) to α-TCP. This experimental study investigated the best sintering conditions for biphasic calcium phosphate (β-TCP/hydroxyapatite 30 wt.%), by correlating scaffold morphometry, microstructure, mechanical properties, sintering temperature and time at peak temperature. Scaffolds closely mimicked the alveolar organization of the jawbone, independently on the sintering temperatures and times; while mechanical testing revealed that the group with peak temperature, which lasted for 2 hours at 1250 °C, showed the highest compressive strength. The good mechanical performances of this group are most likely due to the absence of the α-TCP phase. However, α-TCP phase presence is detected after sintering at the same peak temperature for longer times, showing the time-dependence, combined with the temperature-dependence, of the β-TCP to α-TCP transition.

State of art: Dental implants were demonstrated to have long survival times, especially in mandibles [46, 47] However, successful implantation can be achieved only when a sufficient jawbone volume is present [47-49]; if diseases, trauma, cysts, or tumors occur, they often produce severe alveolar bone defects, suggesting alveolar ridge augmentation procedures before implantation [48-50].

A well-known potential group of scaffolds comprises bioceramics, which have been successfully used as bone substitute biomaterials in clinical applications for many years, including β-tricalcium phosphate (β-TCP), hydroxyapatite (HA) or their composites called biphasic calcium phosphates (BCPs) [51].

When producing BCPs by sintering, different process regimes allow the modification of scaffold performances in customized ways, once grafted in a patient bone defect. In particular, modulation of sintering temperature was shown to change the BCP biocomposite characteristics (phases formation, porosity and hardness properties) [52].

Materials and methods:

- Scaffold blocks of about 125 mm^3 of volume, were produce by sintering biphasic calcium phosphate (30% of HA and 70% of TCP) powder;
- Sintering production is followed two different protocols: in both of them, the first plateau of temperature reached 800 °C for 2 hours, while in the second plateau, the peak temperatures were

[11] Published paper: [45]

different, namely T =1200 °C and T = 1250 °C. Both peak temperatures samples were sintered for 2, 4, or 8 hours (6 groups of samples);

- Scaffolds were characterized by X-ray micro-computed tomography (XμCT), X-ray diffraction (XRD), mechanical compressive test.

Main results and discussion:

Scaffold morphometry

Morphometric analysis by XμCT showed that in general, all the studied scaffolds closely mimicked the alveolar organization of jawbone (Figure 6.17), having high medullar spaces interconnectivity. Figure 6.17 shows larger pores for samples sintered at T = 1250 °C with respect to those sintered at T = 1200 °C, independently from sintering time at the peak temperature.

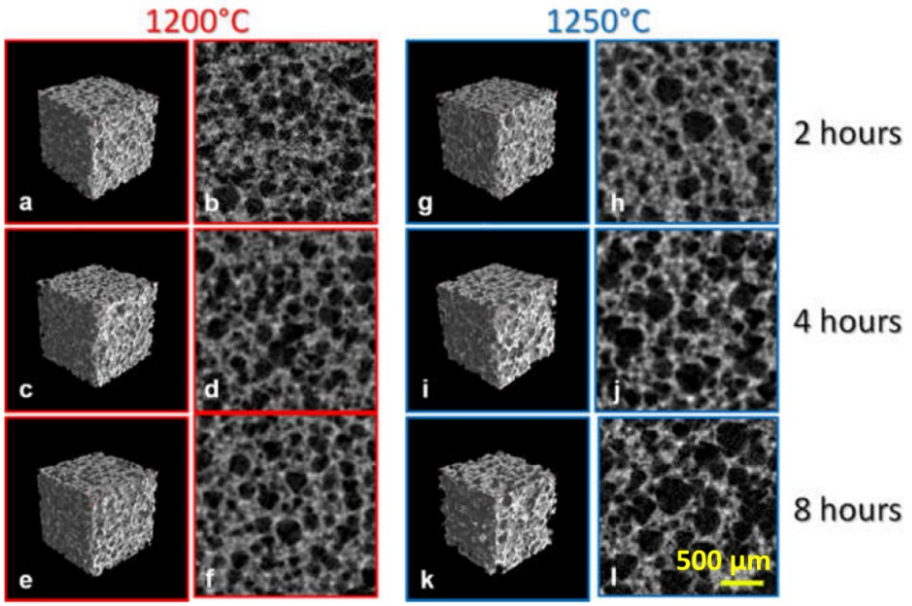

Figure 6.17 - XμCT analysis of the sintered scaffolds: (a–f) Samples sintered at the peak temperature of 1200 °C; (g–l) Samples sintered at the peak temperature of 1250 °C. 3D reconstructions (a, c, e, g, i, k) and axial (b, d, f, j, l) 2D sections of scaffolds: (a, b) T = 1200 °C at 2 h group; (c, d) T = 1200°C at 4 h group; (e, f) T = 1200 °C at 8 h group; (g, h) T = 1250 °C at 2 h group; (i, j) T = 1250 °C at 4 h group; (k, l) T = 1250 °C at 8 h group.

To get reliable information on the microarchitecture, the quantitative morphometric analysis of the complete set of samples was carried out. In 3D mineralized microarchitecture of the scaffolds produced at the peak temperature of 1200 °C, several structural indices remained constant at increasing times of sintering. Conversely, a much wider variability is observed at the peak temperature of 1250 °C, with thinner struts at

increasing times of sintering (Figure 6.18A). Moreover, overall porosity (Figure 6.18B) and pore interconnectivity (Figure 6.18C) decreased for 1200 °C but increased for 1250 °C sintering over time.

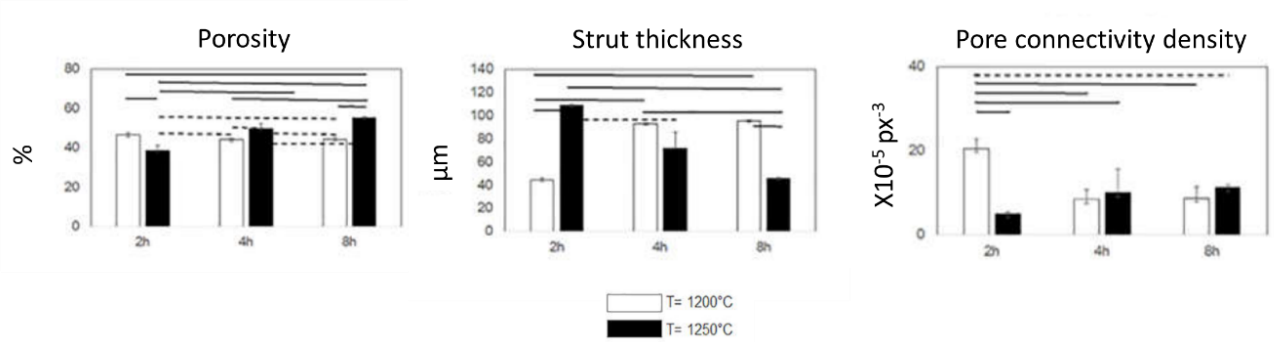

Figure 6.18 - Morphometric 3D data of porosity, strut thickness and pore connectivity density for scaffolds produced at T=1200 °C (with bars) and T=1250 °C (black bars) for 2h, 4h and 8h.

Mechanical characterization

The mechanical testing performed in the present study did not show a relevant variability depending on the time of permanence at the peak temperature for samples of groups at T = 1200 °C; conversely, for groups at T = 1250 °C, yield, ultimate, and fracture stresses seemed to decrease as the duration of the sintering increased. Specifically, the group with peak temperature lasting for 2 hours at 1250 °C showed the highest strength both at the ultimate point and at fracture point. Beyond this critical point, the material changes its mechanical properties. This is most likely due to the α-TCP formation, starting from the group lasting for 4 hours at T = 1250 °C, whose presence is demonstrated by XRD data for sintering at the peak temperature of 1250 °C for longer times than 2 hours.

Good direct correlations were found between the scaffold volume and strength at fracture point and between the strut mean thickness and the strength at the ultimate point. Interestingly, a good inverse correlation was also found between the overall 3D porosity and strength at the fracture point.

Conclusions:

- The BCPs investigated in this study were proved to have a morphometric structure similar to native jawbone, independently of whether they were sintered at different peak temperatures and for different times.
- The BCPs group with peak temperature of 1250 °C for 2 hours showed the highest strength, both at ultimate and at fracture point.
- The ultimate stress achieved by samples that were sintered at the peak temperature above 1200 °C for times longer than 2 hours, was significantly lower, due to allotropic transformation of TCP from β to α phase. In fact, the α phase is brittle and its reverse transformation is not totally achieved during cooling to room temperature.

6.4. Composites

6.4.1. PCL/HA

Aim: The present experimental study[12] aims to extend the know-how on resorbable polycaprolactone/hydroxyapatite (PCL/HA 30 wt.%) bone scaffolds, produced by Laser Powder Bed Fusion (LPBF) technology, to geometrically complex lattice with micro and macro porous structures.

Abstract: Using optimized L-PBF printing parameters, micro- and macro-porous scaffolds for bone tissue regeneration were produced, by regularly repeating in space diamond and rhombic dodecahedron elementary unit cells. After production, scaffolds were submitted to structural, mechanical, biological and matrix-cells interaction characterization. The interaction of scaffolds with human mesenchymal stem cells (hMSCs) allowed studying the degradative processes of the PCL matrix. Biomechanical performances and biodegradation of scaffolds were compared to literature results and bone tissue data. Mechanical compression test, biological viability and degradation rate evidenced strong dependence of scaffold behavior on unit cell geometry.

State of art: Biodegradable scaffolds act as temporary tissue substitutes, providing mechanical support and biological activities during tissue regeneration [54]. High potential production technology of polymer-based scaffolds for bone tissue regeneration was identified in Additive Manufacturing (AM) [55]. Optimization of printing parameters in the L-PBF process allows to improve the dimensional accuracy of parts, thus enabling the production of polymer-based scaffolds with micro- and macro-porous geometry, which meet the requirements for bone regeneration. The main advantages of using the L-PBF technique to produce micro- and macro-porous scaffold are consistency and reproducibility of complex structures [56]. While the CAD design of the elementary unit cell geometry defines the scaffold macro-porosity, the printing parameters used in the L-PBF process totally determine the micro-porosity of the scaffold [56].

Regarding scaffold macro-porosity, recent simulation studies on unit cell topology [5, 6] concluded that midline-symmetrical elementary unit cell geometry, such as Rhombic Dodecahedron (RD), is suitable for load-bearing implants that support the body weight directly, with high mass transfer performance. On the other hand, diagonal-symmetrical elementary unit cell, such as Diamond (DO), has been proposed as the best choice for implants that require large torsional forces, with advantages on implant fixation, cell growth environment and tissue regeneration [5, 6]. The appropriate design of elementary unit cell topology allows controlling strut thickness, which determines the size of macro-pores (> 100 μm) [56], which in turn influences both mechanical and biological performances. On the other hand, small pores (40–100 μm) inside struts constitute the scaffold micro-porosity [56] which increases the specific surface of the material, thus improving permeability, enhancing scaffold degradation and increasing the number of sites available for protein absorption, that improve cells adhesion, proliferation, differentiation and mineralization [57, 58].

[12] Published paper: [53]

The combination of PCL and HA meets biological and mechanical requests for scaffold applications in bone tissue regeneration. Systematic studies in the literature have demonstrated that the quantity of HA capable of enhancing both cell proliferation and mechanical behavior of PCL/HA mixture is about 30 wt.% [59]. Despite the large number of papers dealing with this topic, studies combining L-PBF and PCL/HA (30 wt.%) for scaffold production in perspective of bone tissue regeneration have limited to investigate very simple scaffold geometries, such as solid discs with porous network due to spaces between particles [60], cubic reticular structures [59, 61, 62] and cylinders with orthogonal square channels [63].

Materials and methods:

- Scaffolds were produced using a mixture containing 70 wt.% polycaprolactone (PCL) and 30 wt.% hydroxyapatite (HA);
- Scaffolds were additively manufactured by laser powder bed fusion (L-PBF) technology, using an EOS P770 system;
- Scaffolds were designed (Magics 21.0) with diamond (DO) and rhombic dodecahedron (RD) elementary unit cell (Figure 6.1). Scaffold volume corresponds to a cube 1 cm side length, nominal porosity is 80% and strut size 420 μm for DO and 460 μm for RD (CAD values). Furthermore, scaffolds were produced with intrinsic micro-porosity in the struts, optimizing machining parameters.
- Scaffolds were characterized by scanning electron microscope (SEM), energy dispersive spectroscopy (EDS), X-ray diffraction (XRD), X-ray micro-computed tomography (XμCT) and phase-contrast X-ray micro-computed tomography (PhC-XμCT), roughness measurements and mechanical compressive test.
- Scaffold biological performances were tested by hMSCs viability at 24h and 4 days and cell morphology.

Main results and discussion:

XμCT analysis

DO and RD scaffold geometries show similar mean strut thickness (Table 6.8) and porosity (Table 6.10). Discrepancies between CAD and experimental values of strut thickness (Table 6.8) and porosity (Table 6.10) are fully due to the LPBF manufacturing technique. In the measured value of scaffold porosity is included micro-porosity formed inside struts during the production process. Micro-porosity amounts to about 8%, with average size of micro-pores below 100 μm, independently on unit cell geometry (DO or RD), as estimated by XμCT analysis (Table 6.8). In quantitative terms, the RD geometry has macro-pores with experimentally estimated average size doubled with respect to DO (Table 6.8). From this result, it can be concluded that scaffold based on the RD geometry is formed of few large-size macro-pores, while DO shows many small-size macro-pores. Therefore, the RD geometry, which has less connected structures, shows lower tortuosity and higher porosity than DO.

Table 6.8 - Scaffolds morphometric parameters obtained from XμCT analysis.

Parameter	DO	RD
Mean strut thickness [mm]	0.80 ± 0.12	0.83 ± 0.13
Mean macro pore size [mm]	0.80 ± 0.18	1.60 ± 0.18
Mean micro pore size [μm]	65 ± 10	60 ± 25
Scaffold micro-porosity [%]	8 ± 2%	8 ± 4%

Scaffold characterization

The elementary unit cell geometry influences scaffold global performances as well as local properties. For instance, local heat dissipation during the production process is strongly dependent on scaffold geometry. Tortuosity affects heat dissipation during scaffold fabrication, thus resulting in slower heat dissipation rate for DO (high tortuosity) rather than RD. Heat dissipation rate also affects surface roughness. In DO geometry the heat dissipation rate is low (higher tortuosity), resulting in a longer cooling time which facilitates partial melting of the larger and denser PCL particles on the scaffold surface. The related consequence of this, is a slightly higher surface roughness of DO than RD. On the other hand, heat dissipation rate strongly affects material crystallinity during solidification and cooling. XRD patterns of the scaffold top surface are reported in Figure 6.19. XRD pattern of the mixed raw powder is also reported in Figure 6.19 as reference. PCL peaks are indicated by full dots. Patterns are shifted vertically to ease comparison. Peak shape analysis of XRD patterns provided exact angular position (2θ) and full width at half maximum (FWHM) of most intense peaks. In particular, the two most intense peaks of PCL and the four peaks of HA in the range 2θ = 30–35° were considered, and results are shown in Table 6.9. Miller indices (hkl) in Table 6.9 are reported considering the PCL orthorhombic crystallographic structure proposed by Bittiger et al., while HA structure was taken from ICDD file n. 74–565. Comparison of patterns in Figure 6.19 and results of peak shape analysis in Table 6.9 clearly show a general trend to reduced intensity and increased width (FWHM) of diffraction peaks in scaffolds. This suggests a less crystallized structure of both PCL and HA in scaffolds with respect to the raw powder. It is worth to note that crystallinity of PCL and HA depended on unit cell topology, with DO showing higher crystallinity of both phases (PCL and HA) against RD. As for peak angular position, XRD patterns of scaffolds showed a general shift to lower values with respect to raw powder, indicating higher values of lattice parameters of compounds (PCL and HA) in scaffolds (Table 6.9).

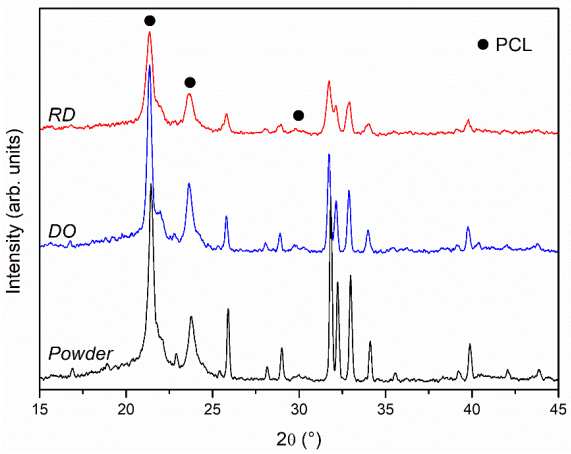

Figure 6.19 - XRD patterns of the scaffolds top surface. Pattern of the mixed raw powder is reported for comparison. PCL – full dots.

Table 6.9 - Results of peak shape analysis carried out on most intense XRD peaks of PCL and HA for raw powder and scaffolds with DO and RD elementary unit cell geometry. 2θ - Angular position; FWHM - Full width at half maximum, hkl Miller indices. Angular position 2θ and FWHM in degree (°).

Material	**Powder**		**Elementary unit cell geometry**				**hkl**
			DO		**RD**		
	2θ (°)	*FWHM (°)*	*2θ (°)*	*FWHM (°)*	*2θ (°)*	*FWHM (°)*	
PCL	21.445±0.003	0.351±0.008	21.355±0.001	0.282±0.004	21.355±0.001	0.430±0.005	(110)
	23.792±0.008	0.41±0.03	23.658±0.002	0.414±0.008	23.664±0.003	0.51±0.01	(200)
HA	31.836±0.001	0.143±0.004	31.733±0.001	0.175±0.004	31.731±0.002	0.322±0.007	(211)
	32.238±0.002	0.128±0.007	32.141±0.002	0.151±0.008	32.133±0.004	0.21±0.01	(112)
	32.983±0.002	0.155±0.007	32.886±0.002	0.175±0.006	32.878±0.003	0.278±0.008	(300)
	34.115±0.006	0.18±0.02	33.992±0.007	0.24±0.02	33.998±0.009	0.41±0.03	(202)

Mechanical test

The compressive tests carried out on the two scaffold geometries (DO and RD) show a substantial identical behavior in the elastic regime (same curve shape and elastic modulus value, Figure 6.20 and Table 6.10), where the elastic properties of the material as well as the elementary unit cell geometry mainly control the mechanical response. In the elastic region, the geometry contribution is due to the elastic response of struts, where pores are not yet flattened and broken, as gradually occurs during plastic collapse [61, 63]. Similar values of strut thickness (ST) and relative density (ρ) in Table 6.10 for DO and RD geometries confirm this mechanism. In the region of plastic deformation (Figure 6.20) struts of the elementary unit cells progressively collapse under the applied load. In this region, DO requires 30% higher load to reach the same compaction value of RD

(Figure 6.20). This effect is due to smaller macro-pores of DO than RD (Table 6.10) at constant strut thickness, resulting in a more connected and space-opened channels. Therefore, the elementary unit cell geometry (connectivity and tortuosity) mainly governs the mechanical behavior during the plastic collapse of scaffold. Collapse of the scaffold structure continues up to compaction, where the compressive curve shows similar behavior for the two geometries (DO and RD). Values of ultimate compressive strength in Table 6.10 are equal, within experimental uncertainties, independently on elementary unit cell geometry. This latter result shows that, at compaction, when the whole scaffold structure is collapsed and pores flattened, the mechanical response mainly depends on material properties.

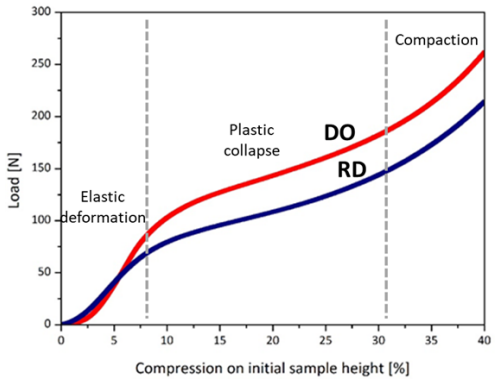

Figure 6.20 - Results of the compression tests for DO (red curve) and RD (blue curve) scaffolds.

Considering that the density of struts (ρs) of our scaffolds is in the range of human mandibular trabecular bone (Table 6.10), comparison of mechanical performances of scaffolds to native bone is allowed. The mechanical parameter considered in this case is the ultimate compressive strength (Table 6.10). Experimental results clearly show that both DO and RD scaffolds geometries perfectly match with the range of values of the ultimate compressive strength of middle region of human mandibular trabecular bone in absence of cortical plates [64].

Table 6.10 - Results obtained in this work for DO and RD geometries compared to literature data for PCL/HA (30 wt.%) scaffolds manufactured by LPBF and human mandibular trabecular bone in absence of cortical plates. P – porosity; PS – average pore size; ST – average strut thickness; ρ - relative density; ρ_s – density of strut; E - elastic modulus; σ_{UC} – ultimate compressive strength.

Reference	**P (%)**		**PS (mm)**		**ST (mm)**		**ρ**		**ρ_s (g/cm^3)**		**E (MPa)**		**σ_{UC} (MPa)**	
This work	*DO*	*RD*	*DO*	*RD*	*DO*	*RD*	*DO*	*RD*	*DO*	*RD*	*DO*	*RD*	*DO*	*RD*
	53	59	0.8	1.6	0.8	0.8	0.47	0.41	0.83	0.72	15±4	13±4	2.8±0.5	2.6±0.4
S. Eosoly et al., 2009, 2010, 2012 [59, 61, 62]	67		1.2		0.6		0.33		-		1 ÷ 2		0.2 ÷ 0.6	
S. Eshraghi et al., 2012 [63]	81		2		0.7		0.19		-		36 ± 1		0.9 ± 0.3	
Human mandibular trabecular bone [64]	-		-		-		-		0.85 ÷ 1.53		3.5 ÷ 125.6		0.22 ÷ 10.44	

Cell adhesion and proliferation

Biological performances of scaffolds, tested with short-term hMSCs viability, consist of DO and RD ability to provide a support for cell adhesion and proliferation (Figure 6.21). Furthermore, DO and RD scaffold geometries allow cell migration from surface (Figure 6.21) to the inner scaffold layers, as confirmed by absence of hMSCs detected by SEM on the top surface of DO and RD scaffolds after 4 days of incubation. In particular, the hMSCs viability trend is greater in RD scaffold geometry respect to DO, due to higher pores size and porosity and lower connectivity and tortuosity, which make cells able to colonize the whole structure with the appropriate supply of nutrients and oxygen.

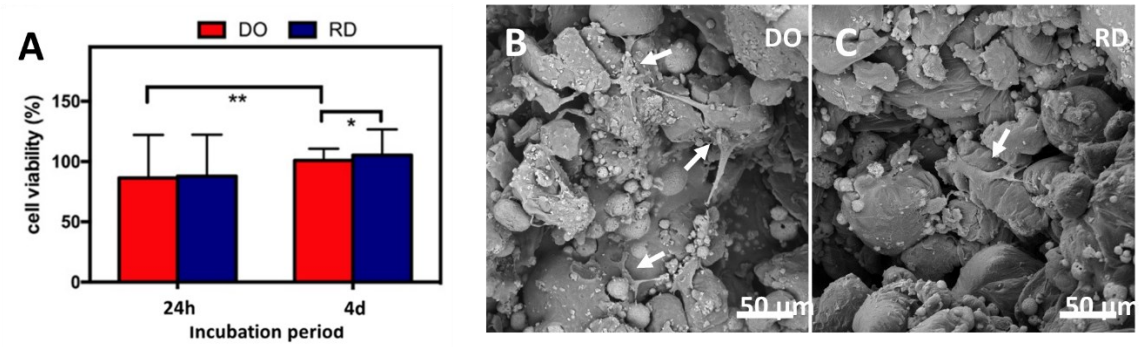

*Figure 6.21 - hMSCS viability after 24 h (24 h) and 4 days (4d) incubation for DO and RD scaffold geometries - * $p < 0.05$; ** $p < 0.01$ (A). SEM observations of hMSCs after 24 h of incubation: DO (A) and RD (B) scaffolds. Arrows indicated hMSCs.*

PhC-XµCT analysis

Under physiological conditions of cell culture, three factors mainly influence PCL degradation: a) geometrical features of the sample, b) PCL raw powder molecular weight and c) local environment characteristics as fluid flow, temperature, and pH [65]. An additional factor reported in literature, capable of affecting PCL degradation, is incorporation of ceramic compounds such as hydroxyapatite [65]. In the present study, all these effects are present and cooperate to the scaffold degradation. High porosity level and large pores size (Table 6.10) enable fluid infiltration into the structure [65]. In addition, scaffold micro porosity within struts is a factor that accelerates the material degradative process, allowing fluid infiltration also inside the struts [66]. Variability of the PCL molecular weight in the raw powder, allowed more likely the release of short chains by the bulk, anticipating mass loss from the matrix [65]. Local environment is characterized by the cells incubation conditions and DMEM flow, affected by scaffold tortuosity. According to Bartnikowski et al. [65], in *in vitro* environment, degradation is faster in the presence of cells (cell-containing environment) [65].
Furthermore, addition of HA particles accelerates the degradation of PCL, due to preferred attack at the ceramic/polymer interface by water with consequent weight loss, followed by macroscopic structural breakdown and small polymer fragments metabolized by cells [67].

PhC-XμCT results on our scaffolds after 24 h of incubation, evidenced PCL degradation in scaffolds due to the combined effects of elementary unit cell geometry, PCL molecular weight, culture medium, presence of cells, as well as amount and size of crystalline HA. Further confirmation of the interaction between stem cells and biomaterial is the strong increase of material specific surface in the scaffold nodes, from 24 h to 4 days of culture. This increase is due to material disintegration with the resulting pores filled with the eroded material from struts around the macro-pores, as illustrated in Figure 6.22.

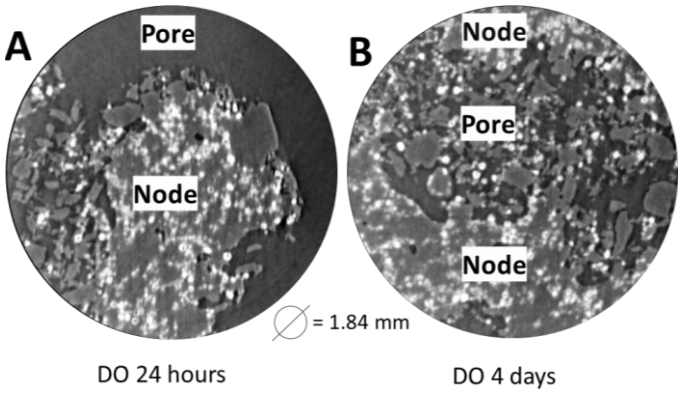

Figure 6.22 – Nodes and Pores imaging by PhC-XμCT reconstruction of DO after 24 hours (A) and DO after 4 days (B) of incubation.

Conclusions:

- Scaffold total porosity (micro and macro) is higher than 50% for the investigated geometries (DO and RD), with micro-porosity amounting to about 8% in the two cases;
- Different geometry of the elementary unit cell reflects on connectivity and tortuosity of macro-pores in the scaffolds. The RD geometry shows lower tortuosity with larger macro-pores than DO;
- Surface roughness and crystallinity of scaffolds is influenced from the thermal behavior on heating of PCL and HA. Heat dissipation rate during cooling mainly depends on scaffold tortuosity, thus resulting in higher surface roughness and crystallinity value for DO than RD;
- Mechanical response of scaffolds submitted to compressive tests evidenced three distinct regions: a) the elastic regime governed by elementary unit cell geometry and material properties, b) the plastic deformation behavior due to the macroscopic geometrical properties (connectivity and tortuosity) of scaffolds, and c) the compaction region, where the material properties determine the mechanical response;
- The ultimate compressive strength values of both DO and RD geometries match with the range of values of the middle region of human mandibular trabecular bone in absence of cortical plates;
- Although the biological response is acceptable for both geometries (DO and RD), RD provides a better 3D environment for hMSCs adhesion and proliferation for scaffold colonization;
- The presence of micro-pores within the struts enhances the scaffold degradation.

Results obtained in this study evidenced the suitability of PCL/HA (30 wt%) resorbable lattice scaffolds with DO and RD elementary unit cell geometry as temporary supports for bone tissue regeneration of human mandibular trabecular bone regeneration.

References

[1] Gatto, M. L., Groppo, R., Bloise, N., Fassina, L., Visai, L., Galati, M., ... & Mengucci, P. (2021). Topological, mechanical and biological properties of Ti6Al4V scaffolds for bone tissue regeneration fabricated with reused powders via electron beam melting. Materials, 14(1), 224.

[2] Wu, S., Liu, X., Yeung, K. W., Liu, C., & Yang, X. (2014). Biomimetic porous scaffolds for bone tissue engineering. Materials Science and Engineering: R: Reports, 80, 1-36.

[3] Wang, X., Xu, S., Zhou, S., Xu, W., Leary, M., Choong, P., ... & Xie, Y. M. (2016). Topological design and additive manufacturing of porous metals for bone scaffolds and orthopaedic implants: A review. Biomaterials, 83, 127-141.

[4] Wubneh, A., Tsekoura, E. K., Ayranci, C., & Uludağ, H. (2018). Current state of fabrication technologies and materials for bone tissue engineering. Acta Biomaterialia, 80, 1-30.

[5] Li, J., Chen, D., Zhang, Y., Yao, Y., Mo, Z., Wang, L., & Fan, Y. (2019). Diagonal-symmetrical and midline-symmetrical unit cells with same porosity for bone implant: Mechanical properties evaluation. Journal of Bionic Engineering, 16(3), 468-479.

[6] Li, J., Chen, D., & Fan, Y. (2019). Evaluation and prediction of mass transport properties for porous implant with different unit cells: a numerical study. BioMed Research International, 2019.

[7] Popov, V. V., Muller-Kamskii, G., Kovalevsky, A., Dzhenzhera, G., Strokin, E., Kolomiets, A., & Ramon, J. (2018). Design and 3D-printing of titanium bone implants: brief review of approach and clinical cases. Biomedical engineering letters, 8(4), 337-344.

[8] Calignano, F., Galati, M., Iuliano, L., & Minetola, P. (2019). Design of additively manufactured structures for biomedical applications: a review of the additive manufacturing processes applied to the biomedical sector. Journal of healthcare engineering, 2019.

[9] Martinez-Marquez, D., Mirnajafizadeh, A., Carty, C. P., & Stewart, R. A. (2018). Application of quality by design for 3D printed bone prostheses and scaffolds. PloS one, 13(4), e0195291.

[10] Powell, D., Rennie, A. E., Geekie, L., & Burns, N. (2020). Understanding powder degradation in metal additive manufacturing to allow the upcycling of recycled powders. Journal of Cleaner Production, 268, 122077.

[11] Chandrasekar, S., Coble, J. B., Yoder, S., Nandwana, P., Dehoff, R. R., Paquit, V. C., & Babu, S. S. (2020). Investigating the effect of metal powder recycling in Electron beam Powder Bed Fusion using process log data. Additive Manufacturing, 32, 100994.

[12] Tang, H. P., Qian, M., Liu, N., Zhang, X. Z., Yang, G. Y., & Wang, J. (2015). Effect of powder reuse times on additive manufacturing of Ti-6Al-4V by selective electron beam melting. Jom, 67(3), 555-563.

[13] Yusoff, M. F. M., Kadir, M. R. A., Iqbal, N., Hassan, M. A., & Hussain, R. (2014). Dipcoating of poly (ε-caprolactone)/hydroxyapatite composite coating on Ti6Al4V for enhanced corrosion protection. Surface and Coatings Technology, 245, 102-107.

[14] Tolochko, N. K., Arshinov, M. K., Gusarov, A. V., Titov, V. I., Laoui, T., & Froyen, L. (2003). Mechanisms of selective laser sintering and heat transfer in Ti powder. Rapid prototyping journal.

[15] Zhou, D., Gao, Y., Lai, M., Li, H., Yuan, B., & Zhu, M. (2015). Fabrication of NiTi shape memory alloys with graded porosity to imitate human long-bone structure. Journal of Bionic Engineering, 12(4), 575-582.
[16] Ahmadi, S. M., Yavari, S. A., Wauthle, R., Pouran, B., Schrooten, J., Weinans, H., & Zadpoor, A. A. (2015). Additively manufactured open-cell porous biomaterials made from six different space-filling unit cells: The mechanical and morphological properties. Materials, 8(4), 1871-1896.
[17] Del Guercio, G., Galati, M., & Saboori, A. (2021). Innovative approach to evaluate the mechanical performance of Ti–6Al–4V lattice structures produced by electron beam melting process. Metals and Materials International, 27(1), 55-67.
[18] Xia, L., Xie, Y., Fang, B., Wang, X., & Lin, K. (2018). In situ modulation of crystallinity and nano-structures to enhance the stability and osseointegration of hydroxyapatite coatings on Ti-6Al-4V implants. Chemical Engineering Journal, 347, 711-720.
[19] Rivera-Denizard, O., Diffoot-Carlo, N., Navas, V., & Sundaram, P. A. (2008). Biocompatibility studies of human fetal osteoblast cells cultured on gamma titanium aluminide. Journal of Materials Science: Materials in Medicine, 19(1), 153-158.
[20] Castañeda-Muñoz, D. F., Sundaram, P. A., & Ramírez, N. (2007). Bone tissue reaction to Ti–48Al–2Cr–2Nb (at.%) in a rodent model: a preliminary SEM study. Journal of Materials Science: Materials in Medicine, 18(7), 1433-1438.

[21] Kyzioł, K., Kaczmarek, Ł., Brzezinka, G., & Kyzioł, A. (2014). Structure, characterization and cytotoxicity study on plasma surface modified Ti–6Al–4V and γ-TiAl alloys. Chemical Engineering Journal, 240, 516-526.

[22] Escudero, M. L., Munoz-Morris, M. A., Garcıa-Alonso, M. C., & Fernández-Escalante, E. (2004). In vitro evaluation of a γ-TiAl intermetallic for potential endoprothesic applications. Intermetallics, 12(3), 253-260.

[23] Mohammad, A., Al-Ahmari, A. M., Balla, V. K., Das, M., Datta, S., Yadav, D., & Ram, G. J. (2017). In vitro wear, corrosion and biocompatibility of electron beam melted γ-TiAl. Materials & Design, 133, 186-194.

[24] Som, I., Balla, V. K., Das, M., & Sukul, D. (2018). Thermally oxidized electron beam melted γ-TiAl: In vitro wear, corrosion, and biocompatibility properties. Journal of Materials Research, 33(14), 2096-2105.

[25] Dzogbewu, T. C. (2020). Additive manufacturing of TiAl-based alloys. Manufacturing Review, 7, 35.

[26] Emiralioğlu, A., & Ünal, R. (2022). Additive manufacturing of gamma titanium aluminide alloys: a review. Journal of Materials Science, 1-26.

[27] Al-Mamun, N. S., Deen, K. M., Haider, W., Asselin, E., & Shabib, I. (2020). Corrosion behavior and biocompatibility of additively manufactured 316L stainless steel in a physiological environment: The effect of citrate ions. Additive Manufacturing, 34, 101237.

[28] Kong, D., Ni, X., Dong, C., Lei, X., Zhang, L., Man, C., ... & Li, X. (2018). Bio-functional and anti-corrosive 3D printing 316L stainless steel fabricated by selective laser melting. Materials & Design, 152, 88-101.

[29] Bai, L., Gong, C., Chen, X., Sun, Y., Zhang, J., Cai, L., ... & Xie, S. Q. (2019). Additive manufacturing of customized metallic orthopedic implants: Materials, structures, and surface modifications. Metals, 9(9), 1004.

[30] Al-Ketan, O. (2021). Programmed Plastic Deformation in Mathematically-Designed Architected Cellular Materials. Metals, 11(10), 1622.

[31] Zhong, T., He, K., Li, H., & Yang, L. (2019). Mechanical properties of lightweight 316L stainless steel lattice structures fabricated by selective laser melting. Materials & Design, 181, 108076.

[32] Ma, S., Tang, Q., Feng, Q., Song, J., Han, X., & Guo, F. (2019). Mechanical behaviours and mass transport properties of bone-mimicking scaffolds consisted of gyroid structures manufactured using selective laser melting. Journal of the mechanical behavior of biomedical materials, 93, 158-169.

[33] Čapek, J., Machová, M., Fousová, M., Kubásek, J., Vojtěch, D., Fojt, J., ... & Ruml, T. (2016). Highly porous, low elastic modulus 316L stainless steel scaffold prepared by selective laser melting. Materials Science and Engineering: C, 69, 631-639.

[34] Fousová, M., Kubásek, J., Vojtěch, D., Fojt, J., & Čapek, J. (2017, February). 3D printed porous stainless steel for potential use in medicine. In IOP Conference Series: Materials Science and Engineering (Vol. 179, No. 1, p. 012025). IOP Publishing.

[35] Xiao, Z., Yang, Y., Xiao, R., Bai, Y., Song, C., & Wang, D. (2018). Evaluation of topology-optimized lattice structures manufactured via selective laser melting. Materials & Design, 143, 27-37.

[36] Cao, X., Duan, S., Liang, J., Wen, W., & Fang, D. (2018). Mechanical properties of an improved 3D-printed rhombic dodecahedron stainless steel lattice structure of variable cross section. International Journal of Mechanical Sciences, 145, 53-63.

[37] Cigada, A., Santis, G. D., Gatti, A. M., Roos, A., & Zaffe, D. (1993). In vivo behavior of a high performance duplex stainless steel. Journal of Applied Biomaterials, 4(1), 39-46.

[38] Gregorutti, R. W., Grau, J. E., Sives, F., & Elsner, C. I. (2015). Mechanical, electrochemical and magnetic behaviour of duplex stainless steel for biomedical applications. Materials Science and Technology, 31(15), 1818-1824.

[39] Hammood, A. S. (2020). Biomineralization of 2304 duplex stainless steel with surface modification by electrophoretic deposition. Journal of Applied Biomaterials & Functional Materials, 18, 2280800019896215.

[40] Zhang, D., Liu, A., Yin, B., & Wen, P. (2022). Additive manufacturing of duplex stainless steels-A critical review. Journal of Manufacturing Processes, 73, 496-517.

[41] Zhang, F., Zhu, L., Li, Z., Wang, S., Shi, J., Tang, W., Li, N., & Yang, J. (2021). The recent development of vat photopolymerization: A review. Additive Manufacturing, 48, 102423.

[42] Barone, M., De Stefani, A., Baciliero, U., Bruno, G., & Gracco, A. (2020). The Accuracy of Jaws Repositioning in Bimaxillary Orthognathic Surgery with Traditional Surgical Planning Compared to Digital Surgical Planning in Skeletal Class III Patients: A Retrospective Observational Study. Journal of clinical medicine, 9(6), 1840.

[43] Mangano, F. G., Margiani, B., Solop, I., Latuta, N., & Admakin, O. (2020). An Experimental Strategy for Capturing the Margins of Prepared Single Teeth with an Intraoral Scanner: A Prospective Clinical Study on 30 Patients. International journal of environmental research and public health, 17(2), 392.

[44] Han, W., El Botty, R., Montaudon, E., Malaquin, L., Deschaseaux, F., Espagnolle, N., Marangoni, E., Cottu, P., Zalcman, G., Parrini, M. C., Assayag, F., Sensebe, L., Silberzan, P., Vincent-Salomon, A., Dutertre, G., Roman-Roman, S., Descroix, S., & Camonis, J. (2021). In vitro bone metastasis dwelling in a 3D bioengineered niche. Biomaterials, 269, 120624.

[45] Giuliani, A., Gatto, M. L., Gobbi, L., Mangano, F. G., & Mangano, C. (2020). Integrated 3D information for custom-made bone grafts: focus on biphasic calcium phosphate bone substitute biomaterials. International Journal of Environmental Research and Public Health, 17(14), 4931.

[46] Mangano, F., Macchi, A., Caprioglio, A., Sammons, R. L., Piattelli, A., & Mangano, C. (2014). Survival and complication rates of fixed restorations supported by locking-taper implants: a prospective study with 1 to 10 years of follow-up. Journal of Prosthodontics, 23(6), 434-444.

[47] Mangano, F., Shibli, J. A., Sammons, R. L., Veronesi, G., Piattelli, A., & Mangano, C. (2014). Clinical outcome of narrow-diameter (3.3-mm) locking-taper implants: a prospective study with 1 to 10 years of follow-up. International Journal of Oral & Maxillofacial Implants, 29(2).

[48] Tamimi, F., Torres, J., Al-Abedalla, K., Lopez-Cabarcos, E., Alkhraisat, M. H., Bassett, D. C., ... & Barralet, J. E. (2014). Osseointegration of dental implants in 3D-printed synthetic onlay grafts customized according to bone metabolic activity in recipient site. Biomaterials, 35(21), 5436-5445.

[49] Jacotti, M., Barausse, C., & Felice, P. (2014). Posterior atrophic mandible rehabilitation with onlay allograft created with CAD-CAM procedure: a case report. Implant dentistry, 23(1), 22-28.

[50] Esposito, M., Grusovin, M. G., Felice, P., Karatzopoulos, G., Worthington, H. V., & Coulthard, P. (2010). The efficacy of horizontal and vertical bone augmentation procedures for dental implants: A Cochrane systematic review. Evidence-based practice: Toward optimizing clinical outcomes, 195-218.

[51] Dorozhkin, S. V. (2010). Calcium orthophosphate bioceramics. In Journal of Biomimetics, Biomaterials and Tissue Engineering (Vol. 5, pp. 57-100). Trans Tech Publications Ltd.

[52] Brown, O., McAfee, M., Clarke, S., & Buchanan, F. (2010). Sintering of biphasic calcium phosphates. Journal of Materials Science: Materials in Medicine, 21(8), 2271-2279.

[53] Gatto, M. L., Furlani, M., Giuliani, A., Bloise, N., Fassina, L., Visai, L., & Mengucci, P. (2021). Biomechanical performances of PCL/HA micro-and macro-porous lattice scaffolds fabricated via laser powder bed fusion for bone tissue engineering. Materials Science and Engineering: C, 128, 112300.

[54] Prakasam, M., Locs, J., Salma-Ancane, K., Loca, D., Largeteau, A., & Berzina-Cimdina, L. (2017). Biodegradable materials and metallic implants—a review. Journal of functional biomaterials, 8(4), 44.

[55] Szymczyk-Ziółkowska, P., Łabowska, M. B., Detyna, J., Michalak, I., & Gruber, P. (2020). A review of fabrication polymer scaffolds for biomedical applications using additive manufacturing techniques. Biocybernetics and Biomedical Engineering, 40(2), 624-638.

[56] Yeong, W. Y., Sudarmadji, N., Yu, H. Y., Chua, C. K., Leong, K. F., Venkatraman, S. S., ... & Tan, L. P. (2010). Porous polycaprolactone scaffold for cardiac tissue engineering fabricated by selective laser sintering. Acta biomaterialia, 6(6), 2028-2034.

[57] Zhang, K., Fan, Y., Dunne, N., & Li, X. (2018). Effect of microporosity on scaffolds for bone tissue engineering. Regenerative biomaterials, 5(2), 115-124.

[58] Abbasi, N., Hamlet, S., Love, R. M., & Nguyen, N. T. (2020). Porous scaffolds for bone regeneration. Journal of Science: Advanced Materials and Devices, 5(1), 1-9.

[59] Eosoly, S., Brabazon, D., Lohfeld, S., & Looney, L. (2010). Selective laser sintering of hydroxyapatite/poly-ε-caprolactone scaffolds. Acta biomaterialia, 6(7), 2511-2517.

[60] Wiria, F. E., Leong, K. F., Chua, C. K., & Liu, Y. J. A. B. (2007). Poly-ε-caprolactone/hydroxyapatite for tissue engineering scaffold fabrication via selective laser sintering. Acta biomaterialia, 3(1), 1-12.

[61] Eosoly, S., Lohfeld, S., & Brabazon, D. (2009). Effect of hydroxyapatite on biodegradable scaffolds fabricated by SLS. In Key Engineering Materials (Vol. 396, pp. 659-662). Trans Tech Publications Ltd.

[62] Eosoly, S., Vrana, N. E., Lohfeld, S., Hindie, M., & Looney, L. (2012). Interaction of cell culture with composition effects on the mechanical properties of polycaprolactone-hydroxyapatite scaffolds fabricated via selective laser sintering (SLS). Materials Science and Engineering: C, 32(8), 2250-2257.

[63] Eshraghi, S., & Das, S. (2012). Micromechanical finite-element modeling and experimental characterization of the compressive mechanical properties of polycaprolactone–hydroxyapatite composite scaffolds prepared by selective laser sintering for bone tissue engineering. Acta biomaterialia, 8(8), 3138-3143.

[64] Misch, C. E., Qu, Z., & Bidez, M. W. (1999). Mechanical properties of trabecular bone in the human mandible: implications for dental implant treatment planning and surgical placement. Journal of oral and maxillofacial surgery, 57(6), 700-706.

[65] Bartnikowski, M., Dargaville, T. R., Ivanovski, S., & Hutmacher, D. W. (2019). Degradation mechanisms of polycaprolactone in the context of chemistry, geometry and environment. Progress in Polymer Science, 96, 1-20.

[66] Visscher, L. E., Dang, H. P., Knackstedt, M. A., Hutmacher, D. W., & Tran, P. A. (2018). 3D printed Polycaprolactone scaffolds with dual macro-microporosity for applications in local delivery of antibiotics. Materials Science and Engineering: C, 87, 78-89.

[67] Azevedo, M. C., Reis, R. L., Claase, M. B., Grijpma, D. W., & Feijen, J. (2003). Development and properties of polycaprolactone/hydroxyapatite composite biomaterials. Journal of materials science: Materials in medicine, 14(2), 103-107.

7. General Conclusions

This PhD thesis is the result of wide collaborations with Italian and international universities as well as industry working in the field of biomaterials and biodevices for tissue engineering. The approach adopted in this study was based on the production of biomaterials by using additive manufacturing technologies such as laser powder bed fusion, electron beam powder bed fusion and vat photopolymerization. After production biomaterials and biodevices in the form of 3D scaffolds were submitted to advanced structural, mechanical and biological characterization. Optimization of the production technology, the lattice geometry of 3D scaffolds and the mechanical and biological performances of products allowed obtaining devices suitable for the regeneration of the target tissues.
Although, outstanding results were obtained in this research work, attested by the papers published in international journals and listed below, many efforts will be necessary in the near future to solve the numerous problems still opened in the field of biomaterials and biodevices for tissue engineering applications.

This PhD thesis is a selection of works conducted during the 20th PhD cycle (2018-2022) at the SIMAU Department of the Università Politecnica delle Marche (Ancona, Italy). During the doctoral period, the study of biomaterials for tissue engineering produced by additive manufacturing was carried out by advanced characterization *in vitro*.

All research works were performed in collaboration with universities and companies, such as:

- Politecnico di Torino, Torino;
- Università degli studi di Pavia;
- Dept. DISCO and Dept. DISCLIMO of Università Politecnica delle Marche;
- 3D4Mec Srl, Sasso Marconi (BO), Italy;
- Prosilas Srl, Civitanova Marche (MC), Italy;
- PUNTOZERO, Milano (MI), Italy;
- Reykjavik University
- Transilvania University

The results obtained in this research work are reported in the following scientific papers:

1. Giuliani, A., Gatto, M. L., Gobbi, L., Mangano, F. G., & Mangano, C. (2020). Integrated 3D information for custom-made bone grafts: focus on biphasic calcium phosphate bone substitute biomaterials. International Journal of Environmental Research and Public Health, 17(14), 4931.
2. Tosco, V., Vitiello, F., Furlani, M., Gatto, M. L., Monterubbianesi, R., Giuliani, A., ... & Putignano, A. (2021). Microleakage analysis of different bulk-filling techniques for class II restorations: μ-CT, SEM and EDS evaluations. Materials, 14(1), 31.

3. Gatto, M. L., Groppo, R., Bloise, N., Fassina, L., Visai, L., Galati, M., ... & Mengucci, P. (2021). Topological, mechanical and biological properties of Ti6Al4V scaffolds for bone tissue regeneration fabricated with reused powders via electron beam melting. *Materials*, *14*(1), 224.
4. Putignano, A., Tosco, V., Monterubbianesi, R., Vitiello, F., Gatto, M. L., Furlani, M., ... & Orsini, G. (2021). Comparison of three different bulk-filling techniques for restoring class II cavities: μCT, SEM-EDS combined analyses for margins and internal fit assessments. Journal of the Mechanical Behavior of Biomedical Materials, 124, 104812.
5. Gatto, M. L., Furlani, M., Giuliani, A., Bloise, N., Fassina, L., Visai, L., & Mengucci, P. (2021). Biomechanical performances of PCL/HA micro-and macro-porous lattice scaffolds fabricated via laser powder bed fusion for bone tissue engineering. Materials Science and Engineering: C, 128, 112300.
6. Gatto, M. L., Groppo, R., Furlani, M., Giuliani, A., Mangano, C., & Mangano, F. (2022). Lithography-based Ceramic Manufacturing (LCM) versus Milled Zirconia Blocks under uniaxial compressive loading: An in vitro comparative study. Journal of Dentistry, 116, 103886.